POLITECNICO DI MILANO

Department of Chemistry, Materials and Chemical
Engineering "G. Natta"

Master of science in Materials Engineering and Nanotechnology

BiVO$_4$ – based photoanodes for
photoelectrochemical water splitting

Supervisor: **prof. Luca Magagnin**

Assistant supervisor: **Ruben Dell'Oro**

Master thesis author:

Stefano Ghidotti
Matr. 898814

Academic year 2019/2020

SUMMARY

SUMMARY OF FIGURES AND TABLES

IV

ABSTRACT

In the present work, synthesis via different metalorganic decomposition methods of bismuth vanadate based photoanodes was investigated for potential water splitting application in a photoelectrochemical cell, evaluating characteristics of the produced films also for a hypothetical large-scale production.

$BiVO_4$ has been thoroughly analyzed over the recent years among semiconducting materials suitable for these kinds of applications, primarily thanks to its optimal electronic band structure and cost effectiveness. Doping with metallic elements, such as molybdenum, has proven to be beneficial for photoelectrochemical performances of $BiVO_4$ films, improving aspects like conductivity and absorption behavior.

To produce the films, drop casting and spin coating techniques were exploited, with deposition of precursor solutions onto Fluorine doped Tin Oxide (FTO) substrates. A Sequential Ionic Layer Adsorption and Reaction (SILAR) method was utilized to produce very thin seed layers of $BiVO_4$ nanoparticles onto FTO, with drop casting of the $BiVO_4$ solution performed afterwards. A thin layer of undoped tin oxide was instead produced on top of the FTO surface before spin coating of $BiVO_4$ to positively influence band structure and morphology of the photoanodes. Characteristics of the photoactive film were modified by deposition of SnO_2 at varying thicknesses. The photoelectrochemical performances of produced photoanodes were evaluated via Linear Scan Voltammetry (LSV) tests carried out in a 1 M $NaSO_3$ solution containing a phosphates buffer at pH 7, with current outputs produced at 1.23 V vs RHE taken as benchmark values. SEM, AFM and XRD were utilized to identify key parameters of deposited films and consequently modify the fabrication strategy.

The main accomplishment was the fabrication of highly uniform deposits with appreciable current outputs. Samples fabricated via drop casting showed photocurrent density outputs of 2.3 mA/cm^2 and 3.3 mA/cm^2 for deposition onto FTO or onto a seed layer respectively, but lacked uniformity along the surface and reproducibility. Spin coating deposition allowed instead both homogeneity and reproducibility, with current density outputs measuring 1.28 mA/cm^2. Finally, exploitation of the modified band structure caused by the SnO_2 layer in between FTO and $BiVO_4$ gave values of 1.68 mA/cm^2, which was shifted to a 2.1 mA/cm^2 after optimization of the SnO_2 thickness.

ABSTRACT

Nel presente lavoro, la sintesi di fotoanodi basati su vanadato di bismuto per mezzo di diversi metodi di decomposizione metallorganica è stata investigata per una potenziale applicazione di water splitting in cella fotoelettrochimica, valutando le caratteristiche dei film prodotti anche per un'ipotetica produzione su larga scala.

Tra i materiali adatti a questo tipo di applicazioni, il $BiVO_4$ è stato analizzato a fondo durante gli anni recenti, principalmente grazie alla sua ottimale struttura elettronica a bande e efficacia dei costi. Il drogaggio con elementi metallici, come il molibdeno, si è dimostrato vantaggioso per le prestazioni fotoelettrochimiche di film in $BiVO_4$, migliorandone aspetti come conduttività e comportamento in assorbimento.

Per la produzione dei film sono state utilizzate tecniche di drop casting e spin coating, depositando le soluzioni dei precursori su substrati di ossido di FTO. Un metodo SILAR è stato utilizzato per produrre film "seed" molto sottili di nanoparticelle di $BiVO_4$ su FTO, con drop casting della soluzione di $BiVO_4$ effettuato successivamente. Un sottile layer di stagno ossido non drogato è stato invece prodotto sopra alla superficie di FTO prima di produrre $BiVO_4$ via spin coating, in modo da influenzare positivamente la struttura a bande e la morfologia dei fotoanodi. Le caratteristiche del film fotoattivo sono state modificate tramite la deposizione di SnO_2 a differenti spessori. Le performance fotoelettrochimiche dei fotoanodi prodotti sono state valutate via test LSV condotti in una soluzione 1 M di $NaSO_3$ a pH 7 contenente buffer di fosfati, con gli output di corrente prodotta a 1.23 V vs RHE presi come valori di benchmark. SEM, AFM e XRD sono state utilizzate per identificare parametri chiave dei film depositati e modificare la strategia di fabbricazione di conseguenza.

Il principale risultato ottenuto è stata la fabbricazione di film altamente uniformi con apprezzabili livelli di corrente prodotta. I campioni fabbricati per drop casting hanno mostrato densità di fotocorrenti di 2.3 mA/cm² e 3.3 mA/cm² con deposizione su FTO e sullo strato seed, rispettivamente, ma con troppo basse uniformità superficiale e riproducibilità. La deposizione per spin coating ha invece permesso di ottenere sia omogeneità che riproducibilità, con valori di densità di corrente di 1.28 mA/cm². Infine, la struttura a bande modificata dallo strato di SnO_2 tra FTO e $BiVO_4$ ha prodotto valori di 1.68 mA/cm², spostato a 2.1 mA/cm² ottimizzando lo spessore di SnO_2.

1 INTRODUCTION

1.1 Fossil fuel and greenhouse effect

Over the course of the last two centuries, the world's energy demand has been increasing by an average of 2.3% a year. This can be linked both to the growth of population and to the fact that the industrial revolution brought into play an enormous need for energy, necessary for economic progress all over the globe. Today the main sources being utilized to supply this demand are fossil fuels, originated in the Earth's crust from the rests of organic matter over the course of some hundreds of millions of years. Some of the most important fossil fuels examples, considering their large scale consume all over the world, are coal, petroleum, natural gases and bitumen, used principally for heat and electricity production. Besides their major constituents, which are hydrogen, carbon and oxygen, all these fossil fuels contain other elements which originate various types of pollutants (sulfur oxides and nitrogen oxides to cite some) upon combustion. These compounds have very detrimental effects when they're released in the atmosphere in large quantities, heavily affecting men and the environment in general, through air, water and soil contamination. *(1)*

The most dangerous effect caused by human activities can be identified in global warming, an effect which consists in an overall increase of the temperature all over the world, resulting in climate change and destruction of ecosystems; apart from the rising temperatures in recent years, some indicators of climate change are the increase in occurrence of extreme climate-related events or the shifting of snow and rainfall patterns. The temperature on Earth is a direct effect of the presence in the atmosphere of the so-called "greenhouse gases", which act as a natural barrier, screening the re-emission into space of part of the radiation coming to Earth from the Sun. This results in keeping the planet's temperature at a reasonable level, but human activities in the last centuries have caused an abrupt rising of the concentration of greenhouse gases (mainly carbon dioxide) in our atmosphere, which are produced mainly by the above-mentioned combustion of fossil fuels. *(2) (3)*

While humans keep relying on this kind of energy sources, the greenhouse effect's influence is severely felt by ecosystems and more in general by the atmosphere, but this is not the only reason why this energetic production model isn't sustainable; in fact, fossil fuels take hundreds of millions of years to be generated, and considering today's fast consumption rates it can be estimated that the current reservoir will last approximately another 50 to 60 years. *(2) (4)*
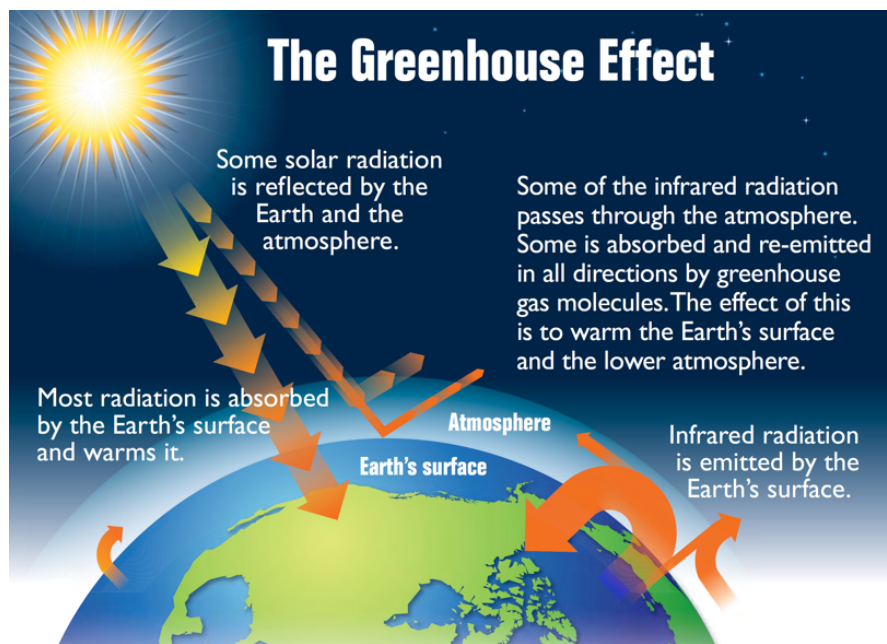
Figure 1. Representation of the greenhouse effect. **(3)**

It is primarily for these reasons that governments of the most important industrialized countries of the world have adopted measures in order to limit this dangerous trend, the most important of them being represented by the Kyoto Protocol agreement, in which it is stated that the ultimate objective, starting from the year 2005 and on, is a "stabilization of greenhouse gas concentrations in the atmosphere at a level that would stop dangerous anthropogenic interference with the climate system". Keeping in mind the always rising energy demand of society, more sustainable production methods, together with better waste management and promotion of eco-friendly lifestyles, have been rising in popularity over the last decades, making the class of renewable sources more important than ever. Among these some important examples are sunlight, wind and water energy. *(2) (5)*
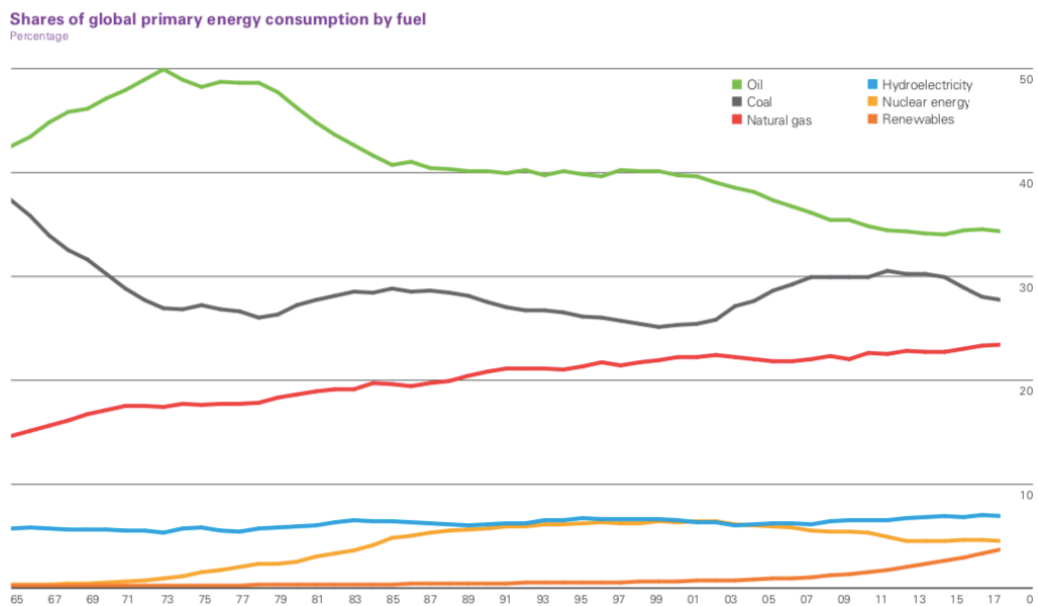
Figure 2. Global energy consumption by tipe of fuel up until 2017; oil, coal and natural gases are still used to produce roughly 86% of the total energy consumed over the world, but oil and coal contributes declined over the course of the last years, while renewable power reached a record high 3.6% in 2017. **(6)**

Hydrogen is expected to play a key role in order to replace fossil fuels in the world's near future, since its conversion to power is clean and simple, but although being the most common chemical element on Earth, it does not exist in nature in its elemental form, so it's only possible to obtain it via separation from stable compounds, the most abundant of which is surely water. As of today, most of the molecular H_2 is still produced via non-renewable sources such as oil, natural gas and coal, while "greener" solutions still need improvements in order to be applied for large scale production. *(5) (7)*

Among these, photoelectrochemical water splitting has received considerable attention over the past years, as a potential technique able to generate hydrogen with zero environmental impact. If improved at a level allowing production of considerable amounts of energy, it could cover a fundamental role in sustainability for future generations.

Global mean temperature

Period Years	Rate °C / decade
25	0.177±0.052
50	0.128±0.026
100	0.074±0.018
150	0.045±0.012

- • Annual mean
- ▬ Smoothed series
- ▬ 5-95% decadal error bars
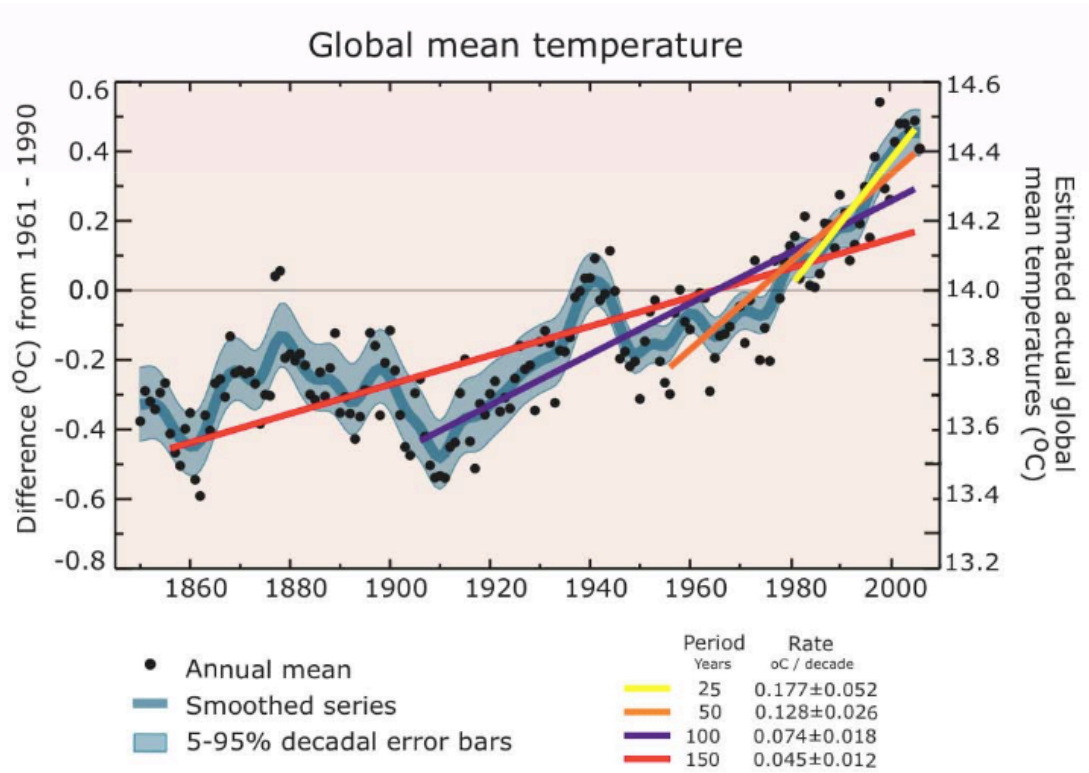
Figure 3. Global mean temperature observed through the years, with linear trends observed over periods of time represented by the colored lines. The Yellow line indicates the highest rate of increasing °C/decade in the last 25 years over prior decades. **(2)**

2 STATE OF THE ART

2.1 Electromagnetic spectrum

The nature of light has been extensively studied by scientists already for thousands of years, with some considerations made from Aristotle dating back to year 500 B.C., in which the philosopher-scientist identified light with the product of vibrations of a substance called "aether", which fills all space but is not visible for the human eye. Later on, in the 17th century, Newton improved Aristotle's definition by adding that light consists of tiny, fast moving particles causing vibrations of the "aether". Then other scientific contributions highlighted the wavy nature of light above the particle-like one, giving rise to two parallel lines of thought, waves and particle theory. *(8)*

These two schools of thought were addressed between the second half of the 19th century and the first half of the 20th, thanks to the work of scientists like Maxwell, Planck and Einstein, who presented theories and conducted experiments demonstrating that the nature of light cannot be described with a single classical model, because of its dual wave-particle nature, being that it is both a wave and a stream of zero-mass particles, called photons. Using quantum mechanics, under the assumption of light's dual nature, it was finally possible to gain a complete understanding of radiative phenomena. Moreover, in the year 1900, Max Planck discovered, thanks to his experiments on black-body radiation, that any measurable amount of energy isn't continuous, but rather a discrete value, multiple of a fundamental quantity called quantum, whose energetic value is associated to that of a photon:

$$E = h\,\nu\,[J]$$

in which E is the energy of the particle, ν is the frequency of the radiation and h is Planck's constant, equal to $6.626*10^{-34}$ J s. *(8)*

This means that the frequency of the light wave travelling in space determines the energy of the photons of the wave itself, and each of them contributes to the total

amount transported by the wave with a single quantum. A reasonable way to classify electromagnetic waves is then a complete spectrum divided in regions associated to a specific interval of frequencies (or wavelengths), and that is the electromagnetic spectrum, organizing waves ranging from below 1 Hz to above 10^{25} Hz (figure 4). Going from low to high frequencies, there are radio waves, microwaves, infrared, visible, ultraviolet, x-rays and γ-rays. The part of the light spectrum that is visible for the human eye occupies the region ranging from 750 to 380 nm of wavelength. This classification means that all these categories are essentially the same phenomenon from a qualitative point of view, but they're different when the energy of the photons of light is taken into account. *(8)*
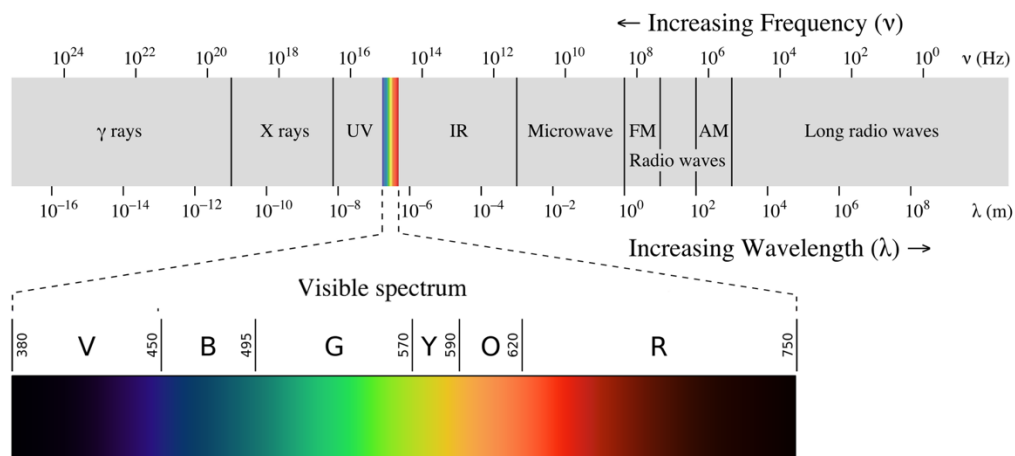
Figure 4. Light electromagnetic spectrum. (Wikipedia Commons)

2.1.1 The solar spectrum

A black body is able to absorb radiation and, as a result of its heating, to dissipate its thermal energy through emission of photons. The wavelength of electromagnetic waves thus emitted is not fixed, so there's no monochromatic emission, but instead the distribution of energy can vary, depending on the temperature of the body itself. The Sun's spectrum can be modeled by considering it a black body at a temperature around 5760 K, so its emitted photons can have different wavelengths. For this case in

particular, the emission spectrum covers wavelengths from roughly 250 nm to 2500 nm, so from the UV to the IR range, covering the entirety of the visible range. *(9)* Emissivity of a body can be defined as its efficiency in emitting energy in the form of thermal radiation. Considering that emission isn't uniform over the whole spectrum, it is possible to calculate for which value of the wavelength there is maximum emissivity (so more photons emitted over any other λ) just by knowing the value of the emitting body's temperature, through Wien's law:

$$T * \lambda_{max} = b$$

where T is the body's temperature, λ_{max} is the wavelength corresponding to maximum emissivity and b is the Wien's constant, equal to $2.8978*10^{-3}$ m K. As evident from figure 5, when considering the Sun this translates to an emission peak in the visible region, from roughly 300 to 800 nm. *(9)*
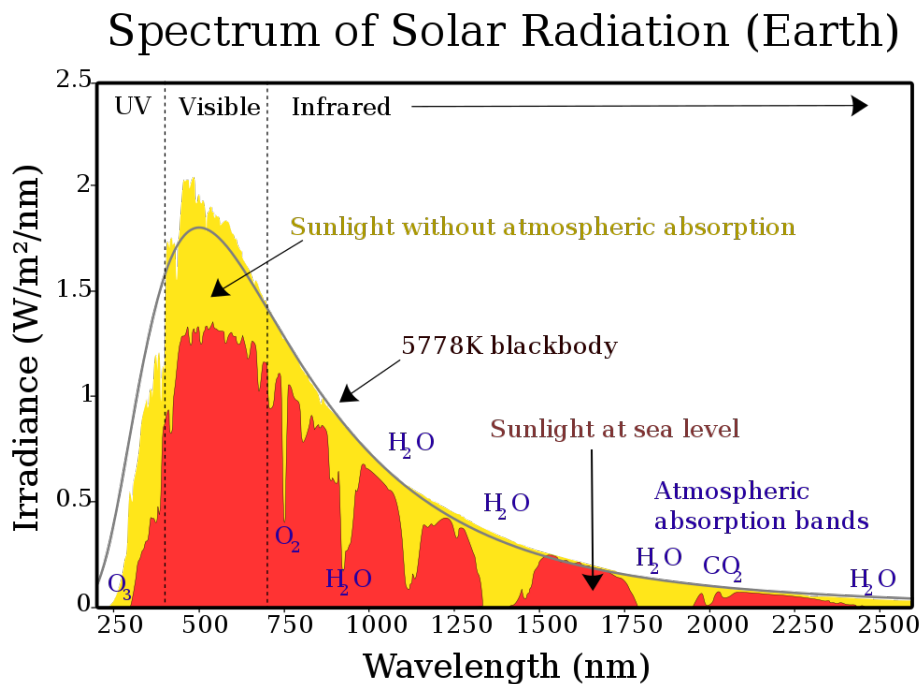
Figure 5. Solar radiation spectrum above Earth's atmospheric level (yellow area), at sea level (red area), with respect to the theoretical spectrum model over a black body at 5778 K (black line); the chemical compounds responsible for photons absorption are indicated. (Wikipedia Commons)

Important considerations must be made regarding the power emitted by the Sun. Upon irradiation at the surface of the star, power density measures 62 MW/m², but this value is reduced by the considerably large factor of 4.6*10⁴ before reaching Earth's surface, where the density is indeed 1353 W/m². This reduction is caused mainly by two factors, one of geometrical nature and the other of chemical one. The former causes a decrease of the power density because of its direction of propagation from the center where it starts its path directed to the Earth; due to the radial emission, at the Sun's surface a certain amount of power is distributed over a given area, whose value increases with the distance from the Sun, so the superficial density of power is reduced. The geometrical attenuation factor can be expressed as:

$$g.a.f. = \left(\frac{R_S}{d_E}\right)^2 \approx 2.16 * 10^{-5}$$

where R_S is the Sun's radius and d_E is the distance to reach Earth's surface.

The second cause of the power density's reduction is the passage of radiation through Earth's atmosphere, where photons inevitably interact with various types of molecules, among which oxygen, ozone, water vapor and carbon dioxide are the most significant, but also methane and fluorinated hydrocarbons play an important role. This interaction results in radiative absorption from these chemicals in the air, so ultimately the electromagnetic spectrum reaching Earth's surface is significantly different from the one originated by the Sun. In figure 5, the yellow area is the latter, while the red area is the former; photons in the UV region, on the left part of the spectrum, are absorbed by ozone and oxygen molecules, while for the IR range CO_2 and water vapor are the main responsible. Photons in the visible part of the spectrum, which registers the largest difference between the two areas, are lost due to reflection and scattering caused by the atmosphere and clouds. It's worth pointing out how for some regions in the IR range the irradiance (the name of emissivity expressed in function of energy instead of wavelength) on Earth's surface is zero. *(9) (10)*

The attenuation of radiation can be quantified by considering the Air Mass factor, expressed as:

$$AM = \frac{L}{L_0} \approx \frac{1}{\sin \vartheta}$$

in which L_0 is the is the length from the considered point on Earth's surface to its zenith (so normal to Earth), L is the actual path of the radiation, and ϑ is the incident angle with respect to L direction. The Air Mass factor's expression above is the mathematical explanation for the fact that if the radiation has to cover a longer path through the atmosphere, attenuation is higher, due of course to a larger number of photon interactions; the value stays zero up to the point where photons encounter the atmosphere, while it's generally around 1.5 at the level of Earth's crust if the angle is considered around 48.2°. Considering the AM1.5 spectrum is important when working with solar devices. *(10)*

2.2 Electronic properties of materials

A solid material is formed by densely packed atoms interacting with each other. This interaction results in a modification of the electron's properties with respect to the case of an isolated atom. In other words, the properties of an electron in condensed matter are very different than in the case of single atoms. The allowed energy levels in single atoms are distributed in a discrete way, with every state well separated by its neighbors by a defined energy gap. Once atoms start forming bonds, independently from the type of solid, these energetic states start to influence each other, completely changing the electronic configuration of the material; because of this fact electrons cannot be described anymore as they were in the case of isolated atoms, and it is necessary to introduce the electronic band structure theory. This description is able to determine the energy levels that an electron can occupy within a solid material, dividing them in different bands, each one having a finite width and a separation from the neighbor bands, identified as energy gap, an interval which is forbidden for electrons. This structure results from the overlapping of the single atomic orbitals upon formation of a high number of interatomic bonds; energy levels within a single band are quasi-continuous, and, since electrons follow Pauli's exclusion principle, there's no possibility of an electronic flux when a band is completely full. *(11) (12)*

In this type of description, it is of crucial important to identify two particular bands. The valence band (VB), is the band of maximum energy comprehending all of the occupied electronic orbitals. Its maximum energetic level is called valence band edge, labelled as E_{VB}. Correspondingly, the immediately upper band (i.e. the lowest one including all of the unoccupied electronic states of the solid), called conduction band (CB), has its lowest possible energy level, the conduction band edge, labelled as E_{CB}. In materials where it is present, the gap between the VB and the CB is called band gap (BG), and has its associated energy value corresponding to $E_{BG} = E_{CB} - E_{VB}$. Thermal, electric and other kind of energetic sources can cause the promotion of electrons from the VB to the CB, provided that the amount of given energy is equal or greater than the value of E_{BG}; if that's the case, the excited electron can jump from its level in the VB to an excited one in the CB, leaving a hole at the starting point. *(9) (12)*

Materials can be classified from the electronic distribution point of view by dividing them into three different categories, based on the different band structures and resulting electrical properties. These categories are insulators, conductors and semiconductors. Before describing them, it is important to define two fundamental energy levels:

- χ: called vacuum energy level, it corresponds to the potential energy of an isolated electron in vacuum at rest;
- E_F: Fermi energy level, defined as the most energetic one for which, at T = 0 K, the occupation probability is 1, and above which probability goes to 0. At T > 0 K, it is instead defined as the level for which occupation probability is equal to 0.5. *(12)*

As depicted in figure 6, insulators are materials characterized by a relatively high E_{BG}, which is greater than 3 eV. This implies a close to zero conductivity at any T level, since even considerable amounts of thermal energy aren't enough to excite electrons from the VB to the CB, which remains completely empty. Materials belonging to this class are predominantly white, since they can only absorb photons with E > 3 eV, resulting in all the visible radiation being diffused, rather than absorbed. Of course, this class of materials cannot be interesting for applications exploiting solar radiation, since their absorption in the corresponding range isn't able to produce appreciable voltages. *(12)*
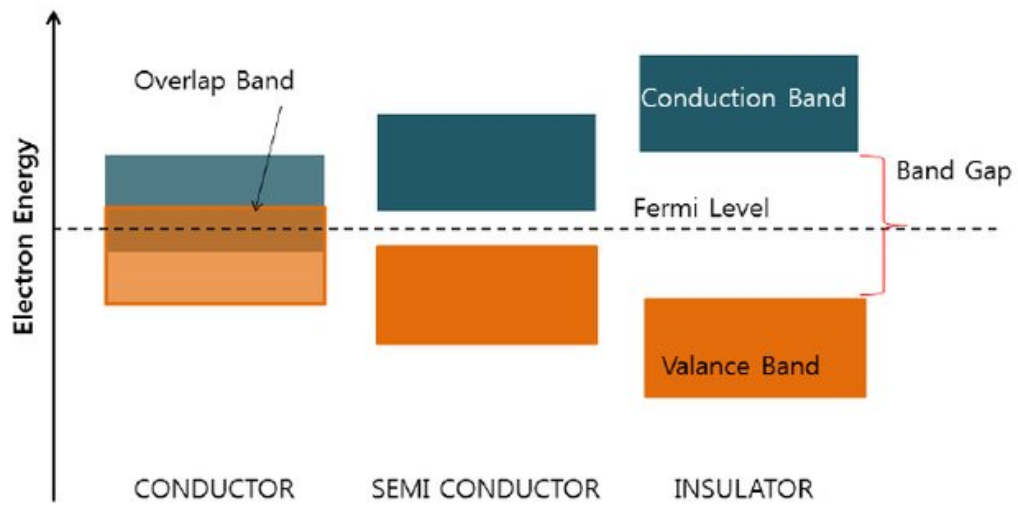
Figure 6. Band gap diagram for conductor, semiconductor and insulator materials. **(13)**

Electronic conductor materials, such as metals, are instead solids not presenting an E_{BG}, or even with an overlapping of the VB and the CB. This fact grants high values of electrical conductivity to these materials, with electrical charges able to move very easily under the influence of a potential difference created by an external electric field, thus originating a current. Because of the high availability of energy states easily reachable, these materials have the ability to absorb incoming photons over a very wide range of frequencies. As a consequence to the great ease of movement for the charge carriers in conductors, the voltage obtained from the potential difference between the energy levels of photogenerated electrons and holes can't be defined, since their recombination, with consequent emission of phonons, is practically instantaneous. *(14) (15)*

Finally, semiconductors are materials in which the value of the E_{BG} is greater than zero, but still considerably lower than in the case of insulators, with values generally comprised between 0.4 and 3 eV. This puts their electronic properties in between those of conductors and insulators; they can in fact behave as quite good conductors in particular conditions, such as in presence of T higher than normal or with significant doping levels. Therefore, unlike insulators, they're able to produce a current upon appropriate stimulation of charges from the VB to the CB. When considering solar radiation in particular, the maximum emissivity is registered in the range around 2 to

3 eV, which is a high enough value to excite electrons to the CB, creating an electron-hole exciton. Thanks to this ability to generate excitons in a relatively easy way, and to the presence of $E_{BG} > 0$ (which hinders recombination, unlike conductors), semiconductors illuminated in proper conditions are the preferred choice for photovoltaic applications, generating significant open circuit voltage and short circuit current values. *(11) (12) (16)*

2.2.1 Semiconductors

In semiconductors, electrical conductivity is the result of the formation of excitons, i.e. the separation of electrons and holes caused by an external energy input. Holes are quasi-particles identified with the absence of electrons, and behave as a positive particle would, with the peculiarity of considering an effective mass determined by the electronic band structure. The equation describing electrical conductivity for a semiconductor highlights this double contribution, relating it with the presence of electrons and holes in the CB and VB respectively:

$$\sigma = n_e q_e \mu_e + n_h q_h \mu_h$$

in which n is the number of carriers, q the unitary charge and μ the mobility. To understand the following considerations, it is important to keep in mind that the charge carriers increase conductivity only when located in the suitable band to do so. *(16)*
So, the value of the electrical conductivity σ depends not only on the number of carriers, but on their mobility as well. In order to enhance σ in a semiconductor, two ways are applicable:
- Increasing the temperature of the material, which produces thermal excitation for the electrons in the conduction band. In this case the material is still an intrinsic (pure) semiconductor, with its Fermi level located in the middle of the band gap; *(16)*
- Doping, with the insertion of small amounts (quantities around 10^{16}-10^{17} cm^{-3}) of particular impurities into the base material. This gives an extrinsic

semiconductor, with the dopant promoting formation of some discrete energy levels lying within the forbidden region, and whose position is determined by the type of impurity introduced in the lattice. In the case of a p-doped semiconductor, the dopant's atoms have one electron less than the atoms of the base material in their VB, so a vacancy is introduced in the lattice, with consequent formation of an energy level just above the VB (in the forbidden region). These newly formed energy levels are so close to the top of the VB that the energetic difference between the two points is in the order of kT, and such a small quantity is easily achievable through thermal excitation; heat is enough to excite an electron in the VB to the new levels above it, leaving a hole behind. In this type of materials, electrical conductivity is then enhanced thanks to the higher number of holes obtained in the VB through this mechanism.

For n-doped semiconductors, the impurities introduced have atoms with one electron more than the base material, so extra electrons are brought into the lattice. Also in this case there's formation of new energy levels, but what differs is their location within the forbidden region; the levels formed with n-doping lie in fact just below the CB, at a distance of the same order of that between the VB and the levels formed with p-doping. Therefore, also in this case it is possible to excite the electrons into the CB just with the use of thermal energy. *(16)*
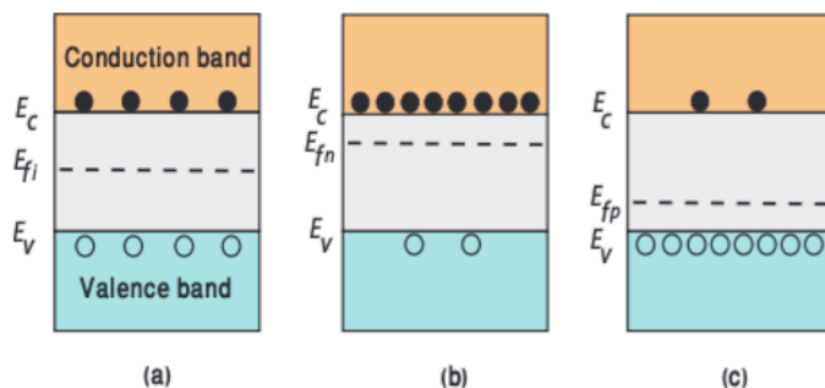
Figure 7. Energy band diagrams for an intrinsic semiconductor (a), an n-doped one (b) and a p-doped one (c), with corresponding Fermi levels and charge carriers highlighting the beneficial effect of doping on conductivity. **(16)**

So both p and n-doping can enhance electrical conductivity via the insertion of charge carriers within the right band. As explained from figure 7, in extrinsic semiconductors the E_F level is shifted from the middle of the forbidden region closer to the VB and closer to the CB in p-doped and n-doped materials respectively. *(17)*

The value of conductivity can also be increased under illumination. If a monochromatic radiation with photon energy higher than the gap of the material is directed onto it, photons can be absorbed, causing formation of excitons with related promotion of electrons into the CB and creation of holes into the VB. The increase of conductivity in the material can be quantified by the equation:

$$\Delta\sigma_{ill} = qG(\tau_e\mu_e + \tau_h\mu_h)$$

where G is the coefficient of electron-hole pair generation per unit volume and τ the recombination time of the specific carrier, that is the time after which it recombines with the carrier of opposite charge. *(16)*

When illumination generates excitons in the semiconductor, the level of E_F is modified. As reported in section 2.2, the Fermi level at $T > 0$ K is defined as the energy level for which the probability of occupation for carriers (electrons or holes) is equal to 0.5, but since illumination drastically changes the distribution of both electrons and holes, shifting the former closer to the CB edge and the latter to the VB edge, also the Fermi energy of the system must be re-evaluated. The E_F of the semiconductor is split into two new quasi-Fermi levels, one for the distribution of the electrons (E_{Fn}) and one for that of holes (E_{Fp}), which are shifted from the original one accordingly to their corresponding charge carriers, as shown in figure 8. *(16) (18)*

The splitting of the Fermi level is of fundamental importance for photovoltaic applications, because it gives an appreciable ΔE_F, defined as the chemical potential of the material, which is in turn directly proportional to the maximum voltage at which the electrons can be extracted in a photovoltaic cell. *(9)*
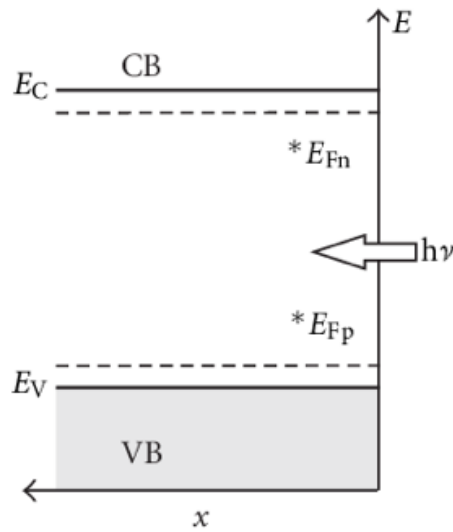
Figure 8. Splitting of the Fermi level into two quasi-Fermi levels in a semiconductor under illumination conditions. **(18)**

2.3 Hydrogen

As already mentioned in section 1.1, Hydrogen is a promising resource for green energy production in the near future. This is due to its great reactivity and power density, being able to release an extremely high amount of energy upon reaction with the oxygen present in air, with just water as a byproduct. Considering these characteristics, it comes as no surprise that interest for hydrogen (primarily as a fuel for zero emission vehicles), has been rising over the last decades. *(5)*

2.3.1 Fuel cell

The device able to convert hydrogen's chemical energy into electrical is called fuel cell, which represents one of the cleanest and most efficient electricity generating technologies. While operating, a fuel cell does not produce any type of pollutants throughout its whole functioning, directly consuming hydrogen and giving only electricity, with water and heat as secondary products. As shown in figure 9, the

general structure of a fuel cell consists of an electrolyte layer separating a cathode and an anode. *(19)*
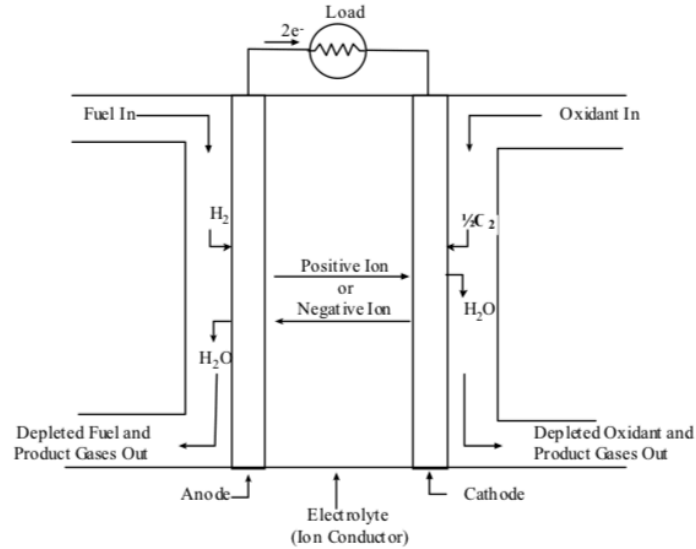
Figure 9. General schematic of a fuel cell. **(19)**

In a typical fuel cell, fuel, consisting mainly of pure hydrogen, is continuously fed to the anode (the negative electrode, at which oxidation takes place), while at the same time an oxidant, in the form of air or pure oxygen, goes to the cathode (the positive electrode, at which reduction takes place). The reactants undergo redox reactions at the interface between the electrodes and the electrolyte, producing both ions and electrons; the ions flow inside the electrolyte, while the electrons pass through an external circuit, powering a load. Catalysts are usually employed in order to speed up the reactions and obtain higher current outputs, while still maintaining a low system temperature. In order to keep the chemical reaction continuously running, it is important for the electrolyte to only allow passage of the appropriate ions, because free electrons or other substances inside of it would disrupt the process. *(19) (20)*

The maximum load that the fuel cell is able to sustain is equal to the potential difference between the reduction values of the two reactants participating in redox reactions (normally hydrogen and oxygen). Once hydrogen reaches the anode, it releases two electrons per H_2 molecule into the external circuit. These electrons spend electrical energy in the load and reach the cathode. In the meantime, H^+ ions travel

through the electrolyte to the cathode, where they react with oxygen, reducing it to give H_2O molecules, which are extracted from the system. By adjusting the supply of fuel and oxidant at the two electrodes, it's possible to regulate the current density produced by the cell, stopping the electrical production as soon as the gas flow supply is interrupted. *(19) (20)*

The electrical work a single cell can perform on an external load is expressed by:

$$W = -nFE$$

with n being the number of electrons involved in redox reactions, F the Faraday constant (equal to 96485.332 C/mol) and E the ideal potential of the fuel cell, which in turn can be calculated via the Nernst equation as:

$$E = E^0 + \frac{RT}{nF} \ln \left[\frac{\prod a_{i_{ox}}^{v_{ox}}}{\prod a_{i_{red}}^{v_{red}}} \right]$$

where R is the universal gas constant, T the temperature in K, E^0 the reversible potential of the cell, n again the number of electrons involved in redox reactions and F the Faraday's constant. *(19)*

	PEFC	**AFC**	**PAFC**	**MCFC**	**SOFC**
Electrolyte	Hydrated Polymeric Ion Exchange Membranes	Mobilized or Immobilized Potassium Hydroxide in asbestos matrix	Immobilized Liquid Phosphoric Acid in SiC	Immobilized Liquid Molten Carbonate in $LiAlO_2$	Perovskites (Ceramics)
Electrodes	Carbon	Transition metals	Carbon	Nickel and Nickel Oxide	Perovskite and perovskite / metal cermet
Catalyst	Platinum	Platinum	Platinum	Electrode material	Electrode material
Interconnect	Carbon or metal	Metal	Graphite	Stainless steel or Nickel	Nickel, ceramic, or steel
Operating Temperature	$40 - 80\ °C$	$65°C - 220\ °C$	$205\ °C$	$650\ °C$	$600\text{-}1000\ °C$
Charge Carrier	H^+	OH^-	H^+	$CO3^=$	$O^=$

Figure 10. Different examples of fuel cell type, with corresponding electrolyte, catalyst, T range of operations of interconnections, and ionic species passing through the electrolyte. **(19)**

Fuel cells are primarily classified by the type of electrolyte they use, which can be an acid, a base, a salt or a solid ceramic or polymerics membrane able to conduct ions. This classification is useful because it's the electrolyte that determines the reactions taking place at the two electrodes, so ultimately the ions travelling through it, closing the circuit. Moreover, the catalysts required, the T range in which the cell operates, the fuel required, and other factors are also determined by the electrolyte. All these characteristics, in turn, indicate for which applications the particular type of fuel cell is most suitable. Figure 10 shows some of the peculiar properties of the most diffused cell types. *(19)*

Apart from the two electrodes and the electrolyte shown in the previous scheme (figure 9), a fuel cell is composed of many other components, with the active region of the apparatus sandwiched between two catalyst layers. Conventional catalysts include nanometer-sized particles of platinum dispersed on a high surface carbon support, mixed with ion-conducting polymers. On the anodic side, the Pt nanoparticles enable the splitting of hydrogen molecules into protons and electrons, while on the cathodic one oxygen reduction takes place, via reaction with the protons generated at the anode, producing water molecules.
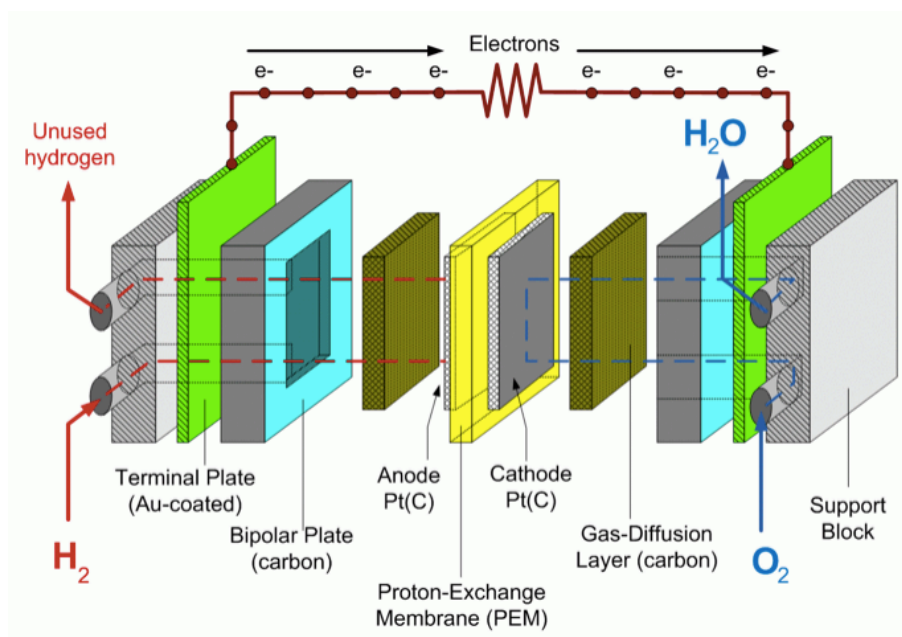
Figure 11. Components of a fuel cell. (PSU Department of Energy)

The active region is included inside a gas diffusion layer, typically composed of a sheet of porous carbon paper coated with a hydrophobic polymeric membrane; this porous layer allows both diffusion of reactants (in gaseous form) towards the electrodes and removal of H_2O from the active region. The whole structure just described, shown in figure 11, is in turn sandwiched between two bipolar carbon plates, and finally sealed with two conductive terminal plates (usually coated with gold), allowing flow of the electrons. *(20) (19)*

Although characterized by high efficiency (generally between 40 and 60%), fuel cells are individually able to produce only small values of potential (around 0,7 V), and for this reason the most common configuration utilized is that of a planar-bipolar fuel cell stack, in which the individual cells are put in series through electrical interconnections. This series configuration allows to obtain a voltage which is given by the sum of all the single ones produced by each cell, and this is usually sufficient to meet the application's requirements. Separator plates are employed in order to guarantee electrical connection between adjacent cells, while providing the whole stack with physical strength and forming a barrier able to isolate the gas flux of the single cells. The outer plates of the stack have a built-in serpentine structure aimed at refrigerating the internal cells, thus ensuring the characteristic low T of fuel cells processes. *(20)*

This category of systems is becoming more and more important with time, primarily thanks to their wide range of possible applications, including among the others on-site electrical powering of households and commercial buildings and auxiliary power generation for cars, trucks and aircrafts. One of the cutting-edge applications for fuel cells is their implementation as additional source of power in electric and hybrid vehicles. Electrical vehicles are those in which traction effort is supported only by electrical motors, while in a hybrid one the propulsion is obtained thanks to two or more kinds of energy sources. In particular, analyzing Fuel Cell Hybrid Electric Vehicles (FCHEV), an integrated and rechargeable fuel cell stack allows the vehicle to move. The first example of such a system adopted in the automotive industry, and still today one of the most popular, is the PEM (Polymeric Electrolyte Membrane) fuel cell, in which H_2 and O_2 are exploited as fuel and oxidant respectively. The polymeric membrane allows transport of ionic species from the anode to the cathode, while precluding electrons from following the same path, preventing short circuits. The most

used type is NAFION, a fluoro-copolymer functioning as protonic transporter, so that only H^+ ions can pass to the cathode where they react with oxygen to give water. The two electrodes are of course connected via an external circuit through which the flow of electrons charges the energy storage system; this load then stores and delivers power to the electrical power control unit, depending on its state of charge and on driving conditions. To ensure efficiency, flow regulators for both H_2 and O_2 have been implemented, allowing to control the consumption rates according to the required power, as described above for a general fuel cell. The stack and the flow regulators are inserted into the same module, which is connected to a DC/DC converter to charge the Li-ion battery of the vehicle. Finally, the oxygen required for the ionic reaction is directly taken from the outdoor environment as the vehicle moves, while the hydrogen, which is of course not present in air, is contained in an internal tank. *(21)*
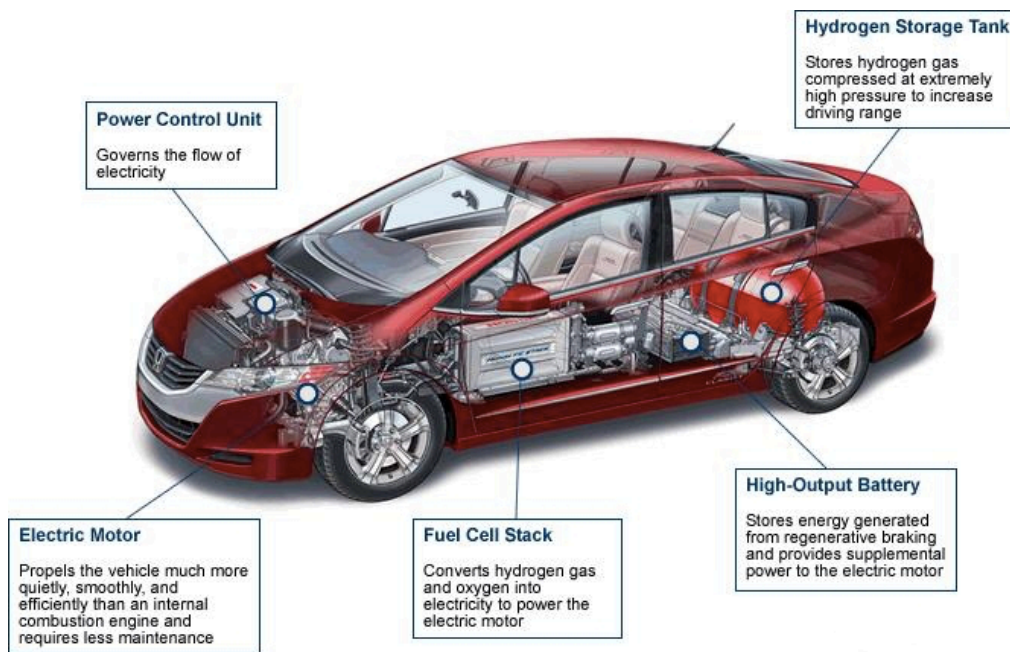
Figure 12. Schematic of a car with the implementation of a fuel cell stack. (American Honda Motor Co., Inc.)

The electrical energy stored is used to move the vehicle through an electrical drive and a coupling device which transfers power from the electrical motor to the wheels, but the striking difference between hybrid vehicles and internal combustion powered ones is the bi-directionality of the energy flow; as explained in figure 12, the electric battery

is able to store energy by converting the kinetic one generated from the braking or slowing down of the vehicle, which is usually wasted in traditional cars. *(22)*

2.3.2 Hydrogen production

There exist a variety of different ways in order to produce molecular hydrogen with zero environmental impact. The main sources present in nature that are used for this purpose are fresh and sea water, biomass and fossil fuels. These must be processed in order to extract H_2 molecules, and among the techniques used, some can produce pollutants in the form of byproducts, or have high cost over efficiency ratios. *(23)*

It is important to explain all of the different possible hydrogen production methods, comparing their advantages and disadvantages, in order to understand why photoelectrochemical water splitting, as a solar based process, is to be considered a very promising technique to ensure a future based on a cost-effective and green production of hydrogen.

2.3.2.1 Biomass gasification processes

The term biomass indicates renewable sources of energy derived from plants and animal material, among which it is possible to find crop and forest residues, animal and municipal waste, grass, and many other materials. In order to extract hydrogen as the final product, these sources must undergo a process called gasification, which can be of thermochemical or biological type, the latter being an example of a completely green technique. Nevertheless, as of today thermochemical gasification is the preferred method for H_2 production from biomasses, given its higher rate of production with respect to biological processes. The main thermochemical process exploited is pyrolysis, which consists in the application of heat to the biomass, reaching high temperatures between 650 and 800 °C in atmospheres containing controlled amounts of oxygen and steam, without triggering combustion of the materials involved. This implies the generation of liquid oils, solid charcoal and gaseous compounds. The main reaction involving the carbon-made biomasses, gives carbon monoxide as a byproduct,

but CO can be converted into CO_2 and molecular hydrogen via sequential reaction with the water steam in the chamber, improving the total yield of the process. The reactions just mentioned are:

$$C_nH_m + nH_2O \rightarrow nCO + \left(n + \frac{1}{2}m\right)H_2$$

$$CO + H_2O \rightarrow CO_2 + H_2$$
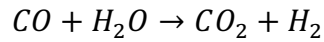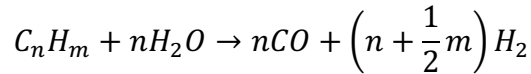
It's noticeable how both reactions produce hydrogen, and after the whole process carbon dioxide is the only byproduct. The "greener" alternative of biological processes employs bio-photolysis techniques, which are a group of methods very different from one another, exploiting particular abilities of bacteria or algae in order to produce H_2 in a completely biological way. *(24) (25)*

2.3.2.2 Plasma arc decomposition

Plasma is the state of matter identified with an ionized gas containing electrons in an excited state (extracted from their atoms of origin) and ionic species, with an overall electrical neutrality. Thanks to the significant presence of electrically charged species, plasma is suitable for an enormous range of applications in which it is exploited as a medium for high voltage electrical current release. Among these, there's the possibility to produce H_2 via decomposition of chemical species driven by plasma aided electrical discharges. The big advantage of plasma arc decomposition is its ability to produce 100% pure molecular hydrogen with zero emission of CO_2 or other pollutants (byproducts are only present in the form of carbon black solid particles). As an example, the decomposition reaction of methane, which is one of the most exploited sources for this particular technique, is reported below:

$$CH_4 \rightarrow C_{(s)} + 2H_{2(g)}$$
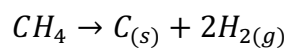
The main drawback of this method is the fact that it is relatively sophisticated, with the importance of managing the high temperatures involved in the decomposition reactions and the high costs related to the creation of plasma. *(25)*

2.3.2.3 Water splitting: electrolysis

Water splitting, as the name indicates, is the scission of water into its elemental components, hydrogen and oxygen. Among the techniques employed to perform this at industrial scale, electrolysis is the most widely spread and the most effective, thanks to its simplicity combined with the fact that it's able to produce hydrogen with a considerable level of purity. It is an electrochemical endothermic process, in which the water splitting is obtained thanks to the application of electrical power between two electrodes placed directly inside water; hydrogen is developed at the cathodic site, where electrons enter the water, while at the same time oxygen is produced at the anodic site. *(24)*

Being an electrochemical process, for the electrolysis to take place it is necessary that the voltage difference between anode and cathode is at least equal to the difference between the reduction potentials of hydrogen and oxygen. The reactions taking place in the cell are:

$$anodic\ equation\ (oxidation):\ \ 2H_2O_{(l)} \rightarrow O_{2(g)} + 4H^+_{(aq)} + 4e^-$$

$$cathodic\ equation\ (reduction):\ \ 2H_2O_{(l)} + 2e^- \rightarrow H_{2(g)} + 2OH^-_{(aq)}$$
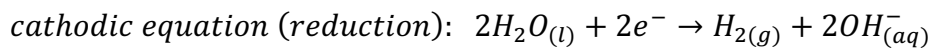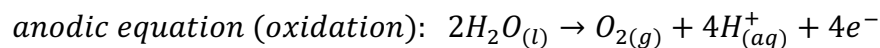
The Pourbaix diagram in figure 13 allows to identify the reduction potentials of hydrogen and oxygen as a function of the electrolyte's pH. The two values of interest can be then expressed as:

$$oxygen\ reduction\ potential:\ \ E = E^0_{O_2/H_2O} - 0.06pH = 1.23 - 0.06pH$$

$$hydrogen\ reduction\ potential:\ \ E = E^0_{H^+/H_2} - 0.06pH = 0 - 0.06pH$$
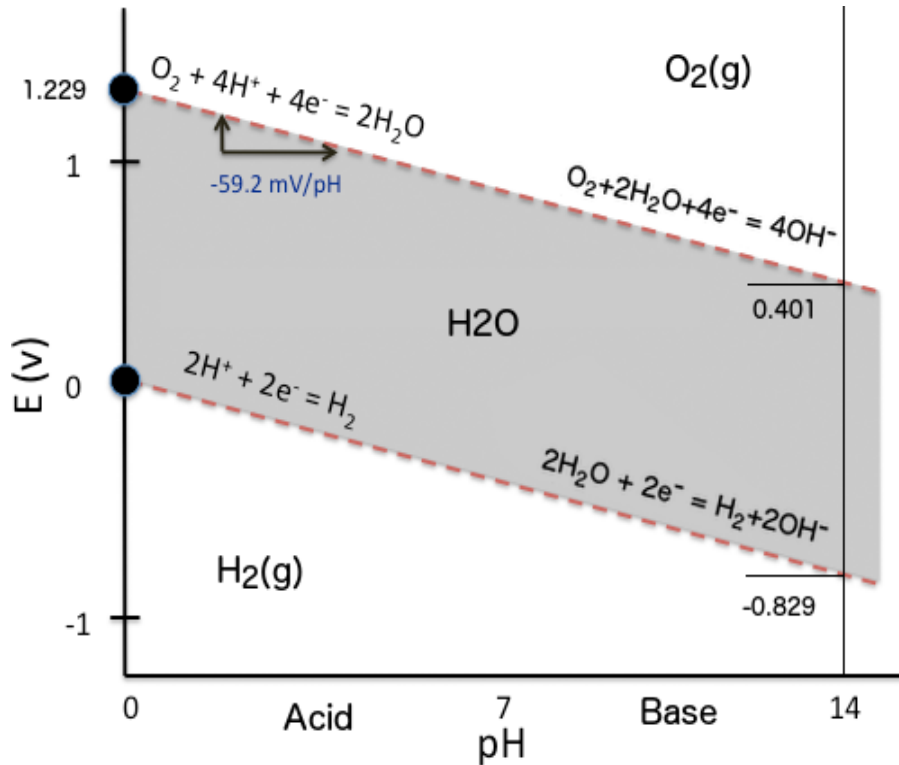
Figure 13. Water reduction and oxidation potentials (vs SHE) at varying pH. (Wikipedia Commons)

meaning that, in order to obtain water electrolysis, the applied potential difference must be at least equal to 1.23 V. In a real process, the role of overpotentials must be taken into account as well. *(25)*

2.3.2.4 Water splitting: thermolysis

Thermolysis, or thermochemical water splitting, is a water splitting method consisting in the heating of water to high temperatures, causing decomposition by breaking of the chemical bonds between hydrogen and oxygen atoms. Although conceptually simple, the process cannot reach reasonable yields until the temperature reaches very high levels, located between 2500 and 3000 °C; at these temperatures, more than half of the water molecules are decomposed into elemental or molecular hydrogen and oxygen. The main drawback concerning this technique is the great tendency of the gaseous product to recombine while cooling, forming H_2O molecules once again, and in order

to limit these phenomena selective membranes can be introduced in the system. *(24)*
(25)

2.3.2.5 Photoelectrochemical water splitting

In photoelectrochemical water splitting, the property of some particular semiconductor materials of being photoactive is exploited in order to make a redox reaction occur inside water, thus producing hydrogen. In a photoelectrochemical cell, the photoactive material is exposed to light, and if a photon with energy equal at least to the band gap of the material strikes the anodic surface, an electron-hole pair (EHP) is generated. The EHP is then exploited in order to obtain the dissociation of water. Holes and electrons originated in the photoactive material are separated; while the former remain located at the anode, where they split water into molecular oxygen and H^+ ions able to travel through the electrolyte, the latter flow through an external circuit to reach the cathode, where they finally produce molecular hydrogen upon interaction with the H^+ ions. The O_2 originally produced at the anode remains dissolved inside the water or is liberated in gaseous form as a byproduct. *(24)*

The mechanism of this process can thus be seen as a combination of an electrochemical and a photovoltaic one; there's in fact presence of redox reactions, but the energy necessary for them to take place is taken from photons of light striking the photoelectrodes, rather than from an electrical energy source. The choice of the semiconductor material is therefore of crucial importance. As it will be clarified later, it must in fact have an appropriate band gap value, together with suitable locations of the CB and VB edges, E_{CB} and E_{VB}. If the conditions are satisfied, the oxidation and reduction reactions described above can take place upon photoactivation of the material, giving:

$$photo-oxidation\ of\ water: \ 2H_2O + 4h^+ \rightarrow O_2 + 4H^+$$

$$photo-reduction\ of\ water: \ 2H_2O + 2e^- \rightarrow H_2 + 2OH^-$$
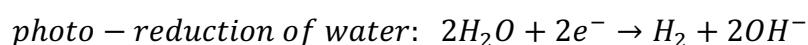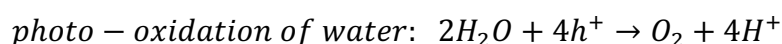
A small bias can be applied to the system in order to help the hydrogen production in case that the electronic bands of the material are not positioned in an optimal way. This situation is known as bias-assisted photo water splitting. *(25)*

2.3.3 Hydrogen storage

The most critical issue regarding hydrogen technology, which must be solved for it to obtain a larger spread and become an economically viable source of energy, is represented by the absence of a reliable storage system, considerably reducing the applicability of hydrogen related devices. *(26)*

One of the reasons for this is the fact that hydrogen, despite presenting the highest energy per mass amongst all fuels, has very low density at ambient temperature. This results in a too low energy per unit volume, which translates to needing large containers in order to have a suitable amount of energy for most applications. Moreover, hydrogen presents additional problems, like its high reactivity and its bad influence on many other materials (hydrogen embrittlement phenomena are an example). Considering this, the development of efficient storage methods able to concentrate good amounts of energy density is much needed for hydrogen's advancement. *(27) (28)*

2.3.3.1 Physical hydrogen storage

There are three possible storing modalities belonging to this category, which are:

- compressed gaseous hydrogen, which consists in compressing the H_2 gas molecules at pressure values between 35 and 70 MPa at room temperature;
- liquid hydrogen, where the gas is brought into a liquid state, thanks to a temperature around -253 °C and a pressure around 1 MPa;
- cryoadsorption, in which the gas is stored exploiting its adsorption on a high surface material at a temperature of -193 °C.

These are all examples in which there is no formation of any type of chemical bonding between the hydrogen and the hosting structure, so the release of H_2 molecules can be simply triggered by rising the temperature or lowering the pressure (opening a canister for example). Among the three ways presented to physically store hydrogen, the compressed gaseous storage is the most adopted one, simply because it doesn't require very low temperatures in order to be applied, at the more reasonable cost of high-pressure values. *(28)*

2.3.3.2 Chemical hydrogen storage

The chemical way generally offers better performances in comparison with the physical one, because of the strong binding of hydrogen and the ability to allow high densities. A big limitation is however represented by the regeneration of the materials used for this purpose, which is rather expensive and energy consuming. *(27)*

An example of chemical storage method used for hydrogen is the one of metal hydrides, which are compounds of one or more metallic cations (M^+) combined with a suitable number of hydride anions (H^-). Most metals strongly bind with hydrogen under the influence of high pressure, with hydrogen occupying interstitial sites in the metal's lattice, resulting in very stable compounds needing temperatures above 100 °C in order to be broken. In wider terms, any metal with a redox potential below H^+/H_2 system at a particular pH can be considered good for chemical hydrogen storage purposes, as the H_2 gets released upon reaction with water, leaving the metal oxide or hydroxide. *(25) (29)*

The design of practical hydrogen storage systems still remains an issue, but sodium borohydride ($NaBH_4$) has been extensively studied as a promising material for this purpose. This material is stable in standard conditions, and can be easily stored with the only precaution of placing it in an alkaline environment. In order to release the hydrogen, the substance is brought into contact with a catalyst, which is the main subject of research at the moment. *(30)*

The interaction between $NaBH_4$ and the catalyst causes the following reaction to occur:

$$NaBH_4 + 4H_2O \rightarrow NaOH + H_3BO_3 + 4H_2$$
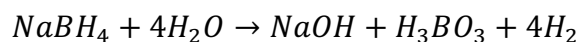
The use of salts of this kind for storing hydrogen is a promising technique, since it is possible to form aqueous solutions of them at room temperature very easily, thus forming a liquid source of hydrogen without the need of high pressures or extremely low temperatures, as in the case of physical storage. The limitation of this method is given by the high costs of the materials, together with the difficulties related to restoration of the borohydrides, and the fact that catalyst optimization hasn't been successfully optimized yet. *(28) (31)*

2.4 Photoelectrochemical cell (PEC)

Starting from the early 1970s, when the possibility of performing water splitting by using photoelectrochemical cells was first presented by Fujishima and Honda *(32)*, research has been very active around this subject. As anticipated in section 2.3.2.5, a photoelectrochemical cell (PEC), is a device able to convert energy coming from photons into chemical energy, through electrochemical processes induced by light striking its photoactive electrodes. The energy thus produced can be used in order to perform water splitting in aqueous solutions. *(32)*

The first example provided by Fujishima and Honda, consisted of an n-type photoactive anode (composed of TiO_2) connected to a platinum back electrode through an external circuit. Upon irradiation of the photoanode, a current flow was established, with holes inducing oxidation reactions (oxygen evolution) at the photoanode surface, and electrons participating to reduction ones (hydrogen evolution) at the cathodic site. The great importance of this experiment consists in the demonstration of the fact that visible light alone is enough to decompose water into O_2 and H_2, so there's no actual need for any external voltage. *(32)*

Different PEC configurations have been developed starting from this one, but the following description will mostly analyze the case of a single photoanode connected to a metallic counter electrode, addressing the other numerous possible situations in section 2.4.5. Each one of them has different peculiarities, but the aspects related to

the conditions for the functioning of the photoelectrochemical apparatus can be equally explained considering any of the configurations.
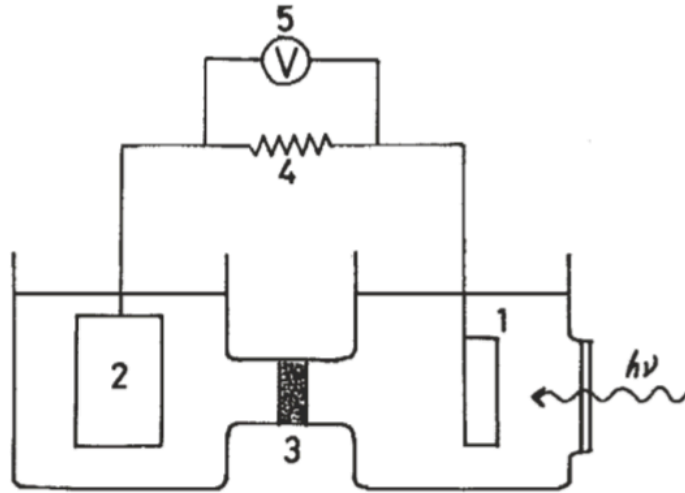
Figure 14. The configuration used by Fujishima and Honda for their experiment in 1972. **(32)**

2.4.1 Photoelectrochemical principles

As evident from figure 14, water splitting in a PEC is conducted with a configuration which is very similar to that of the purely electrolytic case discussed in section 2.3.2.3, but there are some fundamental differences in order to make the process happen without the application of any potential difference external to the system. The presence of at least one photoelectrode, made of a semiconducting material, is instead exploited in order to produce the electrical energy needed for the splitting of water, as previously mentioned. The conversion of light into electrical energy takes place when photons of suitable energy (equal at least to the E_{BG} of the material, as explained in section 2.3.2.5) strike the photoelectrode, thus originating an electron-hole pair. The two charge carriers are then separated thanks to the electric field generated by the intrinsic band structure of the semiconducting material; in the case of an n-type material (constituting the photoanode), electrons are forced to move towards the cathode by flowing inside an electrical contact, while holes stay located at the anode to oxidize water into H^+ and O_2. It must be said that single photoelectrode configurations are realizable also with

29

the use of a p-type semiconductor functioning as the photocathode of the cell, in a sort of symmetrical way with respect to the situation just described. *(33)*

The functioning of a photoelectrochemical cell relies on the electronic properties of the photoelectrode materials and of the electrolyte (which in this case is water), and more in particular on their electronic structure. The generation of EHPs, and the whole process of water oxidation, take in fact place at the photoanode-electrolyte interface, whose characteristics are of extreme importance, as it will be explained later. For any redox couple, it is possible to determine two values of standard potentials for the redox reactions at the electrodes, so one for oxidation and one for reduction. These two reactions create the conditions for a continuous transport of charge, but in order for it to be effectively guaranteed, proper band alignment of the semiconductor energetic levels is needed. It is in fact necessary for the minimum of the conduction band (E_{CB}) of the n-type semiconductor material to be placed at a more negative level with respect to the reduction potential of water (E^0 H^+/H_2), while at the same time the maximum of the valence band (E_{VB}) must be more positive than the water oxidation potential (E^0 O_2/H_2O); if this conditions are satisfied, the redox reactions take place spontaneously, being influenced by the electrochemical potential of the material. *(33) (34)*
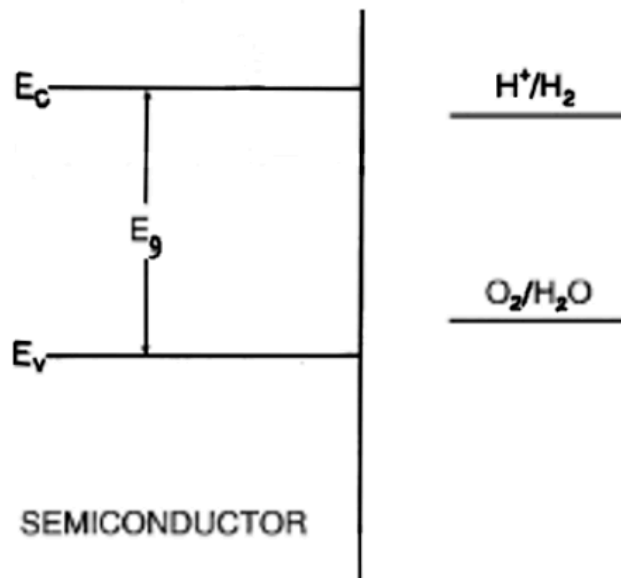
Figure 15. Band diagram of the n-type semiconductor photoanode in comparison with the standard potential values of the electrolyte's redox couples. **(35)**

The condition just explained only takes into account the band structure of the photoelectrode material to analyze the position of its band edges with respect to the standard potentials of the electrolyte. In order to establish a continuous charge transport, other conditions are actually necessary, such as the bending of the electronic bands at the surface of the photoelectrode, guaranteeing carriers separation. The overall stability of the semiconducting material in photoelectrolytic conditions and fast enough charge transfer of carriers are also important for the correct functioning of a PEC. All of these factors will be analyzed in the following sections. *(33)*

2.4.2 Reactions at the electrodes

Upon illumination of the photoelectrode, if the incident photon carries an energy $h\nu$ greater than the semiconductor's E_{BG}, an EHP is created. Considering the simplest PEC configuration, with only one photoelectrode (the n-type photoanode), the processes gives an h^+ (a photogenerated hole) for every incident photon. If the conditions described in the previous section are verified, the following reaction takes place at the anodic surface:

$$Water\ photo-oxidation:\ \ H_2O + 2h^+ \rightarrow \frac{1}{2}O_2 + 2H^+$$
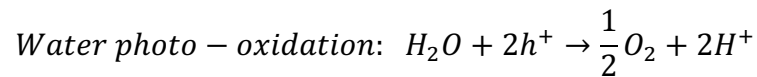
Electrons are not present in the reaction, as they flow through the external circuit to reach the cathode, participating in the underlying reaction:

$$Hydrogen\ reduction:\ \ 2H^+ + 2e^- \rightarrow H_2$$
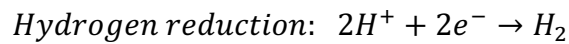
So the holes react with water at the photoanode-electrolyte interface, forming O_2 and H^+ ions; the latter migrate through the aqueous solution and undergo reduction at the cathode-electrolyte interface, finally producing H_2. The schematics of this whole process are shown in figure 16. *(33)*

In standard conditions, water can be reversibly electrolyzed if a potential difference at least equal to 1.23 V is applied. This value can be obtained by using Faraday's law:

$$\Delta G_0 = -nF\Delta E_0$$

in which n is the number of electrons involved in the process, F is Faraday's constant, ΔE_0 is the difference between the reduction potentials of the two reactions involved and ΔG_0 is the variation in Gibb's free energy associated to the total reaction. From these considerations, it becomes clear that in this configuration the water splitting can take place only if the photon carries an energy of at least 1.23 eV (or in other words the PEC must generate at least a potential difference of 1.23 V), which corresponds to the energy carried by radiations of wavelengths around 1000 nm, meaning that it is possible to decompose water with visible light. *(32) (33)*
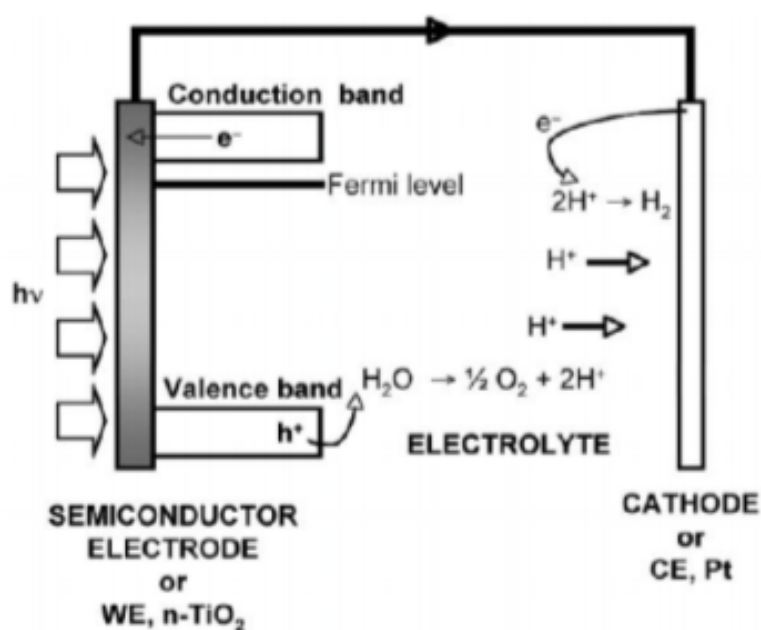
Figure 16. Redox reactions inside the PEC after EHP formation from illumination of the photoanode.

(33)

2.4.3 Band structure analysis

When a semiconductor is placed in contact with another material, having different chemical nature and electrochemical potential (so Fermi level), an electric field is originated as a consequence of the electrical differences across the interface. This is

what happens in the contact region between the photoelectrode and the electrolyte of a PEC, where the electric field acts in order to redistribute the charges and cancel the difference between the two Fermi levels, thus creating a condition of electrical continuity across the interface. This charge transfer stops once the electrochemical equilibrium is reached. *(33)*

The process described above results in the formation of a band structure which is very similar to the case of a Schottky barrier, generally formed at the interface between a semiconductor and a conducting material. The primary characteristic of a Schottky barrier is its height, indicated with the symbol $\Delta\phi_{SC}$, which corresponds to the difference in work function between the Fermi level of the bulk semiconductor and the interfacial E_{CB} (in the case of an n-type semiconductor), i.e. the level of the conduction band edge once charge transfer has reached an equilibrium. This situation is comparable to the one in a PEC, with the charge reorganization leading to an electric structure that causes the emptying of majority carriers in the surface region, while at the same time minority carriers are forced at the surface, forming a charged region called depletion zone. The effect leading to the formation of this zone depleted from majority carriers is known as band bending, since the E_{CB} of the n-type semiconductor literally bends creating a barrier to the passage of electrons, as shown in figure 17. *(33)*
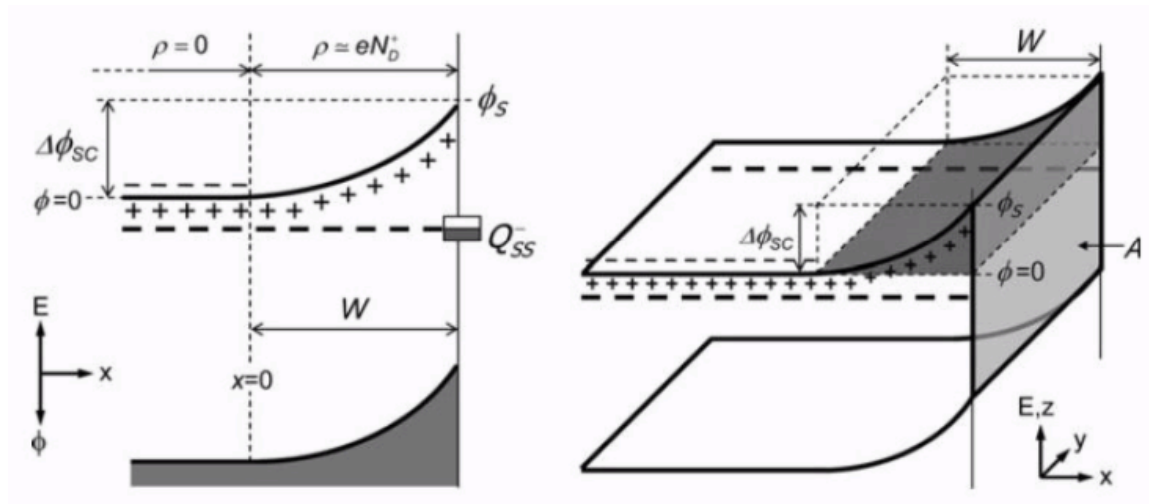
Figure 17. Electronic band structure at the surface of an n-type semiconductor electrode immersed in an electrolyte. Band bending with consequent formation of a depletion zone and potential barrier ϕ can be observed near the surface. **(33)**

This configuration is of fundamental importance for the functioning of the photoelectrochemical cell, because it guarantees the separation between electrons and holes at the photoelectrode-electrolyte interface. Because of the higher mobility allowed in the liquid phase, a net charge, constituted by ions of the same sign of the majority carriers, accumulates near the junction, forming the so-called Helmholtz layer. *(33)*

2.4.3.1 Surface hydroxylation at semiconductor-electrolyte junction

The semiconductor material in contact with the electrolyte is influenced by the solution's pH, which acts on superficial absorption of protons and hydroxide ions present in the solution. Since the species involved are electrically charged, these phenomena affect the potential distribution at the semiconductor-electrolyte junction. At a certain point after immersion, a dynamic equilibrium of absorption-desorption of H^+ and OH^- species onto the surface is reached, which can be described by the equations:

$$M - OH \leftrightarrow MO^- + H^+_{(aq)}$$

$$M - OH + H^+_{(aq)} \leftrightarrow M - OH^+_2$$
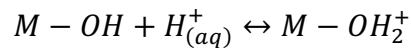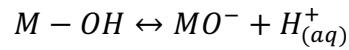
Depending on the electrolyte's pH, the total charge absorbed on the surface can be positive, negative or null. In particular, the pH such that the net adsorbed charge is zero is called point of zero charge (PZC) of the semiconductor. *(33)*

As a consequence of these processes, a charged layer on the semiconductor's surface is formed, with charges of one sign accumulated near the interface (electrode's side) and ionic species of the opposite sign in the electrolyte, as the equations written above indicate. Due to water's high dipole moment, ions in the electrolyte are surrounded by a cloud of H_2O molecules, which constitutes a form of steric hindrance that prevents the charged species from coming into direct contact with the ones absorbed on the surface, keeping them separated by a few ångströms. The region in between the

absorbed ions and the closest ones in solution is the Helmholtz layer mentioned in the previous section, formed as shown in figure 18. *(33)*
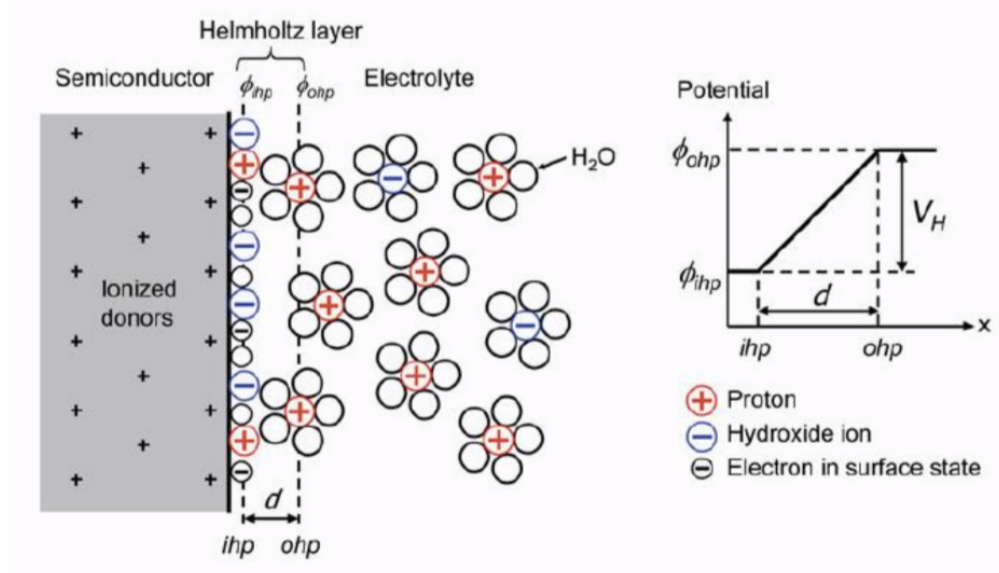
Figure 18. Semiconductor-electrolyte junction with schematic of the Helmholtz layer, where ihp stands for inner Helmholtz plane (absorbed) and ohp for the outer one. **(33)**

2.4.3.2 Potential drop

Because of the presence of ions completely surrounded by water molecules, a potential drop is present across the Helmholtz layer. The value of this difference, qualitatively shown in figure 18, is given by:

$$V_H = \xi d = \frac{Q_s d}{\varepsilon_0 \varepsilon_r}$$

where d is the Helmholtz layer's thickness, usually between 2 and 5 Å, ε_r, electrical permittivity of the electrolyte, is around 6 near the junction (while it's 80 in bulk water), and Q_S, which quantifies the surface density of charges, can be assumed as $\sim 10^{13}/cm^2$; considering these typical values, the potential drop across the layer can be assumed between 0.1 and 0.5 V. Considering the kinetics of the processes involved, the above equation can be rewritten as:

$$V_H = \frac{2,3kT}{e}(PZC - pH)$$

remembering that PZC is the pH value such that the net adsorbed charge on the semiconductor's surface is zero. For a temperature of 25 °C, this last equation gives a value of the potential drop equal to -59 mV for pH unit, with respect to the redox potentials of the electrolyte. *(33)*

2.4.3.3 Band diagram of the junctions

It is possible to determine the entire electronic band diagram of a PEC, with specific consideration of the junctions between electrodes and electrolyte. In this section in particular, the configuration with a photoanode and a pure metal as a cathode is analyzed, with the energy of an electron in vacuum at infinite distance taken as a reference. It is worth noting that this energy level bends in presence of an electric field, so in this case it follows the gradient present in the PEC in the regions near the junction, while it is taken as flat in the bulk electrolyte. *(33)*
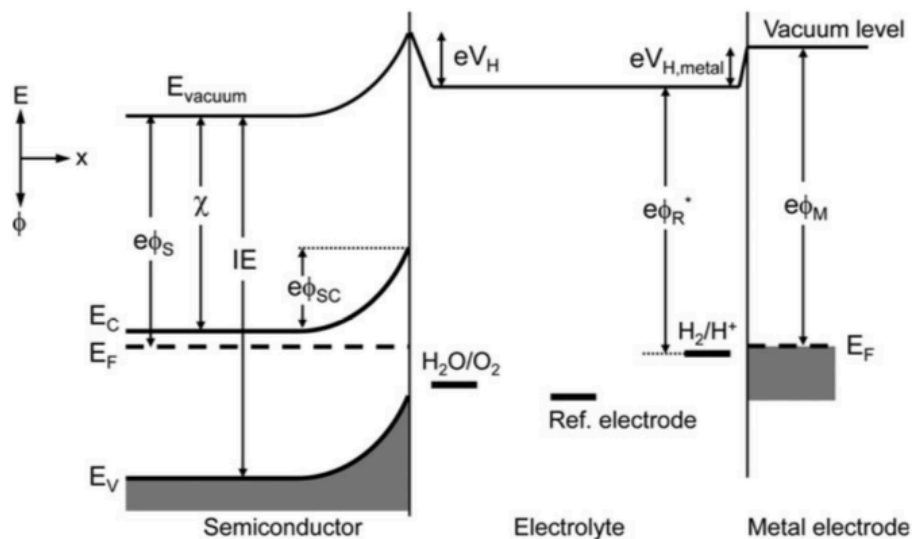
Figure 19. Band diagram of a PEC based on an n-type photoanode and a metallic cathode. **(33)**

Figure 19 shows the photoelectrochemical cell's electronic band diagram, also reporting some important parameters like the electronic affinity, indicated with χ and the ionization energy IE, which are constants related to the material of the photoanode, plus the semiconductor's work function ϕ_{sc} which depends on the distance from the surface. *(33)*

The useful parameters in order to qualify a semiconductor for photoelectrochemical applications are its band structure, the amount of bending it undergoes and the difference in potential energy between its E_{CB} and E_F, always considering the case of an n-type material. On the other end, to discriminate between different types of electrolyte, E_{ox} and E_{red} are the two energy levels to consider. E_{ox} is the electronic affinity of the oxidized specie, while E_{red} of the reduced one, and they're the main reference levels for a redox couple immersed in an electrolyte. The pH of the solution influences the oxidation and reduction potentials just as it does with the value of V_H across the Helmholtz layer, and this dependence is reported in the following equations:

$$E_{red} = E_{red}^0 - \frac{RT}{4F}\ln\left(\frac{p_{H_2}^2}{[H^+]^4}\right) = E_{red}^0 - \frac{2,3RT}{F}\left[\log\left(\sqrt{p_{H_2}}\right) + pH\right]$$

$$E_{ox} = E_{ox}^0 + \frac{RT}{4F}\ln\left(p_{O_2}[H^+]^4\right) = E_{ox}^0 - \frac{2,3RT}{F}\left[\log\left(p_{O_2}\right) - pH\right]$$

This means that the reduction and oxidation potentials of the redox couples in the electrolyte depend on the pH of the solution in the same way of the band positions, i.e. they vary by an amount of -59 mV per pH unit. As a consequence, the band positions of most metal oxides are fixed with respect to the water redox potentials. *(33)*

Photogenerated holes are able to oxidize water only if the energy associated to the H_2O/O_2 redox couple is energetically placed above the valence band, while at the same time only photogenerated electrons having energy higher than hydrogen's reduction potential can react to give reduction. Figure 20 shows a series of energy band diagrams for different semiconductors; a graph like the one represented, showing if a certain reduction or oxidation is thermodynamically favored, can be useful when deciding which semiconductor is the best fit, considering a certain electrolyte and its pH. *(33)*
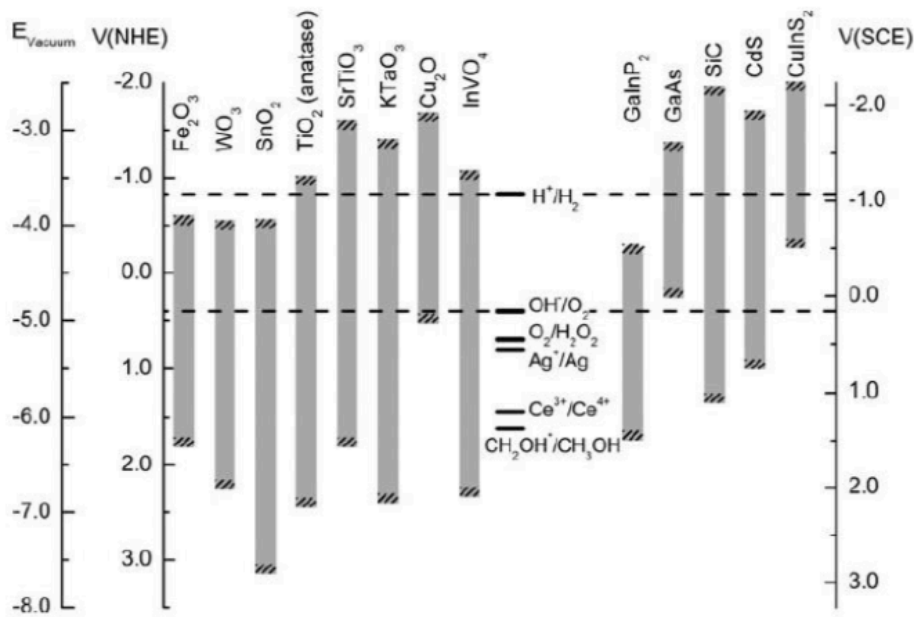
Figure 20. Band edge positions for a series of semiconducting materials in a solution at pH=14, compared with the redox potentials of water. **(33)**

The position of the band edges with respect to the redox potentials is expressed by the so-called "flat band potential", which corresponds to the value that would be needed to reduce the bending at the electrode-electrolyte interface to zero, i.e. flattening the band. Since this value corresponds to the Fermi level of the semiconductor, in the case of an n-type material it is located just below the conduction band edge, and it can accurately reflect the ability of the electrode to reduce water to hydrogen. *(33)*

2.4.3.4 PEC physics under operating conditions

In order to completely understand the functioning of a PEC, every step of the photoelectrochemical chain must be considered. In particular, the system's behavior must of course be studied under illumination. When the electrode isn't hit by light (dark condition), its own E_F level corresponds to the one of the metallic cathode, thanks to the presence of the electrical connection which allows charge transfer between the two (more precisely from the semiconductor to the metal) up to the point where their work functions assume the same value. At this point, the energy band diagram indicates that water decomposition isn't energetically favorable yet, since the potential

of the H_2/H^+ redox couple is still located above the cathode's E_F. When the PEC is exposed to light, electron-hole pairs are generated, with electrons in the CB and holes in the VB. Since this drastically change the distribution of charges in the semiconductor, it is convenient to define two different quasi-Fermi levels (one for the electrons and one for the holes), as done in section 2.2.1, as the energy at which the probability of occupation is 0.5 is different in the two cases. *(33)*
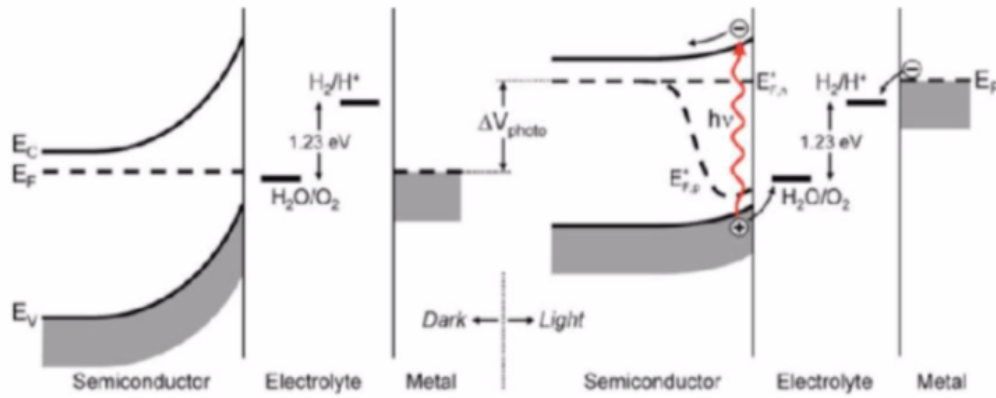
Figure 21. Band diagram of a PEC with an n-type photoanode and a metallic cathode in dark conditions (left) and under illumination (right). Minority charge carriers are photogenerated only on the right. **(33)**

It is possible to express the number of electrons and holes after exposition as:

$$n = n_0 + \Delta n$$

$$p = p_0 + \Delta p$$

in which n_0 and p_0 are the concentration of the respective carriers in equilibrium conditions, while Δn and Δp are the variations introduced by photogeneration of EHPs. For n-type semiconductors, $n \approx n_0$, since the photogenerated carriers are almost negligible with respect to those introduced by doping the material, so the quasi-Fermi levels of electrons remains flat upon irradiation, while the one of holes is changed (figure 21, right). As the electrons are kept far from the surface thanks to the bending of the potential, eventually flowing into the external circuit, holes are located near the junction, and react to oxidize water, as depicted in figure 21. For p-type

semiconductors the situation is of course reversed. It's worth mentioning that, for some type of photoanodes, light irradiation alone isn't enough to guarantee that the cathodic E_F is above the H_2/H^+ redox potential, so an anodic bias must be applied in order to make water splitting possible. *(33) (35)*

2.4.4 Photoelectrode requirements

Photoelectrodes constitute the most important aspect of photoelectrochemical devices. The most important requirements that need to be satisfied can be summarized as:

- good absorbance in the visible region of the spectrum;
- high chemical stability, both in dark and illumination conditions;
- suitable band overlapping with water oxidation and reduction potentials;
- efficient charge transport in the semiconductor;
- low cost.

The region of the spectrum in which the semiconducting material is able to absorb depends on its electronic band gap, with the minimum possible value in order to obtain water dissociation without application of an external bias being the difference between the potential values of the redox couples involved, so 1.23 eV. With this value taken as a reference, if thermodynamic losses and overpotentials are considered as well, the ideal band gap for a photoelectrode material is 1.9 eV, which corresponds to an onset of absorption around 650 nm. Moreover, considering that for the solar spectrum there's an abrupt drop in irradiance below 400 nm, the maximum acceptable bandgap for a semiconductor used in the photoanode must be lower than 3.1 eV, or EHPs can't be generated by solar irradiation. In conclusion, the bandgap of the photoanode material must be between 1.9 and 3.1 eV, which is an interval within the visible range of the solar spectrum. *(33)*

Another important feature is the chemical stability of the materials used. Most non-oxide semiconductors, once immersed in the electrolyte, either dissolve or form an oxide layer that hinders the passage of charges across the semiconductor-electrolyte junction, while some oxides can undergo photocorrosion phenomena. In any case, only a few materials fulfill the requirement regarding overlapping of energy bands with

water's oxidation and reduction potentials, and the ongoing research is mostly concentrated around metal oxides, because of their efficiency concerning charge transport, and the overall fulfillment of the above-mentioned requirements. To assess the quality of a semiconducting material for what concerns charge transport phenomena, intrinsic and extrinsic aspects must be considered; the former are governed by the band structure of the material, while the latter depend on the presence of recombination centers. The tendency to recombine is quantified via the average lifetime of carriers (τ_R), or alternatively through the minority carriers' diffusion length (L_D), which are in fact related by the equation:

$$L_D \approx \sqrt{D\tau_R}$$

in which the diffusivity of carriers D is related to their intrinsic mobility μ by the Nernst-Einstein equation:

$$D = \frac{kT\mu}{e}$$
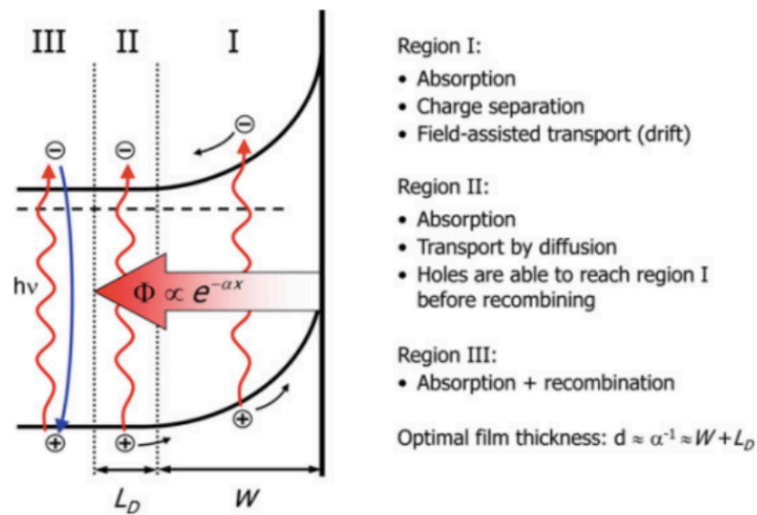
Figure 22. Absorption regions in a photoanode. Carriers can generate photocurrent only if originated in the right spatial conditions. **(33)**

By looking at figure 22, it can be said that only charge carriers generated within a distance L_D+W from the surface (regions I, II) will contribute to the generation of photocurrent, while those at longer distance undergo recombination. **(33)**

41

2.4.5 PEC configurations

When the electronic band diagram of the photoactive material does not efficiently overlap with water's redox potentials, the use of two or more different semiconductors can be applied as a strategy. In these cases, one of the two electrodes is a regular photoanode or photocathode, while the other is either the complementary photoelectrode or a device that provides a certain voltage. *(33)*
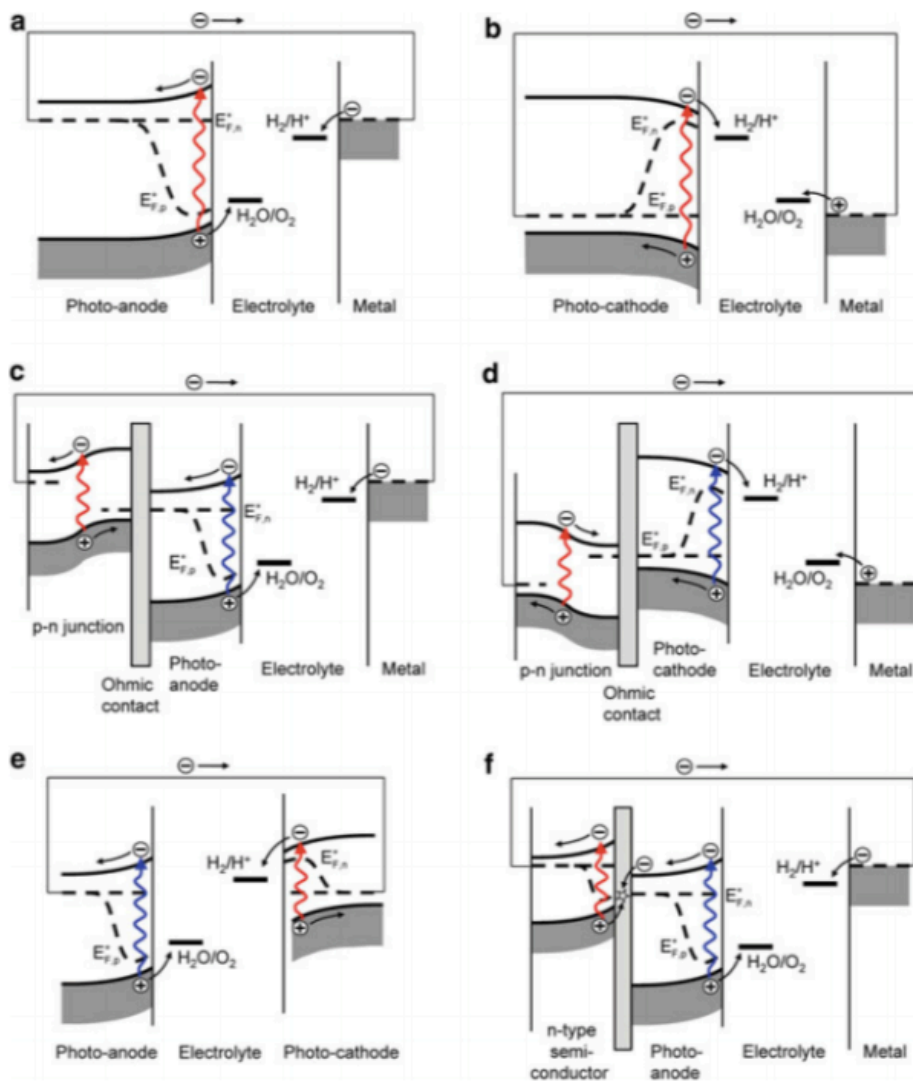
Figure 23. Different PEC configuration examples. **(33)**

The different possibilities, as shown in figure 23, can be: the most standard configuration with a single photoanode (a) or photocathode (b) paired with a metallic

counter-electrode; an embedded p-n junction able to generate a bias (basically a photovoltaic cell) over a photoanode (c) or a photocathode (d); a two-photoelectrodes PEC (e); a n-n heterojunction PEC in which the material for the photoanode is deposited on top of another n-type semiconductor which "boosts" the electrons thanks to a suitable band structure. *(33)*

2.4.6 Chemical degradation and photocorrosion

Durability of the components inside a PEC is one of the main issues related to photoelectrochemical water splitting. The main causes of photoelectrodes deterioration are chemical degradation and photocorrosion.

The first process is related to the stability of semiconductors when immersed in specific electrolytes, which depends on the solution's pH. To make a certain material utilizable in conditions of chemical instability, the most used solution consists in covering the photoactive layer with a protective one, even if this also means limiting the photoactive properties of the material. Usually, high band gap and chemically inert semiconductors are used, such as ZnO, TiO_2 and Ru_2O. *(33)*

Photocorrosion is instead a degradation phenomenon related to the fact that the photogenerated carriers could end up oxidizing or reducing the semiconductor itself instead of water. When a metal oxide is used for the photoanode, its anodic decomposition operated by holes (h^+) can be described with the reaction:

$$M_xO_y + \frac{2y}{x}h^+ \rightleftharpoons xM^{2y/x}_{(aq)} + \frac{y}{2}O_2$$
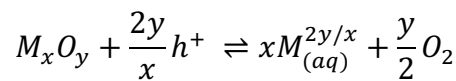
while for photocathodes, the corresponding reaction operated by electrons is:

$$M_xO_y + 2ye^- + yH_2O \rightleftharpoons xM_{(s)} + 2yOH^-_{(aq)}$$
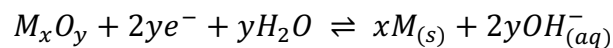
The equilibrium potentials of these reactions, which is in turn related to their Gibbs free energy variation, are the decisive factor in determining whether these undesired effects can occur or not. If the energy level for the anodic decomposition (E_{pd}) is below

E_{VB}, no decomposition can occur, while the same is true for a material at the cathode if the cathodic decomposition level (E_{nd}) is located above E_{CB}. Figure 24 illustrates the relations between material's band structure and photocorrosion reaction's potentials for a series of semiconductors. *(33)*
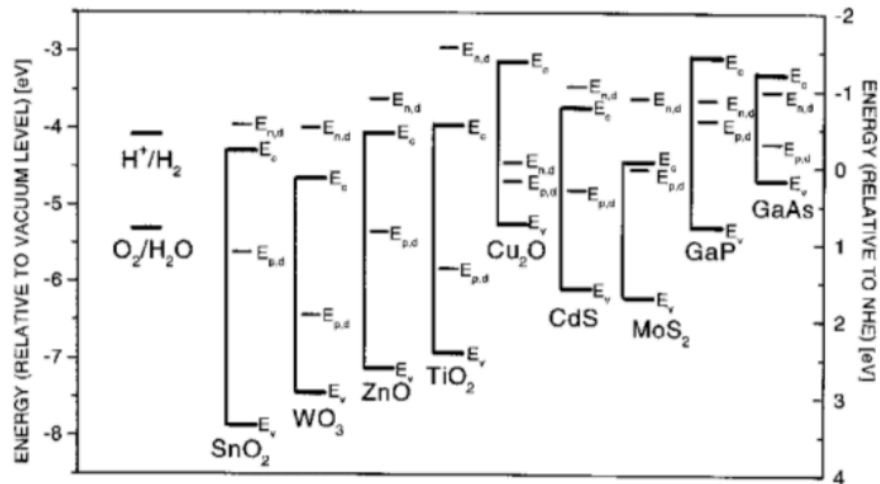
Figure 24. Relative positions of photocorrosion potentials and band edge levels for a series of semiconductors. **(33)**

2.5 BiVO$_4$

As mentioned in section 2.4.4, metal oxides are the main object of the ongoing research around semiconductors for photoelectrochemical applications, not only for their stability in water, but also because of their cost effectiveness and wide distribution of band gaps. Among these, bismuth vanadate received particular attention during the last decade, having provided great performances related to water oxidation. *(36)*

2.5.1 Crystal structures and electronic properties

Bismuth vanadate is an n-type semiconductor, which presents itself as a bright yellow solid composed of rather inexpensive materials. In nature, it can be found as the mineral pucherite, with an orthorhombic crystalline structure, but when prepared in laboratory, it assumes instead either a scheelite or a zircon-type structure. The scheelite

structure can have a tetragonal or a monoclinic crystal system, where in both cases each V ion is coordinated by four O atoms in a tetrahedral site, and each Bi ion by eight O atoms belonging to 8 different VO_4 units. The only difference between the tetragonal and monoclinic systems is that the local environments of vanadium and bismuth are more significantly distorted in the second case, producing a slight difference in the band gap values. The zircon-type structure can instead present only a tetragonal crystal system, in which once again V is coordinated by four O atoms and Bi by eight, but in this case the oxygen atoms surrounding bismuth ions come from just six VO_4 units, with two of them providing two atoms to Bi. This results in a distortion of the Bi-O bond, as shown in figure 25. *(36)*
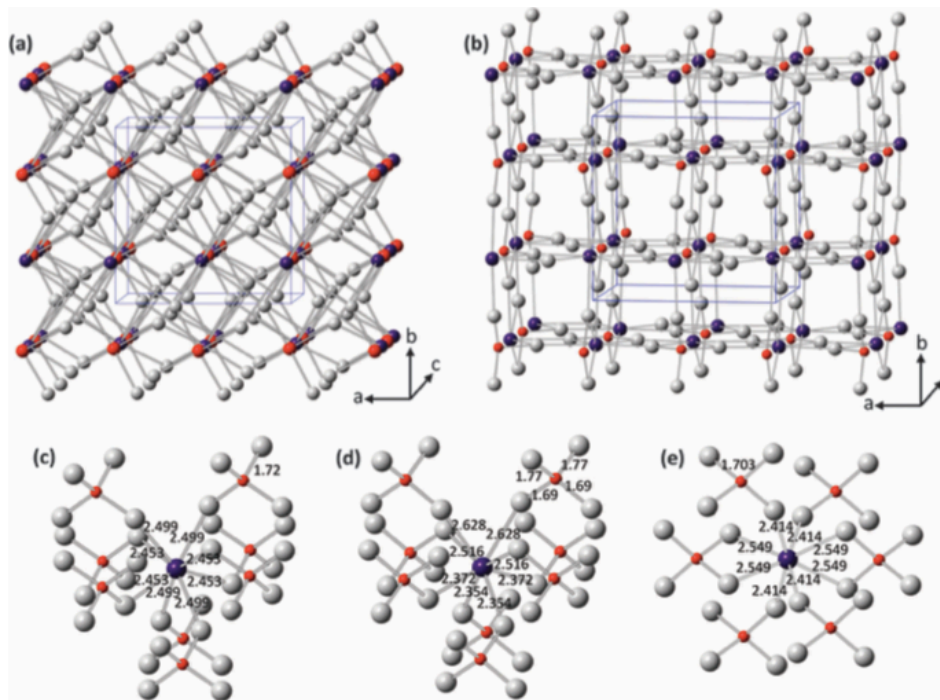
Figure 25. Crystal structures of BiVO₄ synthetized in laboratory: (a) tetragonal scheelite structure; (b) zircon-type BiVO₄; bond lengths (in Å) and local coordination of Bi and V ions for (c) tetragonal scheelite, (d) monoclinic scheelite, and (e) zircon-type BiVO₄ (red = V, purple = Bi, grey = O). **(36)**

Synthesis at low temperature, usually results in a zircon-type structure, but since the specific kinetics of each process play a critical role in determining the structure at low temperature, results may actually vary depending on the different production methods exploited. When instead high temperatures are employed, scheelite structures form; a monoclinic scheelite structure can be obtained starting from a tetragonal zircon-type

one with an irreversible transformation over 400–500 °C, while among scheelite structures a transition between tetragonal and monoclinic was reported to occur reversibly at 255 °C. *(36)*

Photoelectrochemical properties of $BiVO_4$ are strongly dependent on its crystalline structure. The highest activity towards water oxidation was reported for the monoclinic scheelite structure, in which better properties with respect to the tetragonal zircon-type one appear to be mainly due to the enhanced photon absorption, caused in turn by a band gap value of 2.4 eV, sensibly lower than the 2.9 eV of zircon-type structures. This difference in E_{BG} comes from the fact the transitions of interest take place between orbitals at different energy levels in the two cases; in fact, as shown in figure 26, the considered band gap for the zircon-type structure is the one between a 2p orbital of O and a 3d one of V, while for the monoclinic scheelite structure there's a 6s orbital of Bi, introduced at a higher level with respect to the 2p of O. This produces a difference in E_{BG} of 0.5 eV, making it possible to excite charges via absorption of lower energy radiations, so visible instead of ultraviolet. For what concerns the two possible scheelite structures, a higher activity is reported for the monoclinic one, with the difference mainly attributed to the higher extent of distortion of the metal polyhedra in the monoclinic case, as already mentioned; distortion produces a local polarization, which favorably affects the electron-hole separation effectiveness of materials. *(36)*
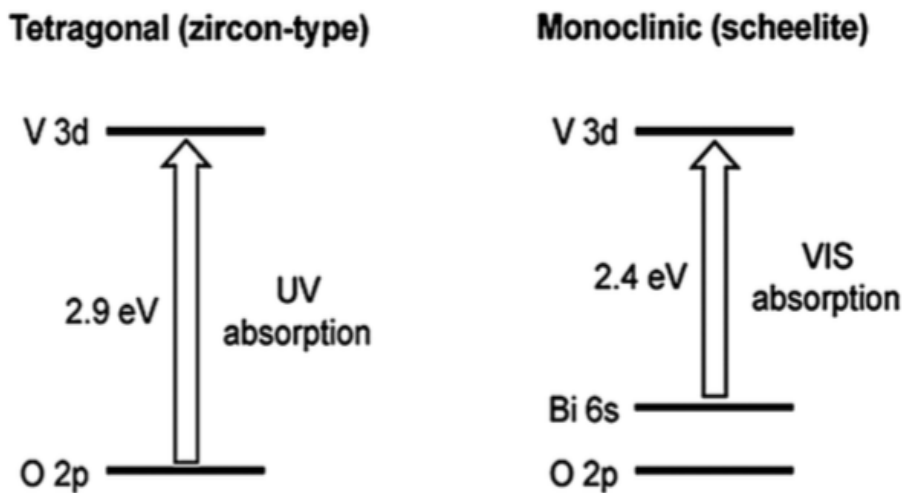
*Figure 26. Schematics of EHP formation for the tetragonal zircon-type and monoclinic scheelite structures. The difference in E_{BG} results in different type of radiations exciting the transitions. **(36)***

Some of the most important features that make bismuth vanadate stand out among other metal oxides for photoelectrochemical applications are:

- a 2.4 eV band gap value of the monoclinic scheelite structure, roughly corresponding to the absorption of radiations at 520 nm of wavelength, allowing good absorbance in the visible range;

- a sufficiently negative valence band edge position (2.4 V vs RHE) with respect to water's oxidation potential, providing a high enough overpotential for holes to oxidize H_2O at the anode;

- a CB level around 0 V vs RHE, having a thermodynamic level close to H_2;

- the effective masses of electrons and holes, which are estimated to be lower than in similar semiconductors (like In_2O_3 or TiO_2), resulting in easier separation and extraction processes for charged species;

- inexpensiveness of the elements in the compound;

- non-toxicity of the material. *(37) (38)*

For what concerns the value of E_{BG}, it is noticeable how the 2.4 eV of $BiVO_4$ is sensibly higher than the 1.9 eV ideally desirable for photoanode materials (as discussed in section 2.4.4). Nevertheless, it's the combination of the band gap value with the very negative position of the CB that makes bismuth vanadate preferable over other n-type semiconductors that can be excited through visible light. The biggest disadvantage is instead related to the surface, characterized by inefficient water oxidation kinetics, poor charge transport properties and high frequency of electron-hole recombination events. Approaches to overcome these problems include doping with other materials, nanostructuring and control of the morphology, formation of composite structures with other materials and superficial application of photocatalysts. Higher photocurrents are generally produced when these methods are applied, thanks to the increased absorption efficiency and the reduction of recombination events. *(36) (37) (39) (40) (41)*

2.5.2 Mo:BiVO$_4$

Doping of bismuth vanadate with metallic elements has been thoroughly analyzed in literature. The introduction of impurity atoms in the bulk, even in small amounts, can

dramatically change its electrical and optical properties, primarily acting on the band edges positions as explained in section 2.2.1. *(36)*

Among the possible dopants analyzed, molybdenum has proven to be the best solution for photoelectrochemical purposes, thanks to the fact that it enhances promotion of electrons in the CB, boosting the overall efficiency of the process. It is in fact a case of n-doping, since Mo atoms have one excess valence electron with respect to the V atoms they replace in the crystal lattice. Mo doping of $BiVO_4$ then results in the formation of energy levels located just below the original CB of the material, giving an increase in conductivity caused by the low energy required for electrons' promotion. The formation of impurity energy levels from substitutional Mo atoms arises from the hybridization of their 4d orbitals with the 2p ones of oxygen between the VB and the CB. The valence band's maximum and conduction band's minimum change with non-negligible effects on the band gap, so also optical absorption wavelength threshold does, explaining why $Mo:BiVO_4$ shows greater absorption in the 500-800 nm range when compared to pristine $BiVO_4$; the absorption onset can be originally estimated to be around 515 nm, while for the doped material it shifts to 530 nm, with absorbance increasing with the Mo content. *(41) (42)*
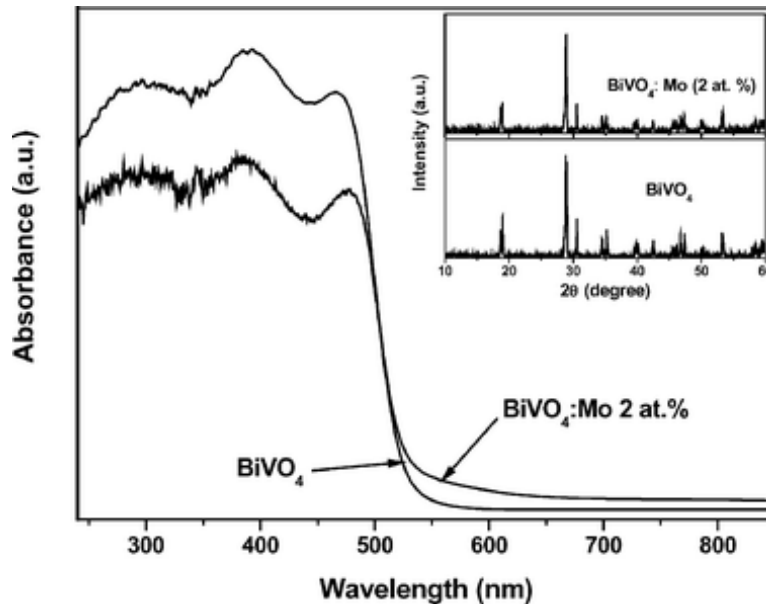
Figure 27. Comparison between the UV-VIS absorption spectra of BiVO₄ and Mo doped BiVO₄; the onset of absorption and the absorbance are different in the two cases. The top right corner shows the XRD spectra instead. **(43)**

However, the quantity of Mo introduced in the pristine material cannot be increased arbitrarily, since undesirable effect could arise from excessive concentrations. When doped $BiVO_4$ is produced, the amount of dopant present in the reaction mixture can be different from that effectively incorporated in the host structure. This is mainly due to the fact that residual dopant ions can form impurity phases on the surface or at grain boundaries, which may be too small even to be detected by XRD or EDS analysis. Presence of these secondary impurity phases can easily hinder charge transport or favor phase recombination, thus deteriorating $Mo:BiVO_4$'s photoelectrochemical properties. Anyway, ensuring the removal of impurity phases would maximize the effects of doping. *(36)*

For what concerns the crystal structure of doped $Mo:BiVO_4$, if calcination at 400 to 550 °C is performed on deposited films, the material tends to crystallize in the photoelectrochemically favorable monoclinic scheelite structure, with large, flake-like, single crystalline domains (having dimensions in the order of μm) showing good charge transport properties. Their growth is driven by grain boundaries elimination via coalescence or dissolution of smaller grains, lowering the Gibb's free energy of the system. Morphology can also be influenced by doping, as it has been shown how molybdenum doping can partially inhibit particle's growth, producing smaller but more homogeneous ones when $Mo:BiVO_4$ is synthetized in powder form, while in the case of production of thin films, increasing amounts of dopant tend to give smaller grains. *(42) (41)*

From Raman analysis, it can be seen how Mo^{6+} ions substitute V^{5+} ions in the crystal lattice. From a molecular point of view, this leads to a deformation of the lattice, due to the fact that the molybdenum ions have an ionic radius slightly larger than that of vanadium ones (measuring respectively 0.055 and 0.050 nm), which causes local compression strains and lattice parameters variations. *(36) (44)*

2.5.3 SnO_2 – $BiVO_4$ heterostructure

As mentioned in section 2.5.1, the formation of composite structures of bismuth vanadate and other materials can help improve its photoelectrochemical properties.

Photoelectrodes in which the main photon absorber is combined with a conductor or a semiconductor are in fact often exploited to enhance photon absorption, electron-hole separation, or charge transport processes, and in particular the coupling of $BiVO_4$ with other metal oxides has produced encouraging advancements for aspects related to the effective separation of charges. Among these, tin oxide has shown beneficial effects when a thin layer is placed in between bismuth vanadate and an FTO (Fluorine-doped Tin Oxide) substrate, due to the optimal alignment of undoped SnO_2's bands with those of $BiVO_4$. *(36)*

In fact, while Mo doping helps absorption behavior with a direct intervention on bismuth vanadate's band structure, the use of tin oxide acts instead on another important aspect influencing the overall efficiency, which is the limitation of charges recombination phenomena. Pristine $BiVO_4$'s surface shows in fact, as mentioned before, high frequencies of recombination events. This is primarily due to the formation of defect states (DS) at the interface between the photoactive material and the substrate, which in this case and for the majority of $BiVO_4$ photoanodes production is made of FTO. *(36)*

Electron-hole pairs are mostly generated at ~100 nm from the irradiated surface, depending on the penetration depth of light. The photogenerated electrons have then to travel across the thickness of the film, but when they reach the interface with FTO, they can fall into the DS instead of travelling through the external circuit. The accumulation of negative charges in this region causes a reduction of band bending, allowing holes to reach the defect state as well, giving recombination. The introduction of an undoped thin layer of SnO_2 can limit these occurrences, thanks to its optimal electronic band structure in combination with that of bismuth vanadate and FTO. In fact, its very positive potential value of the valence band edge efficiently functions as a hole mirror, blocking holes diffusion in the direction of the FTO, in a way "reflecting" them at the $BiVO_4 – SnO_2$ junction. *(36) (45)*

Through this mechanism, schematized in figure 28, the defect states cannot work anymore as recombination centers, because photogenerated holes cannot flow through the tin oxide layer, being literally separated by electrons at a higher degree than in normal $BiVO_4$ photoanodes. The result is of course manifested in a higher efficiency

of the device, since h$^+$ charges can be exploited for water oxidation at the photoanode-electrolyte junction, while electrons travel to the cathodic site. *(36)*
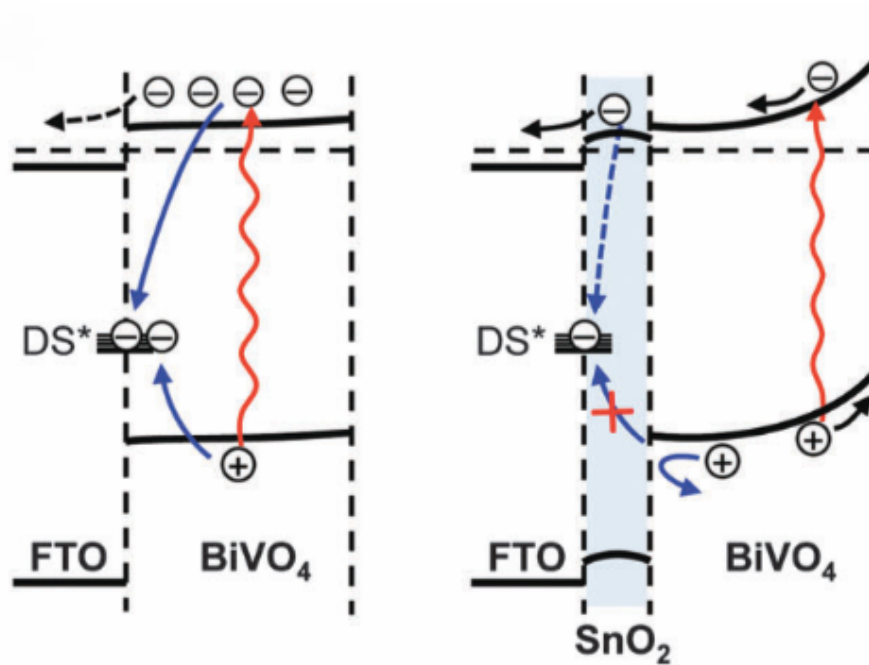
Figure 28. On the left, recombination phenomena at the BiVO4-FTO junction; on the right, SnO2 layer acting as a barrier for the diffusion of holes towards FTO, thanks to an optimal electronic band structure. **(45)**

Presence of the SnO_2 layer could also produce effects on the morphology of the $BiVO_4$ laying above it. It has been reported that even slight changes in the thickness of the hole-blocking layer can alter the photoanodic material in terms of crystalline phases, grain size and film roughness, ultimately influencing electronic properties as well. This possibility will be taken into account later on in this work, analyzing how the thickness of the buffer layer influence photoelectrochemical performances. *(46)*

3 MATERIALS AND METHODS

3.1 Synthesis methods

3.1.1 BiVO$_4$ thin film synthesis – Metalorganic Decomposition

A wide list of techniques for the production of BiVO$_4$ thin films is available. Among these, it is possible to find Metalorganic Decomposition (MOD) methods, which include different processes employed for the production of inorganic powders and thin films without the need of vacuum processes or gel preparation steps. MOD involves instead the dissolution of the metalorganic compounds of interest in a solvent and their deposition on a substrate. The deposition step can be carried out with any liquid phase film growth technique, like spraying, spin coating, drop casting or dip coating. The liquid film is usually heated at moderate temperatures at first, in order to cause solvents to evaporate, and then at high temperatures, depending on the level needed in order to trigger pyrolysis of the metalorganic precursors, leading to the final formation of an inorganic film over the substrate. This second stage, consisting in an annealing of the deposited material, can be tuned in order to influence some of the final properties of the produced film, like crystallinity, oxygen content and particle mean size, among the others. *(47)*

The advantages of metalorganic decomposition methods over other possible thin film production techniques can be briefly summarized as:

- ability to yield finely grained polycrystalline films with extremely uniform composition over large areas;
- high versatility, as it is possible to change the chemical composition of produced films with extremely high precision by varying the content of dopants in the formulation of the original solution;
- relatively low temperatures employed, with precursors that are rarely sensitive to moisturized environments, and can therefore be treated in open atmosphere;
- overall acceptable cost of common metalorganic reagents;

- potential for large scale applicability of many techniques, which is particularly interesting when considering production of photoelectrodes in high volumes for hydrogen production. *(47)*

Considering $BiVO_4$ thin films fabrication in particular, samples produced by exploiting this family of techniques show a characteristic porous morphology, which is actually an important feature when it comes to photoelectrochemical applications. The presence of micro and nanometer sized pores allows in fact a considerable increase of the area of contact between the active material of the photoanode and the electrolyte, leading to an automatic enhancement in terms of charge carriers transfer to the solution. *(48)*

For these reasons, metalorganic decomposition techniques have been the preferred method used for production of $BiVO_4$ and $Mo:BiVO_4$ thin films for this work. The fluorine-doped tin oxide (FTO) substrates used for fabrication of the photoanodes, having dimensions of 1.8 x 2 cm^2, were thoroughly cleaned before deposition processes via sonication for 5 minutes in a solution of 10 mg/L of Alconox® detergent powder followed by subsequent 5 minutes sonication in isopropyl alcohol ($\geq$ 99.8%; Sigma Aldrich).

3.1.1.1 Spin coating

Spin coating is a procedure used to deposit thin films onto a flat surface. A solution is dropped on the deposition substrate through the use of instruments allowing to leave just the right quantity on the surface, like pipettes, or micropipettes if a higher degree of precision is required for the application. The volume dropped ultimately influences the thickness of the produced film. The substrate is firmly secured onto a rotating plate thanks to a vacuum pump connected to the instrumentation, and it starts rotating with increasing speed, up to the point where it reaches the one (measured in rpm) set up by the operator. Rotation at high speed is needed in order to produce centrifugal forces allowing the liquid phase to spread evenly onto the substrate, with excessive fluid being spun of the plate's edges, until the desired film thickness is produced. Higher angular speeds of rotation lead to thinner films, but thickness depends on the dropped

solution's viscosity as well, being directly proportional to it. Solvents utilized for spin coating are usually volatile, so they can evaporate during the process. For these reasons, aspirators are exploited to avoid contamination of the environment or intoxication of the operators. *(49)*

Figure 29. Picture of the spin coater employed for this work. A vacuum pump was also linked to it through a plastic pipe, in order to keep samples in position during rotation.

For this work, the utilized spin coater was a Laurell ws-650 sz-8npp/lite. For what concerns production of $Mo:BiVO_4$ thin films, every deposition was carried out at a speed of 1000 rpm, for a period of time of 25 s and with an acceleration of 800 rpm/s. The solution was dropped just as the plate started accelerating, so that it was spun at the desired speed for the chosen period of time, considering that the final velocity was reached in less than 2 seconds. The quantity of material dropped onto the FTO substrate was of ~500 μL, considering that the excess of solvent would be pushed away from the specimen's surface by centrifugal forces acting while the plate spins. For deposition of multiple layers, the FTO was placed on a heating plate at 400 °C for 5 minutes after each run, in order to let the solvent evaporate and trigger crystallization of the material. Before depositing the subsequent layer, the sample was left to cool

down for a few minutes. The study of Byun et al. *(46)* was taken as the main reference for this part, with some changes adopted regarding the concentration of reagents in the utilized solution in order to obtain the desired increase in thickness at every deposited layer.

For spin coating production, two solutions were initially prepared, the first one being $Bi(NO_3)_3 \, 5H_2O$ (98%; Sigma Aldrich) 0.4 M dissolved in acetic acid (99.8%; Sigma Aldrich), while the second $VO(acac)_2$ (98.0%; Sigma Aldrich) 0.06 M, plus 1% $MoO_2(acac)_2$ (98.0%; Sigma Aldrich) with respect to V moles, dissolved in acetylacetone ($\geq$ 99.0%; Sigma Aldrich). The final solution utilized for spin coating of $BiVO_4$ was obtained by mixing the two above described mixtures in stoichiometric amounts, giving a Bi/V molar ratio equal to 1.1 in a 1% $Mo:BiVO_4$ solution.

Once the spin coating process was completed and the sample had cooled down after being placed on the heating plate for the last time, an annealing treatment was performed, which will be discussed later on.
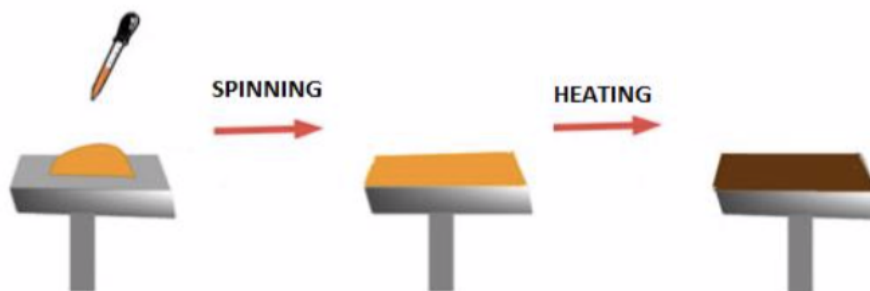
Figure 30. Schematics of the spin coating process for $BiVO_4$.

3.1.1.2 Drop casting

Drop casting technique was also employed in order to produce $BiVO_4$ thin films over fluorine-doped tin oxide substrates. The process consisted in the deposition of a precursor solution on a cleaned FTO, with the use of a micropipette. An important difference with respect to spin coating processes, is the fact that in this case the deposition is completely performed by an operator; therefore, while for spin coating

the final film's characteristics mainly depend on the solutions being used and on the parameters set on the instrumentation, for drop casting the influencing factors are of different nature. Since the objective of this work was the production of efficient photoanodes for photoelectrochemical water splitting, reproducibility of the samples was considered as an important factor, so uniformity of the deposited films was carefully evaluated. While for specimens produced via spin coating a good degree of uniformity was usually achieved, for drop casting ones it was instead a critical point around which much of the work dedicated to this technique was concentrated. The drying step was considered as an influent factor on uniformity; evaporation of the solvents can in fact produce defects in the deposits, so it is important not only to deposit a homogeneous layer, but also to have homogeneous evaporation along the whole surface of the substrate.

During the deposition step, particular care must be taken not to create irregularities in the thickness of the liquid layer, forcing the solution to diffuse all over the area of interest. Therefore, the results obtained after this stage heavily depend on the control of the operator performing the task, and on the formation of irregularities during the evaporation step.
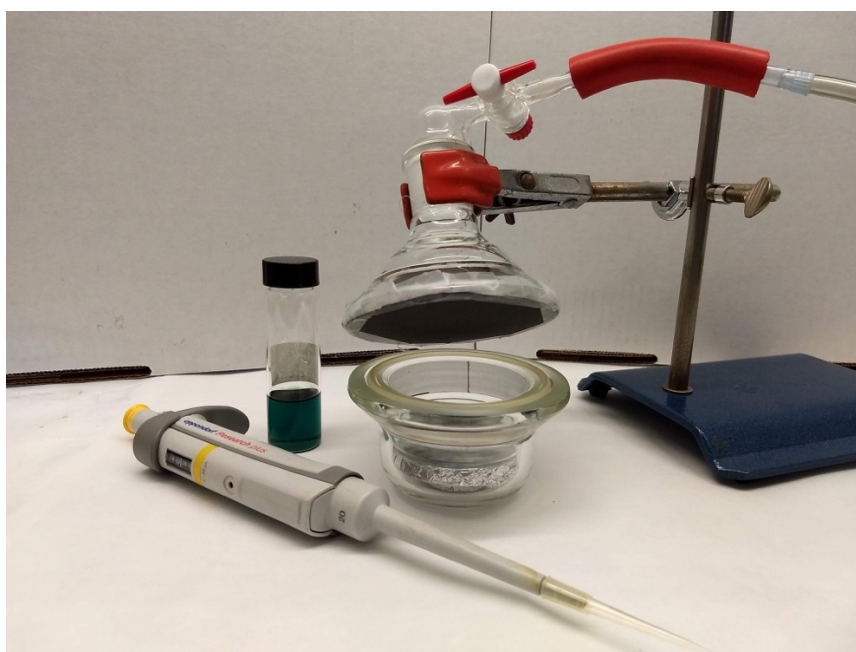
Figure 31. Instrumentation utilized for drop casting. The dropping process was directly performed inside the evaporation chamber in order to avoid any movement of the samples.

The main references for this part of experimentation were the works by Kim et al. *(40)* and Pan et al. *(50)*. For what concerns the solution deposited, it was prepared in order to obtain a final molarity halved with respect to the one utilized for spin coating. The drop casting method was in fact able to produce much thicker deposits after solvents evaporation, so the concentration of reagents was regulated taking that into account. The solution was prepared in an almost identical way with respect to the one utilized for spin coating. At first, a beaker containing $Bi(NO_3)_3$ $5H_2O$ (98%; Sigma Aldrich) 0.2 M dissolved in acetic acid (≥ 99.8%; Sigma Aldrich) and one with $VO(acac)_2$ (98.0%; Sigma Aldrich) 0.03 M, plus 1% $MoO_2(acac)_2$ (98.0%; Sigma Aldrich) with respect to V moles, dissolved in acetylacetone (≥ 99.0%; Sigma Aldrich) were prepared. The two described solutions were then mixed in the final one in stoichiometric amounts, obtaining a Bi/V molar ratio equal to 1.1 in a 1% $Mo:BiVO_4$ solution. The amount dropped over each sample was of 10 $\mu L/cm^2$, and this time a micropipette was used as mentioned above, since a higher level of precision is generally needed in drop casting processes with respect to spin coating ones, considering that the amount of dropped solution will effectively remain on the substrate instead of being partially spun away from it.
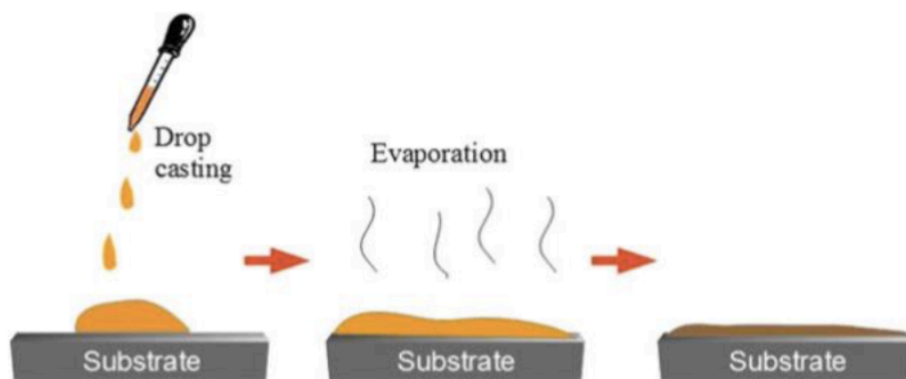
Figure 32. Schematic of the drop casting process, with the last step on a hot plate changing the color of the deposit.

Evaporation was carried out in a nitrogen atmosphere at low pressure, trying as much as possible to create the same conditions throughout the whole extension of the film-air interface. As for the time taken for this step, it was kept between 15 and 20 minutes, based on visual inspection of the samples to ensure the solvent efficiently evaporated.

After taking the specimens out of the evaporation chamber, they were quickly placed on a hot plate at 100 °C for just a couple minutes, in order to ensure elimination of solvents and to trigger a first crystallization of the film. The color of the deposit immediately shifted from the characteristic transparent green of the solution to a brownish one during this short time, after which the samples were ready to undergo annealing in the same way of the ones prepared via spin coating.

3.1.1.3 Introduction of a seed layer

A seed layer of $BiVO_4$ was introduced between the FTO substrate and the above lying film, as a way to favor nucleation of the phase deposited via drop casting. This step was performed through Sequential Ionic Layer Adsorption and Reaction (SILAR) method, which is a relatively easy and effective way in order to deposit nanosized particles of a material over a surface. The process is rather simple, and moreover it is completely performed at room temperature.

A SILAR deposition generally requires two different precursor solutions, and, as the name of the method itself suggests, cations and anions coming from the two solutions eventually react on the surface to produce the desired compound. Apart from two baths with the precursor solutions of the ions that must be deposited, two more need to be prepared with de-ionized water. The process begins then by immersing the substrate in the solution of the first precursor for a certain period of time; this passage produces adsorption of ionic species on the substrate's surface due to attraction forces between the ions in solution and the surface itself. After each absorption step, the DI water baths come into play, being used in order to eliminate any excess material on the substrate's surface. A certain rinsing time is in fact considered critical to obtain an optimal ionic layer formation, limiting this method's wastage of material and preparing the ionic surface for reaction in the third bath. After the first rinsing, the substrate is immersed in the second precursor solution, where the second ionic species is absorbed on the surface, bonding to the previously adsorbed counter-ions. A final rinsing step is once again required to eliminate excess and unreacted material. It is important to prepare two different DI water baths for rinsing after each ionic species

adsorption; this way contamination of both the solutions is avoided, and also there is no risk for the excess particles to bond with their counter-ions that may remain dissolved in water after earlier rinsing passages. The above described steps constitute one complete SILAR cycle, which theoretically deposits one monolayer of the desired material onto the substrate. Therefore, thickness of the film can be easily controlled by changing the number of deposition cycles, and, since only one monolayer is produced at each cycle, the degree of control is the best achievable. Factors affecting the growth phenomena are identified in the quality of the precursor solutions, their pH values and the concentration of the counter-ions in each of them, which is important to consider when deciding the time employed for each dipping passage. *(51)*

The main reference utilized for the deposition of the $BiVO_4$ seed layer for this work was the study performed by Odling et al. *(52)*, with some modifications regarding the formulation of the solutions employed and the thermal post treatment. The baths were prepared in order to have a precursor solution for the bismuth cations and one for the vanadium anions, in which the substrates were left for 30 seconds to obtain adsorption of the ionic species. The same amount of time was taken for each of the rinsing stages.
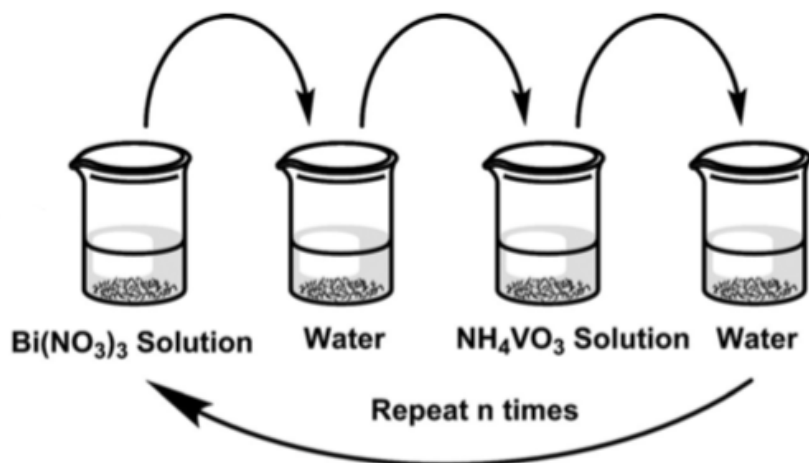
Figure 33. Schematics of the seed layer formation via SILAR method. **(52)**

For what concerns the actual formulation of the solutions for the two ionic precursors, the one for Bi cations was prepared by dissolving $Bi(NO_3)_3$ $5H_2O$ (98%; Sigma Aldrich) 10 mM into 2-methoxyethanol (99%; Alfa Aesar), while the one for V anions was obtained with NH_4VO_3 (≥ 99.9%; Sigma Aldrich) 10 mM in preheated DI water,

to help dissolution. Each cycle was performed first with the immersion in the cationic precursor solution, and then in the anionic one, with annealing on a heated plate at 550 °C for 20 minutes at the end of the last cycle, making solvents evaporate and triggering crystallization of $BiVO_4$ in its monoclinic scheelite structure, as explained in the work of Odling et al. *(52)*. A schematization of the process is shown in figure 33.

3.1.1.4 Tubular furnace

A tubular furnace is an instrument employed for thermal treatments at relatively high temperatures. The internal body of the instrument consists of a 30 cm long ceramic tube, inside which the temperature level can be controlled with appreciable precision. Since apertures are present at the two ends of the furnace, for the particular instrument utilized for this work nominal temperature set by the operator is effectively guaranteed only for a length of about 4 cm, 2 cm to the right and to the left from the very center of the tube. Among the different functions of a tubular furnace, the ones exploited for this work were the possibility to set a constant heating rate to reach the final temperature and the maintaining of that value for a desired amount of time. The interval of temperatures that the instrument is able to produce ranges from 30 °C to well above 1000 °C, allowing great versatility for treatments like soft annealings, oxidations, carbonizations etc.

Tubular furnace processes for samples are made possible through the use of quartz tubes; the specimens that must undergo thermal treatments aren't in fact placed directly in contact with the ceramic material, but lay instead inside a quartz tube closed at one end, and having a diameter slightly smaller than that of the furnace's cavity, allowing easy introduction and extraction for the operator. This tube must of course be resistant to high temperatures and thermal shocks. It is also possible to perform thermal treatments in controlled atmospheres, and that is easily done by applying a cap to the open end of the quartz tube, which can be then connected to conduits to create the desired gaseous atmosphere. Finally, it is important to know that the majority of thermal treatments in tubular furnaces require an air aspirator to be placed near the

open side of the quartz tube, to avoid contamination of the environment by removing gaseous byproducts developed during processes.
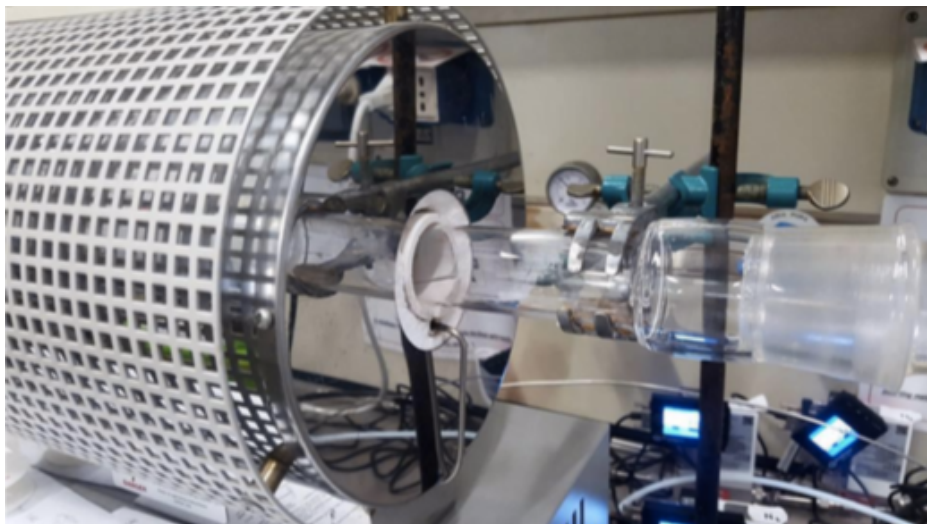
Figure 34. Tubular furnace at the open end of the quartz tube.

For what concerns this work, the only thermal treatment that was performed with a tubular furnace was a calcination, in order to completely eliminate all of the possible residual solvents and trigger the recrystallization of $BiVO_4$ and $Mo:BiVO_4$ in their monoclinic scheelite form. Once the thin film is produced via spin coating or drop casting method, the sample is placed inside the quartz tube, which of course goes into the tubular furnace. The operator must ensure that the specimen (or specimens) is placed within the 4 cm around the center of the furnace, since that's the region where nominal temperature is guaranteed, as explained above. Since calcination takes place in air, there's no need to put a cap on the open end of the quartz tube, and the process can be performed at atmospheric pressure. The main references used for this step of the synthesis were the studies conducted by Kim et al. *(40) (53)* and by Pan et al. *(50)*. Therefore, the heating ramp was set at 10 °C/min to reach a temperature of 550 °C, which was then maintained for 25 minutes. Samples were left to cool down inside the furnace (so still in open air) while its temperature decreased and taken out once the instrument showed a level close to room temperature. After the treatment was finished, solvents were completely eliminated from the surface, and recrystallization of the material into the photoelectrochemically efficient monoclinic scheelite structure was achieved.

3.1.2 Heterojunction with SnO_2

In order to enhance the photoelectrochemical performance of the produced photoanodes, heterostructures with a thin layer of tin oxide laying between the FTO substrate and the $BiVO_4$ film were realized. As explained in section 2.5.3, this was done in order to reduce as much as possible charges recombination phenomena across the $BiVO_4$-FTO interface. For the realization of the SnO_2 thin films, a spin coating method was adopted, with the main references being the studies of Byun et al. *(46)* and Luo et al. *(54)*, but the formulation of the utilized solutions and the parameters with which the spin coater was set were changed, both in order to optimize the production process and to study different effects regarding the efficiency of the hole-blocking layer in heterojunction with bismuth vanadate.

The instrumentation used for fabrication of these films consisted in the same spin coater mentioned in section 3.1.1.1, and the solution was dropped on the spinning substrates in a volume of ~0.5 mL for each run, by means of a plastic pipette. In fact, also in this case there was no need of high precision for this quantity, as the excess solution was spun away thanks to centrifugal forces, with final thickness of deposited films eventually determined just by speed and duration of the process. The SnO_2 precursor solutions were prepared by dissolving $SnCl_2$ $2H_2O$ (98%; Carlo Erba Reagents) 0.1 M and 0.2 M in isopropyl alcohol ($\geq$ 99.8%; Sigma Aldrich). It was decided not to perform spin coating deposition right away, but instead to leave the solutions under stirring conditions for a 36 to 48 hours period, the reason being a visible shift from an opaque to a very clear aspect over the course of the mentioned period. The spin coater was set to spin for an interval of 30 s, while the speed was varied between 500 and 3000 rpm, in order to produce the desired thickness. As it was done for $BiVO_4$ films deposited via spin coating, also in this case, when deposition of multiple layers was performed, samples were placed on a hot plate in between consecutive runs, in order to make the solvent evaporate. The temperature set for this step was of 150 °C, which was enough to get evaporation in a few minutes, without compromising the deposit. Between deposition of consecutive layers, samples were left to cool down at room temperature. An annealing treatment was present in this case as well, but a heating plate was exploited in place of the tubular furnace, with the

produced samples placed in open air at a temperature of 500 °C for 1 hour, and then left to cool down again in open air.

3.2 Analysis instruments

3.2.1 Linear Scan Voltammetry (LSV)

Linear scan voltammetry (LSV) is an analysis method in which the current flowing at one electrode of an electrochemical cell is measured, while its potential with respect to a reference electrode is varied linearly in time. Through this analysis, it is possible to obtain information about oxidation and reduction of chemical species in real time, by observing the peaks appearing in the graphs. Because of its field of investigation, this technique is heavily adopted to study the behavior of electrochemical systems. By imposing a decreasing potential, every peak with negative current values can be associated to a reduction phenomenon, while positive current ones indicate oxidation reactions. Another important technique used very often in electrochemistry is the cyclic voltammetry (CV). It is very similar to LSV, with the difference that in LSV a singular scan is performed between two potential values, while in a CV the potential shifts back and forth from one value to the other, even for multiple times if necessary. This allows to study the behavior of an electrode both as anode and cathode. *(55)*

For what concerns this work, linear scan voltammetry represents the main technique adopted to characterize the photoanode samples (from the point of view of photoelectrochemical efficiency) produced for potential use in PEC systems for water splitting. Tests were performed by observing the variation in electrical current output that the samples produced while being illuminated by a light source at AM1.5 (closely reproducing the Sun's radiation spectrum at the latitudes of most of world's largest population centers, as evident from section 2.1.1), with a variable bias being applied to the system at the same time. Considering the principles of LSV, higher values of measured anodic current correspond to a higher produced photocurrent of the photoanode when applied in photoelectrochemical water splitting.

3.2.1.1 Measurements apparatus

The setup for LSV analyses requires a potentiostat and a three-electrode setup to deliver electric potential to the solution. While testing, the output current graph vs applied voltage is represented via dedicated software. In the analyses performed for this work, the three electrodes being immersed in the electrolyte were:

- the working electrode (WE), which was of course the n-type semiconductor photoanode, able to produce electron-hole pairs upon illumination with radiation of suitable energy. The electrochemical study took place at the WE, and it consisted of an oxidation process (while in the case of a photocathode it would be a reduction one);

- the counter electrode (CE), which was a catalyst material, and in particular Pt. At the CE, the opposite process, with respect to the one at the WE, takes place;

- the reference electrode (RE), which was the Ag/AgCl one, and whose function is allowing a precise identification of the potential at the WE. The power generator will produce a value of potential which is set up by the operator and calibrated over that of the RE. It is also possible to control the rate at which the potential changes value, i.e., the "scan rate" of the test, measured in mV/s. *(55)*
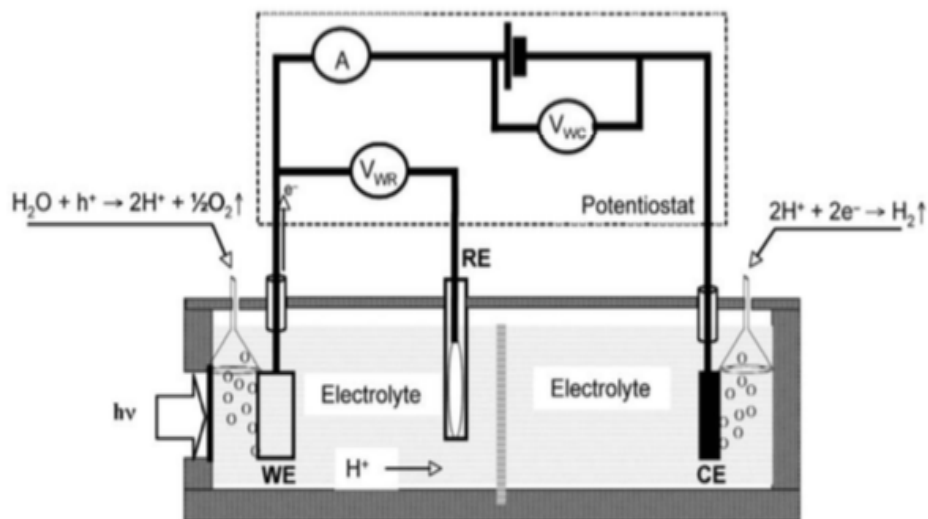
Figure 35. Schematics of a three electrodes cell for photoelectrochemical efficiency assessment. **(33)**

A photoelectrode, when illuminated by the sun's radiation, as reported in the previous chapter, produces a photogenerated current that depends on different parameters, such as band gap of the semiconductor, absorbance, etc. In order to have photocurrent, it is necessary to bring the system out of equilibrium, in a state of quasi-equilibrium, which is done by illuminating it. This is important because in this condition the electrode can exploit a voltage that rises due to the presence of a difference in the chemical potential value for holes and electrons. There is another way to bring the system out of equilibrium, consisting in application of an external bias; applying a potential can force electrons to flow in a desired direction. So LSV technique is a convenient way to measure the amount of current photogenerated by a photoelectrode, at different values of external bias applied. In this case, what is measured is the difference in current read by the instrument between periods of time when the photoelectrode is illuminated and when it is in dark conditions. *(55)*
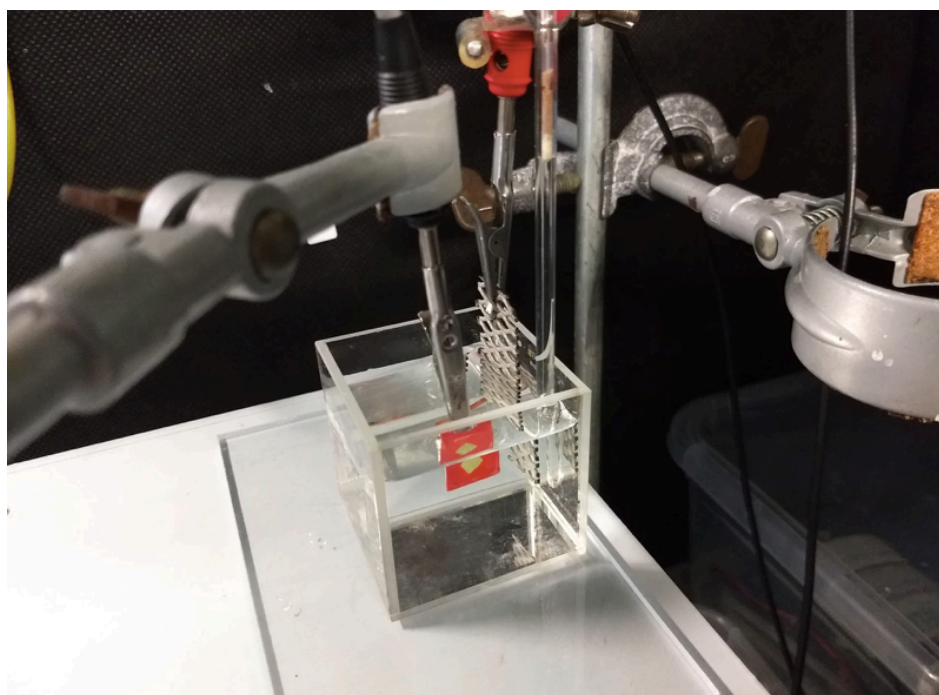
Figure 36. Setup utilized for LSV testing. Only a selected area of the photoelectrode's surface is left exposed to light, in order to evaluate the photocurrent produced by the homogeneous part of the film.

As described in chapter 2, the type of electrolyte chosen for testing, and its pH in particular, also influences the results, acting on the band structure of the system. For what concerns this work, the electrolyte utilized was a solution containing a

phosphates buffer, with 0.25 M K_2HPO_4 and 0.25 M KH_2PO_4, at pH 7, and 1 M $NaSO_3$. This solution was chosen because of the fact that in this situation sodium sulfite acts as a hole scavenger, with its oxidation being highly favored over oxygen evolution. This allowed the evaluation of the material's photoconversion ability in absence of surface catalysts. As for the electrodes, the reference one was an Ag/AgCl electrode in a 3 M KCl solution, while the CE was a Pt coated titanium net, with a greater area than the tested photoanodes. This aspect, and the fact that Pt acts as a catalyst for the hydrogen reaction, guaranteed testing conditions in which the performances weren't limited by the CE. The power generator utilized for this work was an AMEL 2553 potentiostat/galvanostat. This machine is able to measure the potential between two electrodes while a certain current is flowing (galvanostatic mode), or alternatively it allows to impose a potential at the WE to then measure the current flowing in the system (potentiostatic mode). For LSV tests, the potentiostatic mode was of course the one of interest, with the potential scanning between two imposed values as explained before.

The potentiostat was set up in order to impose a scan rate of 20 mV/s over the working electrode, with the starting potential value being the open circuit voltage, and the final one 700 mV vs Ag/AgCl. This interval was chosen because the reference value of photocurrent taken under consideration for the above described solution was located at 600 mV vs Ag/AgCl, which corresponds to 1.23 V vs RHE (Reversible Hydrogen Electrode), the thermodynamic potential of oxygen evolution in standard conditions, commonly used in literature as benchmark value for the comparison of the performances of photoelectrodes.

This correlation is obtained thanks to the following equation:

$$V_{RHE} = V_{Ag/AgCl} + 0.21 \, V + 0.059 \, pH$$

in which 0.21 V is the conversion factor reported in the reference electrode scale (as shown in figure 37) and 0.059 pH represents the logarithmic term of the Nernst equation.
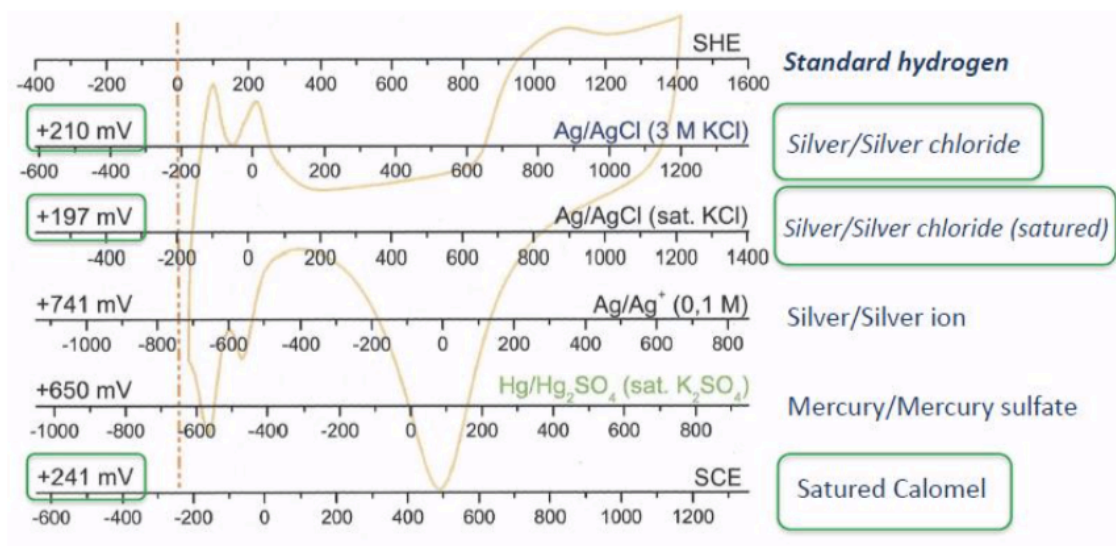
Figure 37. Potential scale for different reference electrodes. **(56)**

Measurements were taken both as the samples were illuminated and in dark conditions, in order to evaluate the difference in photocurrent produced by each sample at any value of the potential scan. The photocurrent produced in dark conditions is referred to as "dark current", and, in order to evaluate the electrode's photoelectrochemical efficiency, its value at a given potential must be subtracted from the corresponding one in conditions of illumination.

For every sample, the test was carried out both in front and back illumination conditions, i.e., with light striking the upper surface of the electrode (the n-type photoactive material) and its back (the opposite part, consisting of the back of the FTO substrate). What is different in these two situations is the entity of the path that charge carriers have to follow; in fact, EHPs are generated at different distances from the photoactive material's surface, meaning that they will have to cover different lengths, and in particular they will have different recombination probabilities, which in turn influence the measured photoelectrochemical efficiency of the photoanode being tested, since a lower number of recombination events would give higher photocurrents. As it will be reported in the experimental analysis section, by looking at LSV curves these differences were more or less obvious, depending on each sample's particular structure and methodology of fabrication.
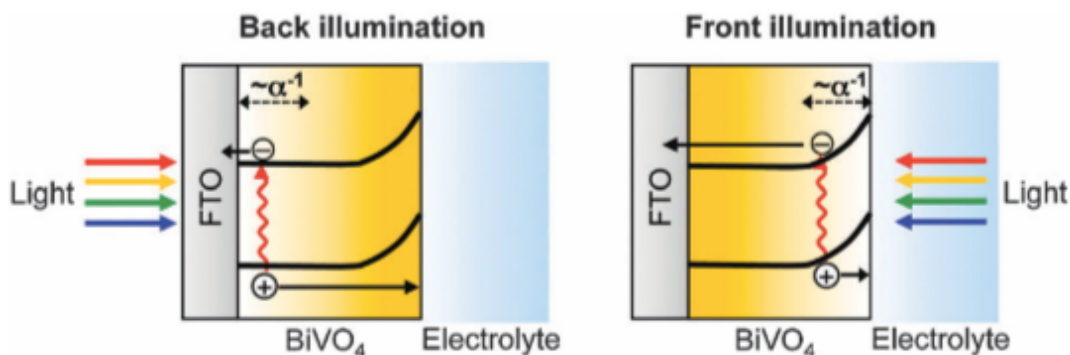
Figure 38. Schematics of the different paths that charge carriers have to follow in the case of back (left) or front (right) illumination conditions. **(36)**

Many studies reported that bare $BiVO_4$ electrodes generate a higher photocurrent with back illumination than with front illumination. As shown in figure 38, EHPs are generated near the back contact in the first case, while in the second they originate near the semiconductor-electrolyte junction. Then holes diffuse towards the surface, while electrons flow to the back contact and the electrical lead, thanks to the electronic band structure of the photoanode material. Higher values of produced photocurrents in back illumination indicate that slow electron transport is one of the limiting factors for $BiVO_4$ photoanodes. In any case, doping and formation of heterostructures can somehow limit these differences between the two situations, thanks to the better charge mobility and limitation of recombination phenomena they produce. *(36) (45)*

3.2.1.2 Solar simulator

In order to perform tests of photoelectrochemical water splitting with the produced samples, it is necessary to use a light source. The solar simulator used for all the tests is an Abet Technologies' model 11002 Sunline™ solar simulator. This solar simulator utilizes an optimized optical system to deliver an AM1.5 (100 mW/cm²) sun irradiance over an area of 50x50 mm, using a 100 W Xe arc lamp. In addition to a simple solar simulator, an electronic shutter is integrated, allowing an on-off light cycle on the illuminated area, at a controlled frequency and with a controlled shape of the wave. For what concerns this work, the shutter was set up to a frequency of 0.5 Hz, completing an entire on-off oscillation every 2 seconds. This resulted to be very useful

68

in order to determine the photocurrent generated by a sample, since the jumps between intervals of time with the sample illuminated and in dark conditions were immediately evident in the graphical representations of the results.
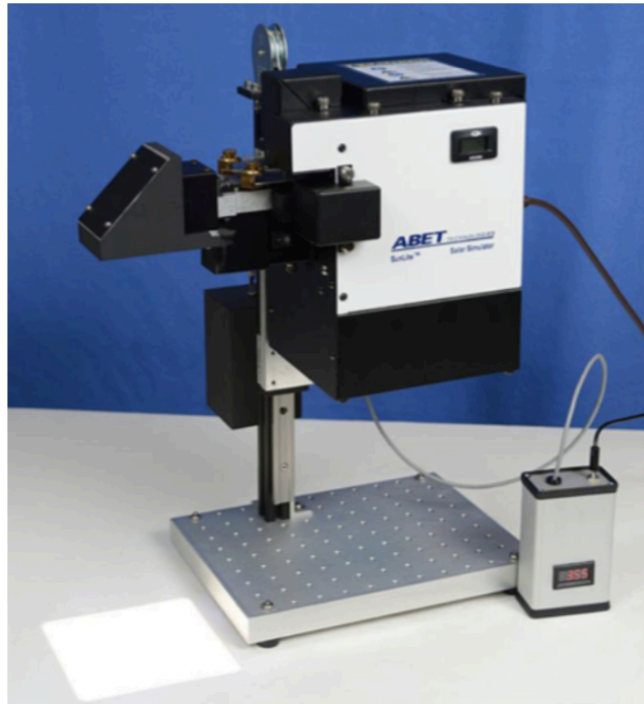
Figure 39. Solar simulator used for LSV tests.

Throughout the time employed for LSV tests, it was decided to produce two separated curves for each sample, one with the whole test under illumination conditions and one with dark conditions, so the shutter wasn't utilized anymore. This change allowed easier interpretation of the curves when superimposition of multiple tests' results was necessary for comparisons and evaluations.

Tests were carried out with photoelectrodes being kept at 21.5 cm from the lamp, where the light produced by the simulator has an irradiance equivalent to 1 sun.

3.2.2 Scanning Electron Microscopy

Scanning Electron Microscopy (SEM) is an imaging technique that allows to obtain representations of a surface at high magnifications, following the incidence of a collimated beam of electrons, called primary, on the surface of the sample to be

analyzed. In order to generate the beam, a tungsten filament is heated until its electrons are thermionically ejected due to the high energy they possess, and then directed towards the sample under analysis. Tungsten is the metallic material usually adopted for thermionic emission purposes, thanks to some of its peculiarities. It shows in fact a high melting temperature, a low vapor pressure, allowing to produce electron beams without interference of tungsten impurities detached from the filament, and it also has a reasonable cost. Other possibilities include lanthanum hexaboride. After generation of the beam, the charged particles are accelerated by an electronic cannon in an ultra-high vacuum (UHV) environment, with a pressure lower than 10^{-9} mbar, and directed to the sample exploiting a system of electromagnetic lenses, which is then used to move the beam over the sample's surface as well, allowing to obtain complete scans over areas of interest. The interaction of the collimated beam with the analyzed material can result in different phenomena, such as the scattering of the primary electrons (BS electrons), or the emission of either photons in the X-rays region or secondary e^-. Therefore, the electrons coming out of the sample's surface can be divided into backscattered (BS) and secondary, according to the energy they possess once they leave the material and reach the detector; while the former derive from an elastic scattering of the primary electrons striking atoms of the sample, the latter are the ones undergoing diffusion as a result of inelastic scattering occurring along their path when leaving the surface. *(57)*

Figure 40. SEM analysis instrumentation.

After collecting the incoming charges, the detector sends a signal proportional to the measured current density to a monitor. By synchronization of the displacement of the electron beam on the sample's surface with the position detected on the screen, it is possible to obtain a magnified image of the observed material. The analysis of the back-scattered electrons also allows to obtain a representation of the spatial distribution of the chemical elements composing the sample, considering the greater probability of the occurrence of elastic scattering for greater atomic number of the atoms involved.

As mentioned above, in some cases it is possible to observe the emission of X-rays or Auger (secondary) electrons, based on the energy possessed by the primary ones upon collision with the surface; it must in fact be high enough to tear core electrons from the atoms of the sample. Considering this, the same instrumentation utilized for SEM analysis can be employed also for compositional spectroscopy techniques, depending on the particular equipment at disposal. These are Energy Dispersive X-ray Spectroscopy (EDS) and Auger Electron Spectroscopy (AES). Moreover, considering the fact that scanning electron microscopy is a non-destructive analysis technique, since no surface modification is produced while moving the electron beam over the sample, it can be repeated for a desired number of times over the same specimen. *(57)* *(58)*

The instrumentation used for this work in particular consisted of a ZEISS EVO 50 EP, equipped with an OXFORD INCA ENERGY 200 EDS unit. Images produced via the use of SEM instrumentation were black and white representations with great resolution and depth of field, often allowing easy interpretation of what was present on the samples surface from a morphological point of view.

3.2.3 Atomic Force Microscopy

Atomic Force Microscopy (AFM) is a technique used in order to obtain information about the topography and roughness of a specimen's surface via its representation. Areas of investigation typically range from a range of 10x10 down to 3x3 μm^2, but

they can even be reduced down to the nm scale. For what concerns the lateral and the vertical resolution of the instruments, they're typically lower than 0.1 and 0.01 nm respectively. Moreover, AFM is one of the most important tools in order to manipulate matter at the nanoscale, thanks to its great degree of precision and maneuverability. *(59)*

Operations are based on the interaction between the surface of the sample under analysis and a scanning probe, consisting of a micrometric tip connected to a cantilever, which is typically made of silicon or silicon nitride. When the probe is in proximity of the surface, at a distance in the order of nanometers, Van der Waals interactions cause a deflection of the cantilever according to the Hooke's law. While scanning the surface, it is possible to reconstruct the topography of the sample by following the modifications these forces impose over the position of the cantilever with respect to its equilibrium configuration. The deflection of the cantilever is measured by means of a laser which strikes its back and is then reflected towards a photodetector that can analyze movements of the cantilever even in the order of 0.1 nm, relating them to the morphology of the surface. All the collected data are analyzed via software, allowing to process a topographic map of the sample. AFM analyses can be carried out in three different modes:

- in contact mode, the micrometric tip is placed at just a few ångströms from the sample, and then scanned over the surface. Measurement of the repulsive forces between the cantilever and the sample is based on a feedback system which registers the force that is necessary in order to keep the cantilever in contact position, i.e., at a fixed distance;

- in non-contact mode, the tip is instead kept at a fixed distance in the order of 10 nm, with attractive forces being developed between it and the surface atoms. Morphology of the surface is once again reconstructed by measuring the forces applied on the cantilever to keep it at the imposed distance;

- in tapping mode, the cantilever is instead placed in oscillation at a frequency similar to its resonant one, thanks to a piezoelectric system placed in the cantilever's structure. What's measured in this case is not a force anymore, but instead the amplitude of the cantilever's oscillations; in fact, while the instrument's input is kept constant, this amplitude is altered because of the

interactions of the tip with the sample's surface. The measurements take place once again through a feedback system, registering the input necessary in order to keep the oscillation amplitude at a constant level. All data are then processed via software to reconstruct the sample's surface topography. *(59) (60)*
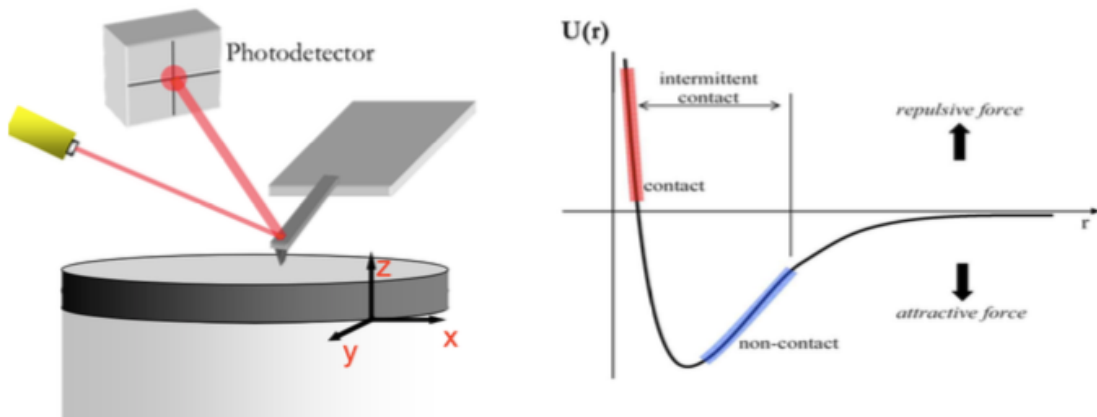
Figure 41. Left: schematics of AFM apparatus; right: potential energy variations vs sample-tip distance, with the three modes' range of action. **(60)**

For this work, measurements were taken in non-contact mode, with AFM SOLVER PRO produced by NT-MDT, mounting a silicon tip with an Au reflective layer, and having a force constant of 0.01-0.5 N/m.

3.2.4 X-Ray Diffraction

X-Ray Diffraction (XRD) is one of the most important non-destructive analysis techniques for what concerns crystalline materials. This is due to its ability to provide information about crystalline structure, different phases, crystal orientation, grain size, presence of defects and other structural parameters of the analyzed sample. The physical principles of XRD are based on the interaction between X-rays (having a wavelength in the order of interatomic distances) with the atoms of the crystal. When X-rays hit the surface, they're immediately elastically scattered in every direction, with the emission of secondary spherical waves originated from a specific electron of the atom that interacted with the incoming radiation. This X-rays diffraction produces

valuable information about the crystalline nature of samples, obtained by analysis of patterns resulting from constructive and destructive interference of the monochromatic radiation which is scattered by adjacent crystalline planes. In this process, the structure of the crystal under analysis offers a highly regular array of scattering centers, resulting in a likewise regular array of spherical waves being scattered. The disposition of the atoms (scattering centers) inside the crystal will therefore determine the interference phenomena associated to the secondary X-rays. By studying the position of interference peaks, it is then possible to reconstruct the whole crystallographic disposition of the atoms in the sample. *(61)*
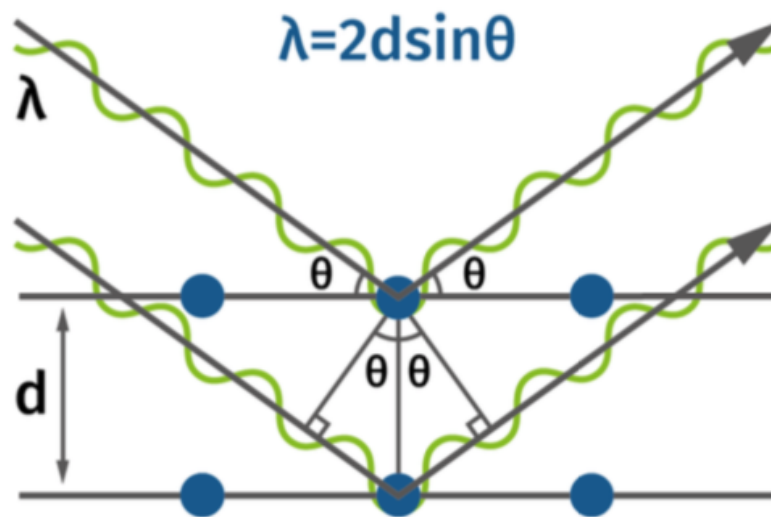
Figure 42. Illustration of two waves satisfying the Bragg's law. (stresstech.com)

There's a variety of ways in order to produce X-ray radiations, but the most used for this type of technique requires the use of a synchrotron light source. Radiation emitted from it is first of all filtered to make it monochromatic, and then directed towards the sample. According to Bragg's law, which is:

$$n\lambda = 2d \sin \vartheta$$

(where n is an integer number, λ is the wavelength of the incident radiation, d is the distance between consecutive atomic planes generating diffraction, and ϑ is the angle between the sample's surface and the incoming X-rays) a combination of λ, d and ϑ

can generate constructive interference for the scattered waves only if it satisfies the relation. This condition is graphically explained by figure 42. After diffraction takes place, a pattern is obtained on a 2D graph, with spots identifying regions for which wavelength of the radiation, diffraction angle and lattice parameters (distance between adjacent planes) satisfy Bragg's law, thus generating constructive interference. *(61)*
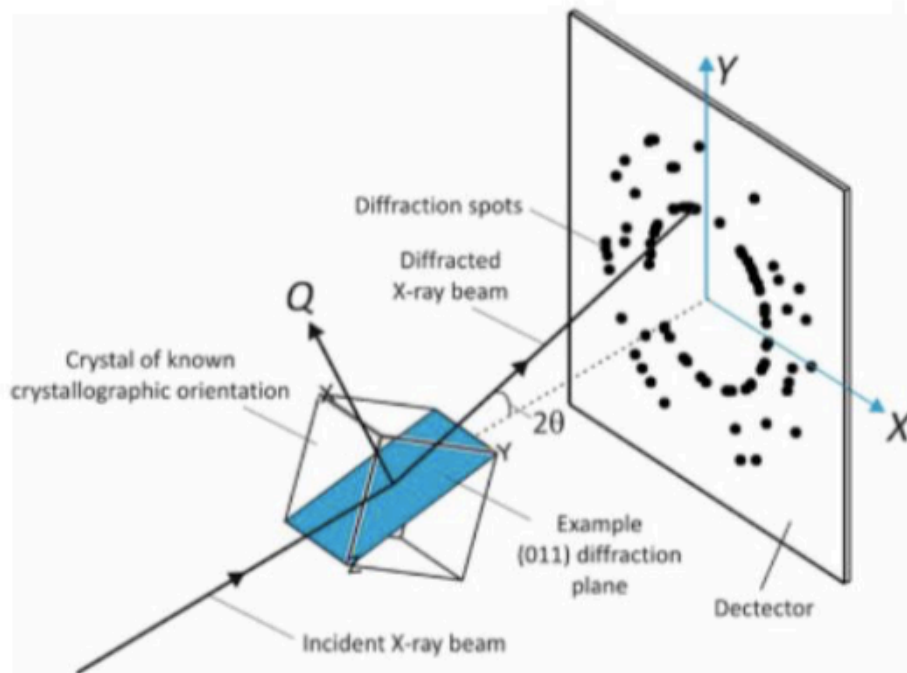
Figure 43. Representation of the process of detection of interference signals from a crystal. **(61)**

The positions of the spots registered on the 2D screen change in function of the locations of the atoms composing the crystal lattice. Therefore, by observing the pattern it is possible to understand the structure a material presents, together with the crystalline base. In other words, XRD allows to deduce all of the crystallographic properties of analyzed samples, provided that they are crystalline or semi-crystalline, otherwise there's no production of any interference pattern from the scattered radiation, since there's no regular disposition of atoms organized in planes. The graph with constructive interference pattern is transposed onto an intensity vs angle (2ϑ) plot for easier interpretation. In order to analyze all possible plane orientations, X-ray diffraction is usually performed on materials in the form of powders, in order to reproduce all of the possible diffraction directions for the particular material. When

instead it is not possible to perform the analysis over powders, the samples are inserted in the diffractometer and then kept spinning, exposing all of the possible plane directions to the incoming X-rays, thus producing all of the spots related to the material on the 2D detector plane. *(61)*

For this work, XRD measurements were obtained with a Malvern Panalytical EMPIREAN diffractometer. Tests were performed in thin film mode, using a Cu target to generate X-Rays.

4 EXPERIMENTAL RESULTS AND DISCUSSION

The experimental part of this work was focused on the production of $BiVO_4$ based photoanodes to be applied in photoelectrochemical water splitting, evaluating the current output produced at increasing potential by such electrodes by means of linear scan voltammetry, as described in the previous chapter, with particular attention to the value located at 0.6 V vs Ag/AgCl (equivalent to 1.23 V vs RHE), used as a benchmark for performance assessment in literature. Bismuth vanadate is one of the main materials studied for PEC photoanodes, but, as explained in section 2.5.1, some important limitations – mainly identified in poor water oxidation kinetics and charge transfer, and excessive occurrence of recombination events – hinder its diffusion at large scale in the field of hydrogen production, and need therefore to be addressed and limited in order to obtain a competitive water splitting technology. *(41)*

As already mentioned, it was chosen to deposit thin films of bismuth vanadate by means of different metalorganic decomposition methods. This choice was made for the great versatility, reduced costs and potential large-scale applicability of these techniques, but also for the numerous references present in literature. This work aimed at obtaining considerable values of photocurrent density outputs, and at the same time to do so with an easily replicable method of fabrication of the semiconducting materials of the photoanode.

Therefore, as for the major aspects considered during experimentation apart from the current output measured with LSV tests, reproducibility of the samples was considered as a very important aspect, since the long-term objective of this work would be the production of photoelectrodes at large scale. Thickness and morphology of the produced films were also kept under significant consideration, since they were held accountable for phenomena related to charge transport and recombination, and surface kinetics, respectively. It is in fact important to stress out the fact that carriers' diffusion length represents a critical aspect to consider if their recombination needs to be limited. This will be further discussed when examining the results obtained from LSV tests in comparison with SEM analyses, to address the correlation between microstructure of the deposited films with produced photocurrent.

For the reasons just explained, the above cited ones were the main elements influencing the orientation of this work's experimental phase. As a first step, photoanodes were produced with a drop casting method, and different routes were explored in order to limit the problems encountered, like the formation of rather inhomogeneous films on the FTO substrates. The introduction of a $BiVO_4$ seed layer by means of Sequential Ionic Layer Adsorption and Reaction (SILAR) represented the main progress concerning the drop casting production route, as sensible progresses observed during LSV tests were attributed to the seed's layer influence upon growth of the above-laying film at the microscopic level. In order to obtain advancements in term of produced photocurrent, SnO_2 produced via spin coating was investigated as a candidate material for the realization of heterostructures with $BiVO_4$. For this part of the work, the research revolved around optimization of thickness of the various layers and variation of the related production parameters. As for SnO_2 also bismuth vanadate films were produced via spin coating for this part of the study, because of the intrinsic uniformity of deposits fabricated via this method.

4.1 Drop casting $BiVO_4$

$BiVO_4$-based photoanodes produced via drop casting were the initial object of the experimental section of this work. After thoroughly cleaning the FTO substrates via sonication as described in chapter 3, a 1% Mo:$BiVO_4$ solution was deposited onto their surface in a quantity of 10 $\mu L/cm^2$, through the use of a micropipette. This quantity was chosen as a standard value by considering those utilized in the works taken as main references for this method of fabrication, being the studies of Kim et al. *(40)* and Pan et al. *(50)*. Despite being a slightly different value of dropped volume with respect to those proposed in the mentioned works, preliminary experimental results showed no appreciable variations between samples with 10, 12.5 or 15 $\mu L/cm^2$ dropped onto the FTO surface, so one of the decisive aspects taken under consideration to choose the appropriate quantity to deposit was the evaporation step, which was considerably faster with lower volumes, also helping to avoid formation of defects at this stage. Considering this, and in general to compare the photoelectrochemical behavior with

samples produced by dropping 10 μL/cm², also thin films with 5 μL/cm² were tested via LSV, but the obtained photocurrent at 600 mV vs Ag/AgCl was considerably lower than in the standard case, so the quantity of 10 μL/cm² was kept constant for all samples produced via drop casting.

In order to help homogeneity of the surfaces, it was decided to avoid moving the samples between drop casting and evaporation steps. Therefore, the actual deposition was performed with the samples already placed in the structure shown in figure 31 (section 3.1.1.2), which was then closed leaving a small aperture between the vessel and its cover, allowing creation of the appropriate gaseous atmosphere and pressure. Moreover, it was important to keep the FTO substrates as flat as possible during the deposition, to avoid migration of the low-viscosity solution caused by the action of gravity.

For the evaporation step, the reference works by Kim et al. *(40)* and Pan et al. *(50)* utilized an inert Ar atmosphere for a period of 15 minutes. For what concerns this work, a N_2 atmosphere with a low pressure inside the evaporation chamber was instead adopted as a standard for samples produced by dropping 10 μL/cm² of precursor solution, since it didn't produce particular variations with respect to the other inert gas. As for the time employed for this stage, visual inspection showed that 20 minutes were sufficient for the evaporation of solvents in the great majority of the cases, but anyway the samples were placed on a hot plate at 100 °C for a period of ~5 minutes to ensure optimal evaporation before the annealing treatment was performed.

As shown in figure 44, samples produced via drop casting presented irregularities on their surface, which were already present before the annealing treatment in tubular furnace. These were attributed to the possible formation of pressure gradients inside the evaporation chamber, causing turbulence which disturbed the homogeneity of the surfaces. In order to limit this occurrence, a filter was applied between the cap and the vessel of the chamber, and N_2 pressure was kept at a low level. These two expedients were adopted in order to try producing a homogeneous gaseous flux. Anyway, the obtained results were not acceptable in terms of uniformity of the thin films, and even if some samples were considerably better than others, reproducibility was considered as insufficient.
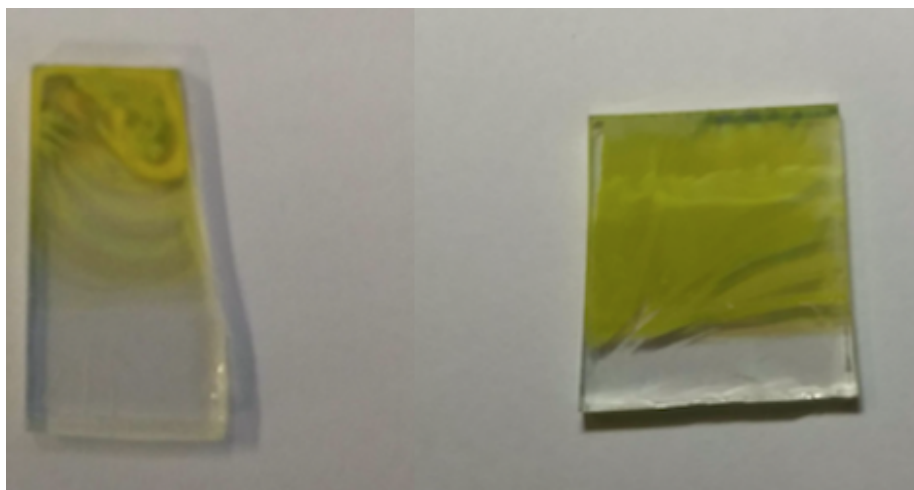
Figure 44. Classic examples of samples produced via drop casting, presenting defects which were originated during the evaporation step.

Since the above described detrimental effects were most certainly due to problems related to the evaporation stage, the annealing one was kept as described in literature, with a ramp of 10 °C/min to reach a temperature of 550 °C, that was kept for 25 minutes. For $BiVO_4$ photoanodes in general, this was considered as a standard thermal treatment to trigger recrystallization of the material into its photoelectrochemically favorable monoclinic scheelite structure, as described in the study by Rohloff et al. *(41)* mentioned in section 2.5.2, and this was verified by analysis of XRD spectra. Further confirmation of the fact that inhomogeneities in drop casting samples were originated from gaseous fluxes during evaporation came from the fact that, for $BiVO_4$ samples produced with other techniques, the annealing treatment didn't produce any undesired effect over the uniformity of deposited films (see section 4.2).

Characterization via SEM of the photoanodes produced via drop casting showed the usual flake-like crystalline domains of $BiVO_4$ produced via metalorganic decomposition techniques, as widely reported in numerous works. Figure 45 displays images of the surface at different magnifications, where the characteristic porous structure of bismuth vanadate films is evident, and the dimensions of the single flakes can be estimated to be lower than 1 μm in length.

As already mentioned, the film's porosity is of crucial importance, allowing better charge transfer from the surface of the photoanodic material to the electrolyte, since

the area of contact is much larger than it would be in the case of a more compact morphology.
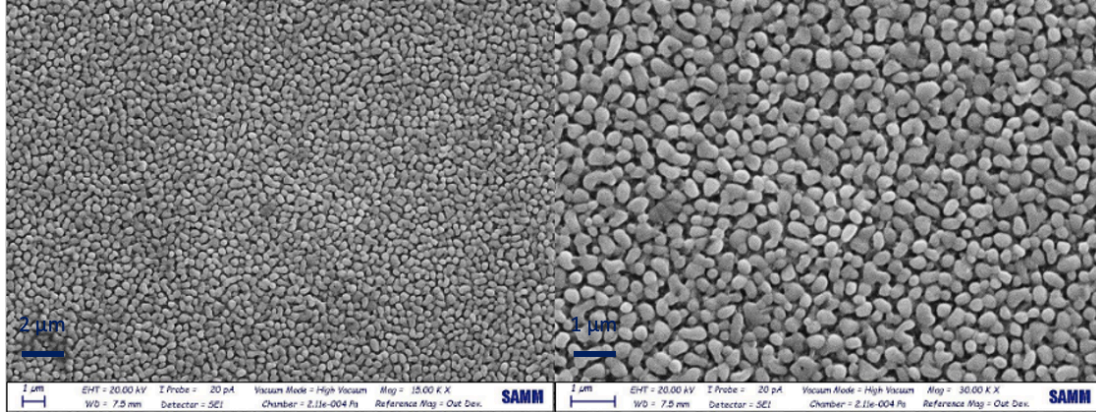
Figure 45. SEM images of drop casting BiVO₄ thin film, at 15Kx (left) and 30Kx magnification (right).

Atomic Force Microscopy analysis was also performed as an additional way to obtain visual information regarding the surface morphology of the samples. The resulting graph for a photoanode obtained by dropping 10 μL/cm^2 of solution onto FTO is represented in figure 46.
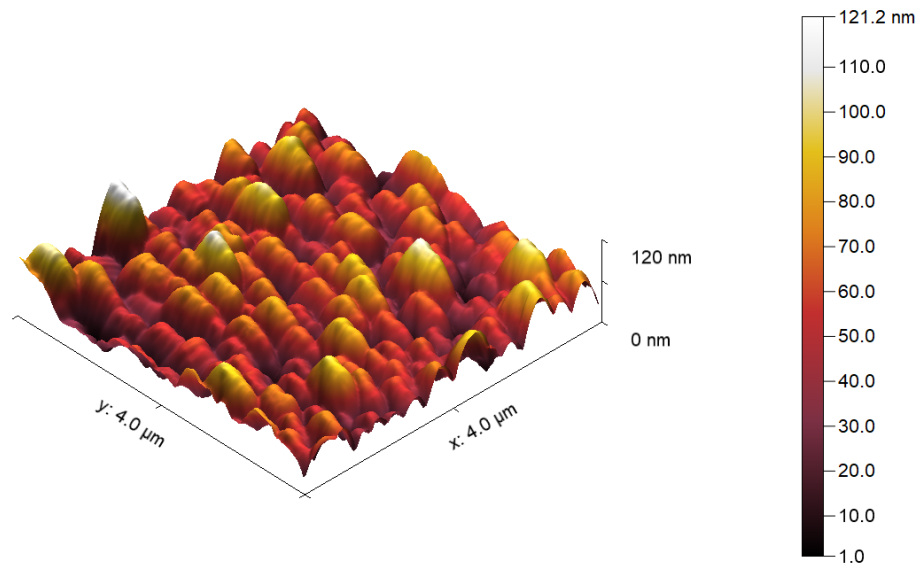
Figure 46. AFM image of a sample produced via drop casting with 10 μL/cm^2.

Data obtained by the instrumentation were analyzed via Gwyddion software, producing the above laying graph and allowing to obtain characteristic values for a

better understanding of some surface parameters, like the maximum height difference between peaks and valleys of the surface profile, in this case measured at 120 nm. This information, integrated by micrograph analysis of the morphology, can give an idea of the extent to which porosity is developed over the surface. Characteristics deduced by analysis of the AFM graph and of SEM images are coherent with one another.

Linear Scan Voltammetry curves were obtained for each of the produced samples to evaluate the photocurrent outputs at 0.6 V vs Ag/AgCl, applying the parameters described in section 3.2.1.1. Before performing the tests, each sample was visually inspected in order to identify a particularly uniform region over the whole surface, covering the rest of it with varnish in order to isolate only the chosen area. This step was considered necessary in order to evaluate photoelectrochemical performances in a correct way; since reproducibility of the films was one of the desired qualities, it wasn't logical to test one with important inhomogeneities across its extension. Attempting instead to produce higher degrees of uniformity was judged as a more rational choice. Because of this fact, the currents produced by the photoanodes were calibrated over the areas of their exposed active regions, measured via ImageJ software. The final photoelectrochemical performance was therefore evaluated in terms of density of photocurrent (j), expressed in mA/cm^2. This same procedure of applying varnish that isolated uniform regions of the produced films to prepare them for LSV testing was adopted for all of the $BiVO_4$ samples produced over the course of the experimentations. It is important to note that in this particular case of samples produced via drop casting, the remaining active regions that came in contact with the electrolyte during LSV tests were relatively small when compared to the ones obtained from other techniques, because of the problems discussed earlier. Nonetheless, current density was accurately evaluated over these regions, giving an idea of the potentialities of photoanodes produced with this technique in a PEC application.

Additionally, as it can be seen in figure 44, a small portion of the deposited film was etched from the FTO substrate, with the use of a low concentration HCl solution, which very easily dissolved the $BiVO_4$ deposited films. This step was necessary in order to guarantee the electrical contact of the photoanode connected to the potentiostat, allowing to impose a potential, and of course also to give an electrical connection between the working electrode and the Pt counter electrode.

In the produced LSV plots, current density acquired under AM1.5 illumination of the photoactive samples is expressed as a function of the potential (expressed in V vs Ag/AgCl RE) applied by the potentiostat to the working electrode. The photocurrent is evaluated as difference between the values produced in illuminated and dark conditions, as explained in chapter 3. Curves were therefore produced by utilizing the integrated shutter of the solar simulator, to make this difference immediately visible. Anyways, for the sake of easier interpretation of some of the graphs in which multiple samples are compared, some LSV tests were performed by measuring in two different steps, one under illumination and one with dark conditions for the whole duration. In these cases, the difference was then obtained by subtracting the corresponding values of the second curve from the first one.

The value of potential at which the analyses were started was the Open Circuit Voltage (OCV) of the photoanode connected to the Pt counter electrode, which is the immersion potential of the working electrode in equilibrium with the electrolyte solution. The scanning was then protracted up to the value of 0.7 V vs Ag/AgCl for the reasons already explained in chapter 3.
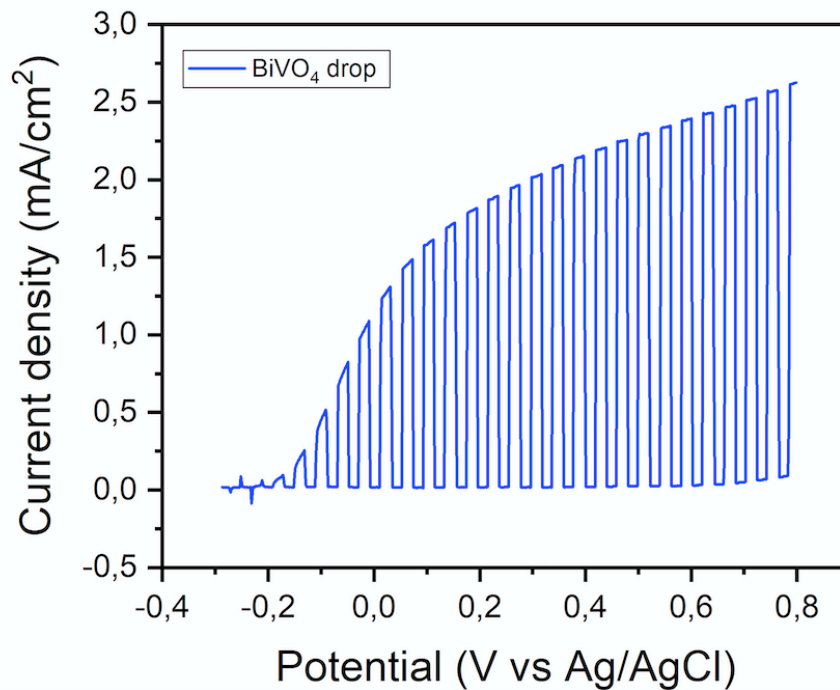
Figure 47. LSV resulting graph for a sample produced via drop casting with 10 µL/cm² of solution.

For what concerns BiVO$_4$ photoanodes produced with the above described technique, the best performances measured through LSV were comparable with the ones displayed in figure 47. As said, what is evaluated is the difference in the current density measured between time intervals during which the integrated shutter of the solar simulator blocks light (dark mode, graphically represented by the line following the lowest part of the graph) and those during which the sample is illuminated. As evident from the last figure, the best results obtained from drop casting gave a current density of about 2.3 mA/cm^2 at 0.6 V vs Ag/AgCl.

Apart from this value, fundamental in order to evaluate the photoelectrode's performances, there are other characteristics of the curve that are worth analyzing. First of all, it can be seen how the value of photocurrent doesn't immediately grow when the potential is increased from the starting value; there's in fact an interval of about 0.2 V of amplitude starting from the immersion potential for which current density stays very close to zero. Then, when the potential reaches a value around -0.15 V vs Ag/AgCl, current density starts to grow. The value at which the current density starts to grow is commonly referred to as the onset potential, since the activity of the material is observed from that point on.

Starting from there, it is possible to see how the value of the current grows with V for a certain interval. At a certain value, the slope of the curve decreases, and then the relation between current density and applied potential stays almost linear for the remaining part of the test. This kind of behavior of the curve, without any significant disturbances, indicates that the photoactive film is morphologically stable at these values of applied potentials; phenomena of photocorrosion are in fact negligible for situations like these. *(38)*

A proof of the effective presence of photoactivity in the material can be simply demonstrated by illuminating the sample while not imposing a potential; the value read by the instrumentation registers a shift towards more negative values (from ca. -50 mV to -300 mV) when light hits its surface. This behavior is caused by the generation of electron-hole pairs inside the deposited film.

From a qualitative standpoint, the above described features can be observed for all of the LSV curves analyzed throughout the course of this work, mostly because they all

depend on the fact that the material under analysis is photoactive, and therefore the appreciable differences between distinct curves are mostly of quantitative nature.

By looking at the graph represented in figure 48, it is instead possible to observe an important difference for what concerns the value of current density measured at 600 mV vs Ag/AgCl, and in general for the behavior of the curve, between the case of front and back illumination of a sample, which in this case is the same whose behavior is represented in the previous graph.
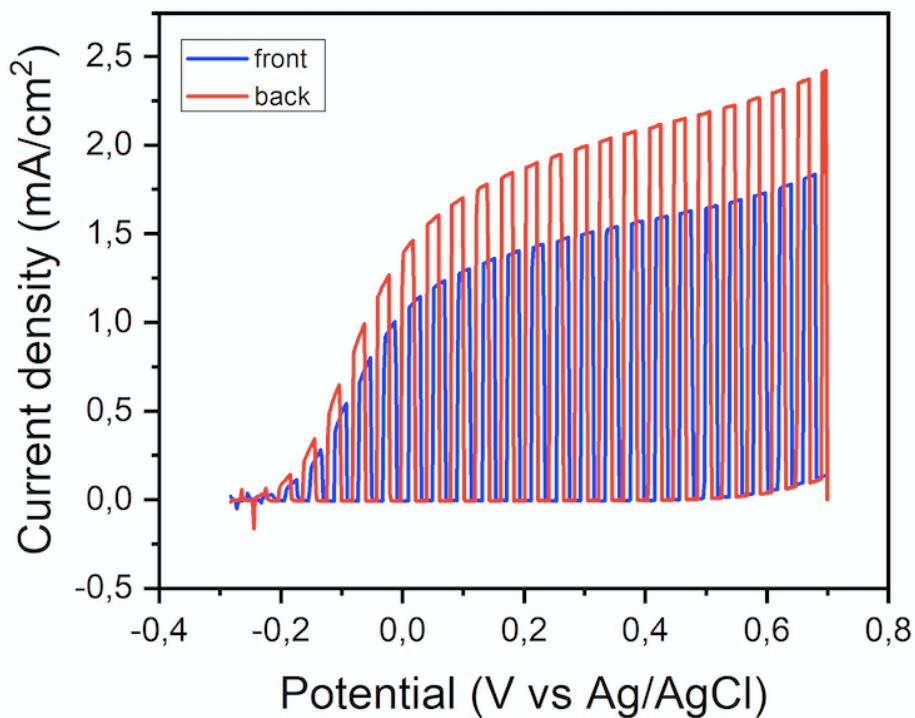
Figure 48. LSV graph for the same sample in front (blue) vs back (red) illumination conditions.

As anticipated in section 3.2.1.1, while there are no significant differences for what concerns the overall shape of the two curves, the photoelectrochemical efficiency measured in conditions of back illumination is greater than in the case of front illumination. This indicates that electron transport through the thickness of the deposit to reach the electrical back contact is one of the main causes of recombination, as described in the works of Liang et al. *(45)* and Wang et al. *(62)*; in fact, electrons have to cover a longer path when the radiation strikes the photoanode at the electrode-electrolyte junction, since the EHP is generated farther from the FTO surface, and vice

versa the same is true for holes in back illumination to reach the junction and give water oxidation. A situation in which electrons have to cover the shortest possible path is then preferable to obtain higher photoelectrochemical efficiency of bismuth vanadate photoanodes.

The experimental observations are consistent with the electronic band structure of $BiVO_4$ in its monoclinic scheelite structure as it is described in literature; in fact, in this case the conduction band consists mainly of the 3d band of V (as depicted in figure 26), and because of the fact that in this configuration the VO_4 tetrahedral units do not share edges or corners, electrons have to hop from one tetrahedron to another in order to move through the $BiVO_4$ film. Doping with small amounts of molybdenum only introduces a small distortion in the original lattice, therefore this phenomenon remains a feature of the material. *(45)*

For the particular case of the specimen of figures 47 and 48, the current density at 600 mV vs Ag/AgCl shifts from a value of 1.75 mA/cm² in front illumination to 2.3 mA/cm² in back, with an important variation of 0.55 mA/cm², roughly 30% of the value in front illumination. While this difference is an intrinsic aspect of all $BiVO_4$ and $Mo:BiVO_4$ photoanodes, being that it derives from the crystalline structure of the material itself, it is reported in literature that larger differences are observed in the case of undoped films, meaning that the slight distortion introduced with Mo doping can enhance charge transport of electrons. *(42)*

In any case, the differences between curves obtained in front and back illumination were more or less prominent when analyzing different photoanodes, indicating a dependence not only on the intrinsic nature of $BiVO_4$, but on the different results obtained from fabrication of the samples. The same type of variation for photoanodes produced with different techniques will be taken into account later on, showing quantitatively or qualitatively different behaviors in comparison with the case that was presented in figure 48.

From the analysis of an XRD spectrum for a $Mo:BiVO_4$ sample produced via drop casting, illustrated in figure 49, it is possible to notice how the disposition and intensity of the peaks indicate that the crystalline structure of the photoanodic material coincides with the one of bismuth vanadate in its monoclinic scheelite structure. X-ray diffraction was performed over the same areas that were selected for LSV testing, in

order to ensure that the structure of the material was indeed the desired one. Peaks in the figure aren't generated only by the deposited material, but from the underlying substrate as well, which is made of fluorine-doped tin oxide in its cassiterite crystalline form.
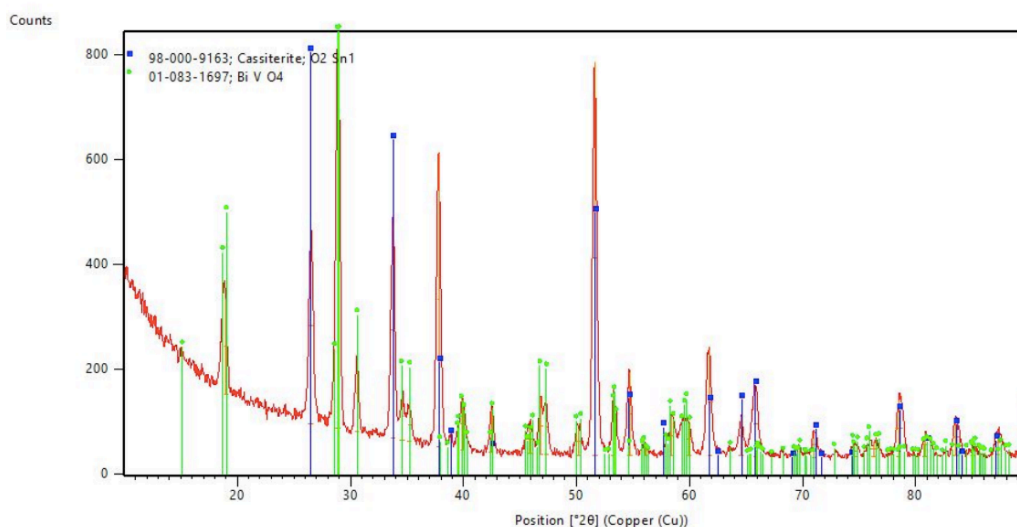
Figure 49. XRD spectrum of a Mo:BiVO$_4$ photoanode produced via drop casting, with 10 µL/cm^2 of solution deposited on a FTO substrate.

In the graph, the red continuous line represents the signal registered by the instrument, while the relevant peaks are highlighted with a blue marker if they correspond to the FTO substrate, or with a green one in the case of bismuth vanadate. Regarding relative intensities of the peaks corresponding to the produced BiVO$_4$ film and to the FTO substrate, they generally vary with the amount of material that is effectively deposited onto the surface. Therefore, while position of the peaks remains the same (since it only depends on the crystallographic planes of a particular structure), their intensity can vary for two photoanodes produced with different methodologies.

What is immediately evident is that doping with molybdenum produces a crystalline structure that is just lightly distorted with respect to that of pristine BiVO$_4$, as hinted by the relatively wide characteristic peaks; this is coherent with the study of Park et al. *(36)*, in which it is reported that Mo^{6+} ions substitute V^{5+} ones with doping, and the slight distortion is originated by the small difference it the two ionic radii, which is just of roughly 0.005 nm. The XRD spectrum presents therefore all of the expected

87

peaks for $BiVO_4$ in its monoclinic scheelite structure: the highest one is the peak located at an angle of 28.9°, which corresponds to the (121) family of crystalline planes. The second most predominant bismuth vanadate peak is instead located at roughly 19°, resulting from the two different peaks at slightly higher and lower angles that are clearly visible in the graph; these correspond to the families of planes of Miller indexes (110) and (001). The last peak that is important in terms of relative intensity is finally detected for an angle of 30.6°, indicating the family of planes (040). These peaks correspond then to the directions of preferential growth in this case. *(63)*

It can be noticed how there is not a clear predominance of one of the growth directions over the others, and this is a sign of how the nanostructures in the deposited film are randomly oriented, causing slight variations of the relative intensities of XRD peaks between different spectra of the same type of crystal structure.

By comparing the values of the highlighted angles with the ones indicated for XRD analysis of $BiVO_4$ in the Joint Committee on Powder Diffraction Standards (JCPDS) *(63)*, presence of the photoelectrochemically favorable monoclinic scheelite crystal structure was finally confirmed, indicating a correct application of the thermal treatment in the tubular furnace.

The complete transition to a monoclinic scheelite structure is of fundamental importance for the functioning of the photoanode, because a tetragonal structure would imply a very different behavior for what concerns generation of electron-hole pairs, having an electronic band gap of 2.9 eV, much larger than the 2.4 eV of the monoclinic case (as shown in figure 26, section 2.5.1). Moreover, interfacial regions between a monoclinic and a tetragonal phase could be detrimental, acting as recombination centers and ultimately reducing the number of charged species useful for the functionality of the photoelectrode. Potential presence of a tetragonal phase in the deposited film is detected in the eventuality that strong peaks are registered for angles of 24.4° and 32.7°, typical values for tetragonal $BiVO_4$, which are not detected in this case.

By looking just at the current values that drop casting samples were able to produce at 0.6 V vs Ag/AgCl and in general to the quality of the registered LSV plots, photoelectrochemical efficiency can be considered overall good when compared to other values found in literature. As mentioned before, the biggest problem regarding

this methodology of photoanodes fabrication was related to the absence of homogeneity of the deposit's surface, originated during the solvent's evaporation stage, just before annealing. These irregularities were easy to observe at a macroscopic scale from sample to sample and were pretty much inevitable in a type of synthesis carried out by a human operator. For what concerns the evaporation chamber setup, different configurations were attempted during the production, the most efficient of them being the one represented in figure 31 (materials and methods section).

In the case of drop casting, differences in uniformity of the surfaces indicated that the deposit's morphology was highly dependent on experimental conditions over which it is was very difficult to have a fine degree of control, and this cannot of course be accepted if one of the main objectives of the work is to obtain an easily reproducible way of fabrication. In addition, it can be assumed that a photoanode with a considerably larger area than the ones tested (measuring 1.8 x 2 cm^2) would present even bigger inhomogeneities across its surface.

It must be said that these problems regarding uniformity are not an intrinsic characteristic of this technique, but rather of instrumental limits observed throughout this work. The initial idea was in fact to exploit metalorganic decomposition methods also for their potential large-scale applicability.

4.1.1 Introduction of a seed layer via SILAR

Based on the overall results obtained via drop casting method, it was decided to try finding a way to produce a higher degree of uniformity among surfaces of the produced photoanodes. In order to achieve this result, Sequential Ionic Layer Adsorption and Reaction (SILAR) was evaluated as a valid alternative to improve the deposited materials in terms of homogeneity at the microscopic scale. Therefore, a very thin layer of material was deposited on the cleaned FTO substrate via SILAR.

This methodology was judged as a viable technique based on the study performed by Odling et al. *(52)*, taken as the main reference for this kind of production. According to the mentioned work, deposition of BiVO$_4$ via SILAR on a metal oxide substrate like FTO is able to produce a monoclinic scheelite structure upon thermal post treatment,

which for what concerns this work consisted in an annealing on a hot plate at a temperature of 550 °C for 20 minutes, performed immediately after the last rinsing stage of the procedure. The monoclinic scheelite structure can be identified from the XRD graph peak corresponding to the (121) family of planes, even if the signal is relatively low, since the quantity of deposited material is very limited with respect to a technique like drop casting. *(52)*

One of the major advantages of the SILAR method consists in the possibility to finely tune the thickness of the produced film, being that, as explained thoroughly in chapter 3, one deposition and rinsing cycle theoretically deposits one monolayer of the desired material. To make this possible, dipping and rinsing time frames must be defined in relation to the concentration of cations and anions in the two solutions, guaranteeing efficient coverage for each of the adsorbed monolayers.

After a preliminary study, it was decided to keep the concentrations of the two ionic precursors at 10 mM, with a dipping time of 30 s. As for the formulation of the solution for the bismuth precursor, instead of using water as the solvent like Odling et al. *(52)* did, 2-methoxyethanol was instead utilized (Haji Yassin et al. *(64)*), as it produced a much more uniform mixture, ensuring that position of the FTO substrate suspended inside the bath wasn't influencing the quality of the deposit.
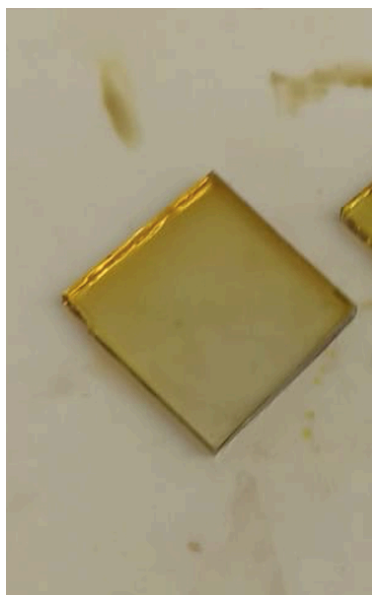
Figure 50. Sample with BiVO₄ seed layer deposited via 5 SILAR cycles over FTO, portrayed after annealing treatment.

Considering these concentrations of the solutions and adsorption time frames, at first different numbers of deposition cycles were tested, but in the end, it was decided to perform 5 complete SILAR cycles to produce the $BiVO_4$ seed layer. By observing the sample in figure 50, it is possible to notice how the procedure originated a slight shift of color from a transparent FTO glass towards the characteristic yellowish shade of bismuth vanadate.

It is important to note that, contrary to the drop casting layer that was intended to be deposited above, the one produced via SILAR consisted of pristine, undoped $BiVO_4$. Nonetheless, as already explained, the crystalline configurations of the two materials are so similar that the variations could not induce formation of undesired modifications along the interface. The seed layer was in fact introduced as a way to positively influence the formation of the above laying deposit by influencing the microstructure at the interface. Moreover, since the major uniformity defects observed from drop casting were originated during the initial drying phase, one of the desired effects of the SILAR fabrication was a positive influence over the wettability of the surface with respect to the case of bare FTO. It was in fact very difficult to obtain a regular distribution of the deposited solution, as described in the previous section.

After the annealing treatment on a hot plate was performed on the seed layer as described, samples were ready for the deposition via drop casting of Mo doped $BiVO_4$; the quantity of precursor solution dropped onto the substrate was again of 10 μL/cm², since this was kept as a standard in order to evaluate the influence of the underlying layer, keeping all of the other process parameters as they were defined during the first stage of drop casting production. Deposition was again performed in the same enclosure where the evaporation phase took place, and everything was kept as it was done for Mo:$BiVO_4$ drop casting on bare FTO, including the annealing stage in the tubular furnace.

As immediately noticeable by looking at figure 51, also in this case the evaporation phase produced macroscopic defects in terms of uniformity of the deposit, which were attributed to the same phenomena individuated in section 4.1.

Figure 51. Evaporation defects present on the surface of a photoanode prepared via drop casting of 10 µL/cm² of Mo:BiVO₄ solution over a BiVO₄ seed layer.

Looking at the photoanode depicted above in particular, different shades of yellow are observable along the surface, indicating a different thickness of the deposit in the corresponding area. This caused of course some problems in the decision of areas to test, since the thickness of the photoactive material is one of the most important aspects influencing the overall photoelectrochemical efficiency.

Considering this fact, active areas that were effectively tested during LSV tests (so left exposed, without application of varnish) were again very small with respect to the 1.8 x 2 cm² of the whole FTO glass, compromising the applicability of this fabrication method for the production of high-surface photoanodes. Non controllable, small experimental variations produced specimens presenting very different deposits.

As a way to investigate morphology of the tested photoanodes, SEM data were obtained for selected areas, producing images comparable with those represented in figure 52. Comparing these images with those in figure 45, the flake like crystalline domains of bismuth vanadate produced via metalorganic decomposition methods are again easily identifiable on the surface, together with the usual porous structure of BiVO₄ films produced via MOD methods.
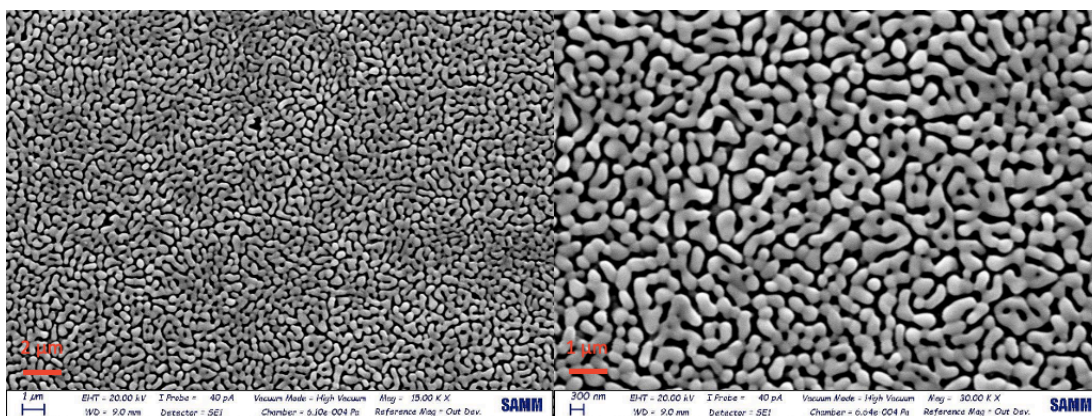
Figure 52. SEM images of a photoanode produced via SILAR (5 cycles) followed by drop casting (10 µL/cm²) at 15Kx (left) and 30Kx magnification (right).

For what concerns instead the characteristic feature dimensions, it can be seen how in this case the nanostructures presented more elongated shapes with respect to the ones from drop casting on bare FTO, together with more pronounced interconnections between different flakes. Altogether, it can be said that, for what concerns uniform areas tested via LSV, the changes introduced by the seed layer from a morphological point of view were present, but not massive. Therefore, a pretty much equal ability of the material can be expected when evaluating the charge transfer ability from the anode to the electrolyte solution.
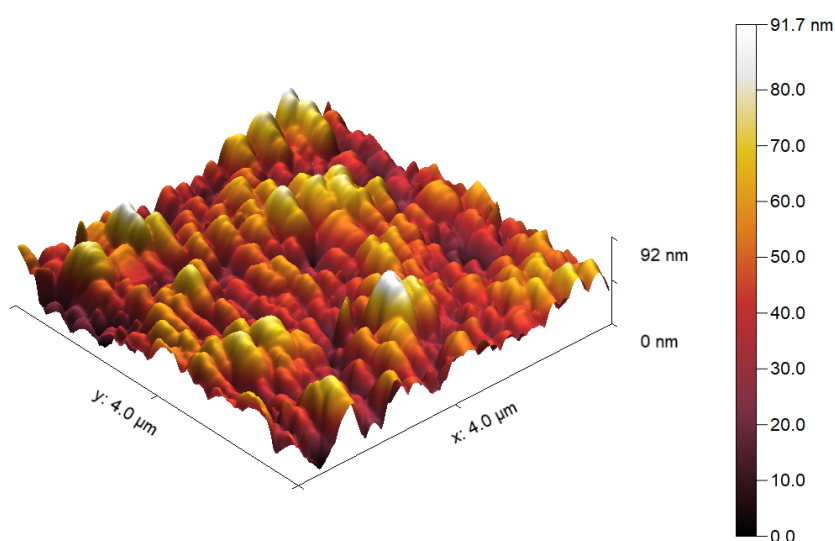
Figure 53. 3D graph resulting from AFM analysis of a photoanode produced via drop casting of the Mo:BiVO₄ solution (10 µL/cm²) over a seed layer produced via SILAR (5 cycles).

Further analysis of the superficial morphology was obtained via AFM measurements, allowing to produce the graph represented in figure 53 via Gwyddion software. Characteristics obtainable from AFM and SEM analysis are coherent with each other, and, as expected, they're also very similar to the ones individuated for the case of drop casting on bare FTO. In the case of SILAR followed by drop casting, the maximum height difference measured between different regions of the scanned surface was of 92 nm, a pretty similar value to the 120 nm that were obtained without application of the seed layer, showing once again a substantial affinity between the morphologies in the two situations.

X-ray diffraction was utilized to assess crystallographic properties of the samples, producing the graph depicted in figure 54.
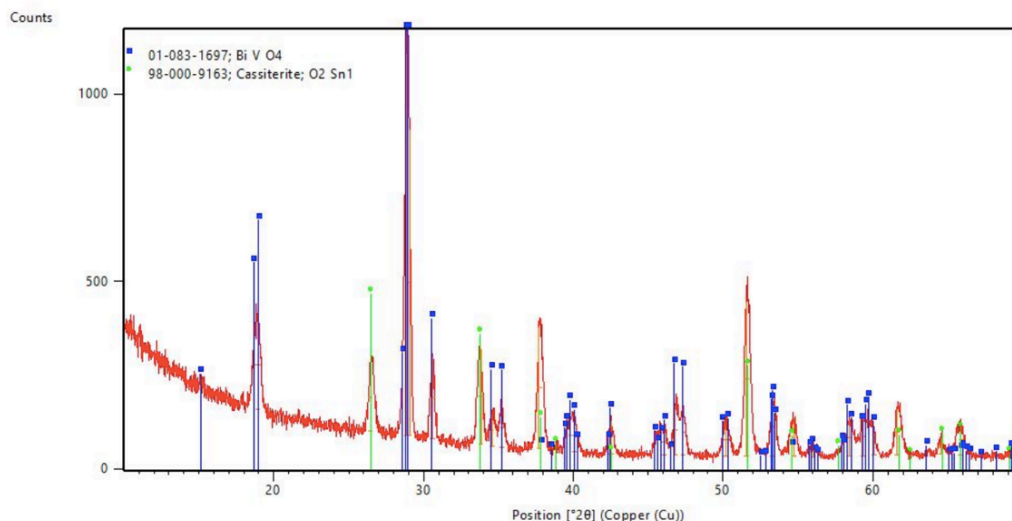
Figure 54. XRD spectrum of a photoanode produced via drop casting of Mo:BiVO$_4$ (10 µL/cm^2) over a seed layer fabricated via SILAR (5 cycles).

In this case, peaks associated with cassiterite are marked with green circles, while those corresponding to the crystal structure of BiVO$_4$ are matched by blue squares.

Also for this type of analysis, the expected correspondence with the case of drop casting on bare FTO was found. The same three predominant peaks highlighted in figure 49 are present also in figure 54: the most intense one at an angle of 28.9°, corresponding to the family of planes (121), the second in order of relative importance

at 19°, for the (110) and (001) families, and the third located at 30.6°, generated by diffraction from the (040) planes. The two spectra are indeed almost identical when put close to each other, mostly because of the application of the identical thermal treatment in the tubular furnace. It is finally worth mentioning how the peaks at 24.4° and 32.7° are absent for this type of photoanodes as well, indicating absence of the crystal planes generating diffraction in a tetragonal $BiVO_4$.

The curve depicted in figure 55 represents the best results in terms of photoelectrochemical performance for photoelectrodes produced with the SILAR seed + drop casting method.
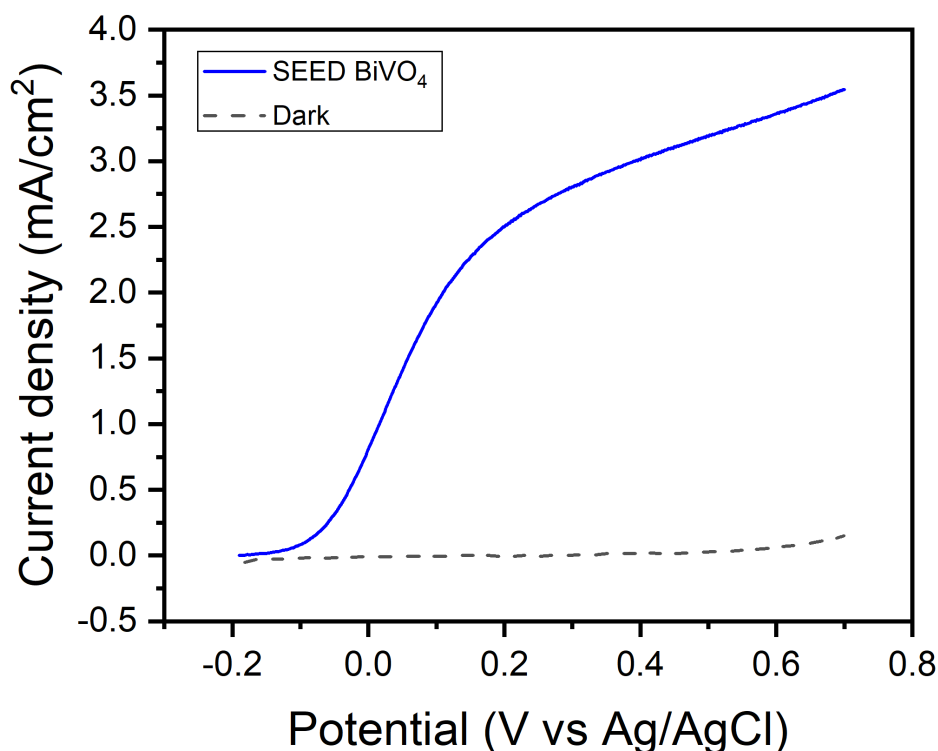
Figure 55. LSV results for a photoanode produced by drop casting (10 µL/cm²) of Mo:BiVO₄ over the seed layer precedently deposited via SILAR (5 cycles).

The value of current output registered at 0.6 V vs Ag/AgCl is of 3.3 mA/cm², while the onset potential is shifted to about -0.08 V vs Ag/AgCl, a more positive value than in the previous case. Significant values obtained for photoanodes produced via drop

casting over bare FTO and over seed layer are summarized in table 1 for easier interpretation.

Method of fabrication	Immersion potential [V vs Ag/AgCl]	Onset potential [V vs Ag/AgCl]	Current density at 0.6 V vs Ag/AgCl
Drop casting	-0.25	-0.15	2.3 mA/cm^2
SILAR + drop casting	-0.2	-0.08	3.3 mA/cm^2

Table 1. Comparison between significant values obtained for drop casting over bare FTO vs drop casting over a seed layer.

The most important aspect that is immediately observable is a great positive shift for the current density output measured at 0.6 V vs Ag/AgCl, proving an appreciable improvement for what concerns photoelectrochemical performances when applying a seed layer before fabrication of the drop casting deposit. In particular, the current density value improved by a remarkable 43% (1 mA/cm^2) with respect to the value obtained without seed. This significant variation was attributed to the configuration provided at the interface with FTO that was generated through SILAR, with a high degree of order at the microscopic scale, and at the same time to the influence of the seed layer upon the above deposited $BiVO_4$ growth.

For what concerns the shape of the two curves, directly compared in figure 56 for easier interpretation, it can be noticed how they present similar behaviors, with differences observed only from a quantitative standpoint; application of the $BiVO_4$ seed caused a slight shift of less than 0.1 V towards more positive potential values in regard to the immersion potential. This difference is kept almost at the same level even after the onset potential, up to a point where to gap starts decreasing. A little bit after the 0 V vs Ag/AgCl mark, the curve obtained by the deposit over the seed layer leaps over the other one, thanks to its more pronounced positive slope after the onset potential. The length of the interval for which the initial slope is kept before eventually decreasing is instead almost the same for both methodologies of fabrication, giving the different value registered at 0.6 V on the horizontal axis. Overall, the influence of the seed layer can be appreciated by looking at the much larger area of the graph that lies below the corresponding curve.
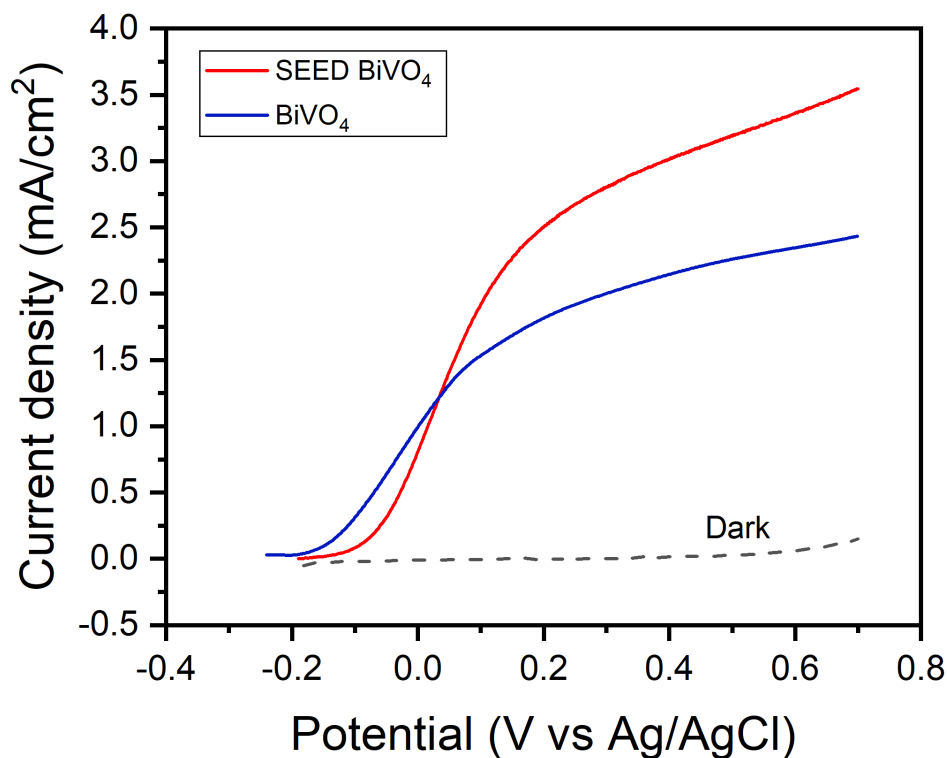
Figure 56. Comparison between the LSV measurements obtained by photoanodes produced by drop casting over bare FTO (blue) and over a seed layer deposited via SILAR (red). The same quantity of Mo:BiVO₄ was dropped in both cases.

The current density registered at 0.6 V vs Ag/AgCl for the drop casting on bare FTO was already considered a promising value when compared to those found in literature, and the modification introduced by the seed layer was very significant, producing an improvement without changing the overall appreciable features of the previous curve. Other than that, the problem regarding uniformity of the deposits wasn't solved at all. Therefore, a drop casting process of this kind was judged as a non-viable technique because of the inability to produce highly homogeneous photoanodes with relatively large areas, even if other attempts at improving this aspect were made later on. Taking into consideration these important limitations, it was decided to shift the focus of this work towards a different metalorganic decomposition method more suitable for production of uniform films, and for which dependence from experimental variables is more controllable in terms of reproducibility.

4.2 Spin coating $BiVO_4$

Spin coating was introduced as a way to obtain a high degree of uniformity of films deposited over the FTO substrates, as it was reported in literature as an efficient method to obtain this feature. Such a characteristic comes from the very nature of a spin coating process, for which the fabrication procedure is predominantly automated in relation to a drop casting one, where a human operator has a much higher influence over the final result. Moreover, the solvent evaporation step, which was considered the main source of inhomogeneities in the previous section, didn't produce significant undesired effects in this case, since it didn't involve application of a gaseous flux, but instead just placing the samples on a hot plate at 400 °C for a period of 5 minutes before performing the annealing treatment in tubular furnace with the same parameters adopted for drop casting specimens, as described in section 3.1.1.1.

By looking at the formulation of the solutions utilized for this methodology of production, described in the chapter relative to materials and methods, it can be seen how concentrations of the bismuth and vanadate ions in the precursor solutions were doubled with respect to the ones employed for drop casting, while maintaining a 1.1 ratio between Bi and V moles and a 1% number of Mo moles with respect to those of vanadium. This modification was considered necessary in order to deposit quantities of material comparable to those produced via drop casting, as spin coating films are generally thinner with respect to those fabricated via other MOD techniques.

Different studies regarding this topic, and in particular the ones provided by Byun et al. *(46)* and Sayama et al. *(65)* reported enhanced photoelectrochemical performances of spin coating $BiVO_4$ photoanodes presenting multiple layers deposited on top of each other, with different rpm values and spinning time intervals. This is to attribute to the fact that spin coating can deposit only very thin layers, since the rotational speed must be kept at a consistent level for the sake of thickness uniformity. In particular, the study of Sayama et al. *(65)* reported a thickness lower than 0.1 μm per layer at 1000 rpm.

For what concerns this work, photoanodes produced via spin coating had thicknesses comparable to the drop casting ones only for a number of deposited layers around 5. The difference in color that is observable from direct comparison of the sample

depicted in figure 57 (spin coating) with the ones in figure 44, can be instead attributed to a more compact morphology of the film, as it will be discussed later. This produced a slightly more translucent aspect.
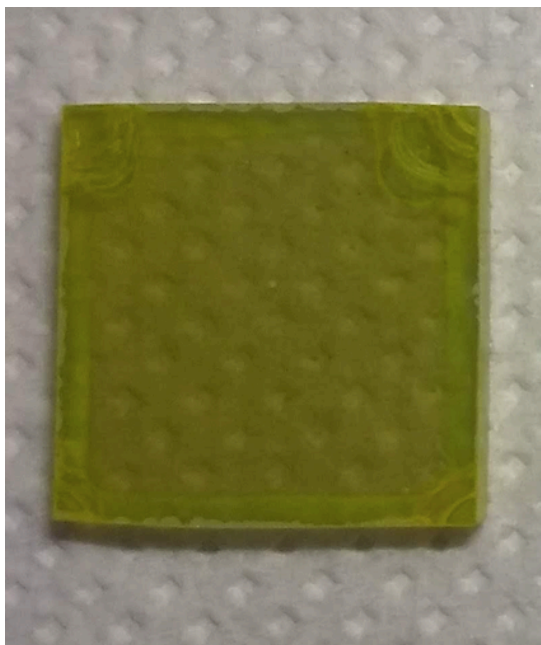
Figure 57. Photoanode produced by spin coating of Mo doped BiVO₄ (5 layers), presenting the characteristic translucence of samples produced with this technique.

Preliminary deposition tests, performed by stacking 5 layers on top of each other, allowed to optimize the spin coating process parameters by applying a rotation of the plate at 1000 rpm for 25 seconds, taking the values reported in literature as a starting point. In particular, the spinning time frame was kept from the reference works, as visual inspection carried out immediately after the spinning process was completed didn't pinpoint any significant variations in terms of thickness above the FTO substrates, while the rpm value was chosen by evaluating the LSV curves of produced photoanodes.

As explained in chapter 3, samples were placed on a heating plate at a temperature of 400 °C for 5 minutes between application of consecutive layers, to ensure correct solvent evaporation and trigger initial recrystallization of the material into its monoclinic scheelite form. Experimental evidence demonstrated that it wasn't in fact necessary to apply thermal annealing in the tubular furnace after every layer to obtain the desired structure, reducing by a lot the time taken for the synthesis of photoanodes.

The annealing stage at 550 °C for 25 minutes and with a heating ramp of 10 °C/min was applied only after the last layer of BiVO$_4$ was deposited.

At first, the experimental part dedicated to spin coating revolved around the individuation of the optimal thickness to get the highest possible current density output at 0.6 V vs Ag/AgCl, which corresponded to a certain number of layers spun above the FTO substrate. In addition to the analysis of the obtained LSV plots to assess photoelectrochemical efficiency, morphological and crystallographic parameters were taken into account via SEM, AFM and XRD measurements, evaluating the results relatively to those obtained for drop casting.

Inspection of SEM images, illustrated in figure 58, reveals a visually homogeneous morphology of the analyzed surface, where it's still possible to notice the characteristic flake-like structure of the BiVO$_4$, with some differences with respect to the structure observed for drop casting samples (refer to figure 52); the deposit looks in fact much more compact, with a lower degree of porosity. This is a common trait of all films produced via spin coating, which are in general more packed and uniform over large areas.
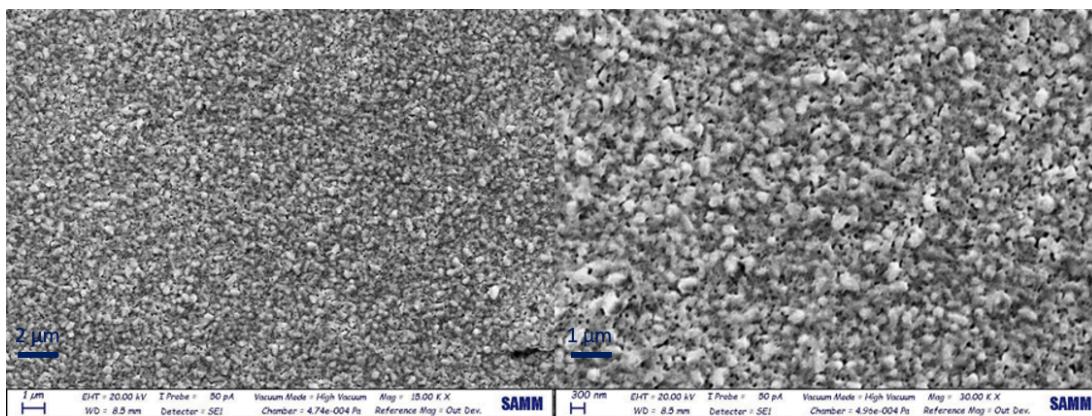
Figure 58. SEM imagies of a BiVO$_4$ photoanode produced via spn coating with deposition of 3 layers at 15Kx magnification (left) and 30Kx magnification (right).

The reduction of porosity results however in a much reduced contact area between the semiconducting material and the electrolyte, which is expected to negatively influence the overall photoelectrochemical performance of the material because of the less efficient charge transfer to the electrolyte.

Considerations derived from SEM images are corroborated by those made possible by AFM analysis, where a more compact surface is shown with respect to the case of drop casting, influencing porosity as just explained.
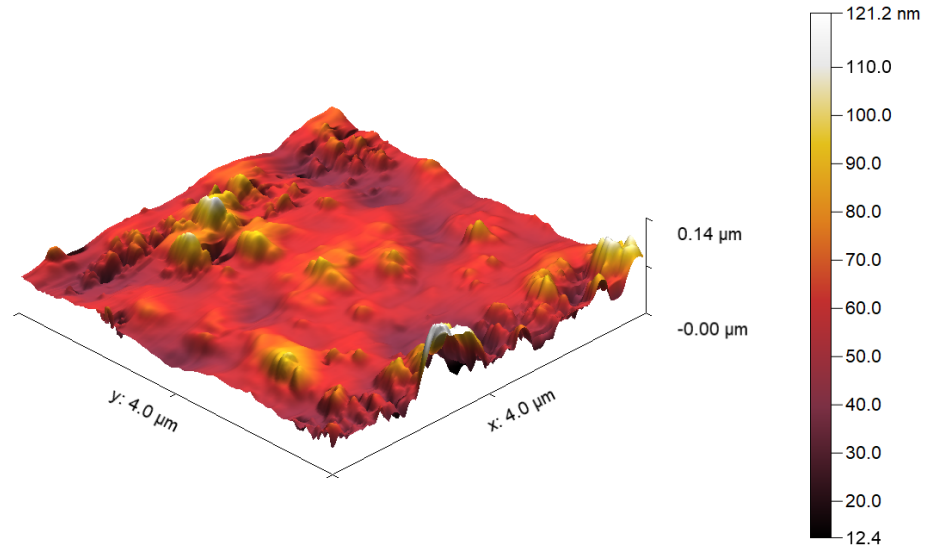
Figure 59. Graph resulting from AFM analysis performed over a BiVO$_4$ deposit produced via spin coating method.

In comparison to AFM graphs produced for drop casting samples, in the case of figure 59 the surface seems to present a much smoother morphology. In reality, it must be taken into account that AFM measurements were taken in non-contact mode. Considering that characteristic features of the surface presented very reduced typical dimensions, the 3D image of figure 59 cannot accurately represent the actual surface depicted in the SEM picture. It must be instead interpreted as an indication about the difference in height between "peaks" and "valleys" that will be located at the semiconductor-electrolyte junction, giving an idea of the extension of the contact area while the photoanode is in working conditions.

In addition, the maximum difference between lowest and highest points measured along the analyzed area, equal to 121 nm, in this case is caused by the small irregularities found along the right edge of the graph, but for example the mean roughness registered a value of 8.8 nm, roughly half than the one measured in both the cases relative to drop casting photoanodes.

It is important to point out the fact that bismuth vanadate films synthetized via spin coating presented substantial uniformity of the deposit along the whole area of the FTO substrate. As it can be seen by looking at figure 57, the only noticeable defects were located at the corners of the substrate, and attributed to the effect of superficial tension, creating accumulation of solvent in those regions during the thermal treatment on hot plate at 400 °C between consecutive runs. Considering this, deposition via a spin coating method can be imagined to be applicable even on larger substrates, because of its intrinsic ability to give a uniform deposit over relatively extended areas and also thanks to the discrete reproducibility of the fabricated films.

In order to assess crystallographic properties, XRD data exemplified by the spectrum in figure 60 were collected. In the graph, blue markers are employed to locate peaks relative to bismuth vanadate, while green ones are instead utilized for cassiterite peaks originated by the underlying FTO substrate.
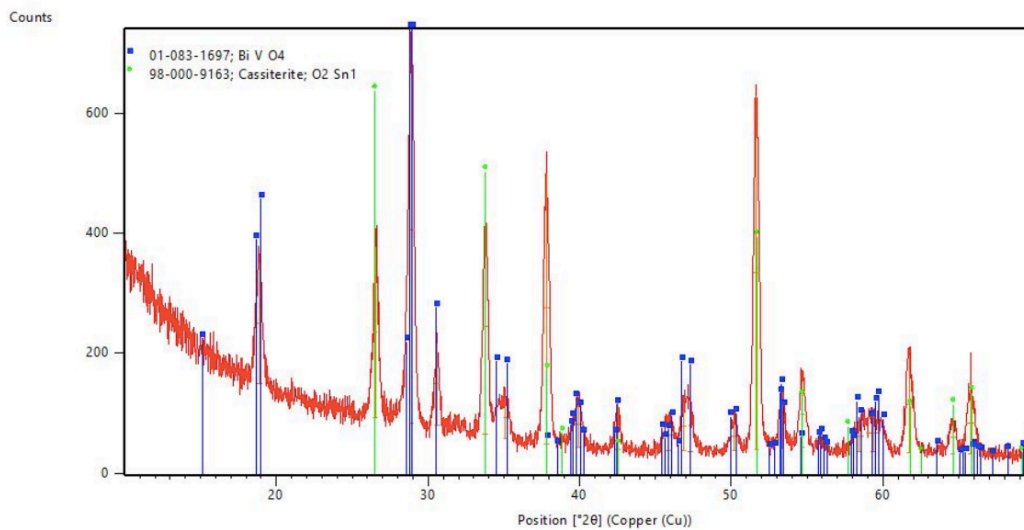
Figure 60. XRD spectrum of a Mo:BiVO₄ photoanode produced via spin coating of 5 layers deposited on top of each other.

As in the cases of drop casting of Mo doped $BiVO_4$ over FTO and over the seed layer described before, also in this configuration the three characteristic peaks originated by the monoclinic scheelite crystal structure of $BiVO_4$ are present, and they have similar relative intensities as well: the one relative to the (121) family of planes at 28.9°, the one of the (110) and (001) families at 19° and the one for the (040) family at an angle

of 30.6°. For what concerns the peaks that would be originated by a tetragonal structure at 24.4° and 32.7°, they're absent also in this situation, testifying a correct and virtually complete recrystallization of the material during the thermal annealing stage in the tubular furnace.

As explained before, initial research was carried out to determine how many layers were needed in order to produce the best photoelectrochemical performing photoanodes. The LSV curves resulting from deposition of 3, 5 and 7 layers of materials are reported in figure 61. A number of layers lower than 3 produced relatively negligible current density values, while going above 7 spin coating runs didn't increase the photoelectrochemical efficiency, probably because of the intrinsic limitation in regard to charge transport abilities of the deposited material, which can be felt at higher thicknesses of the photoactive material.
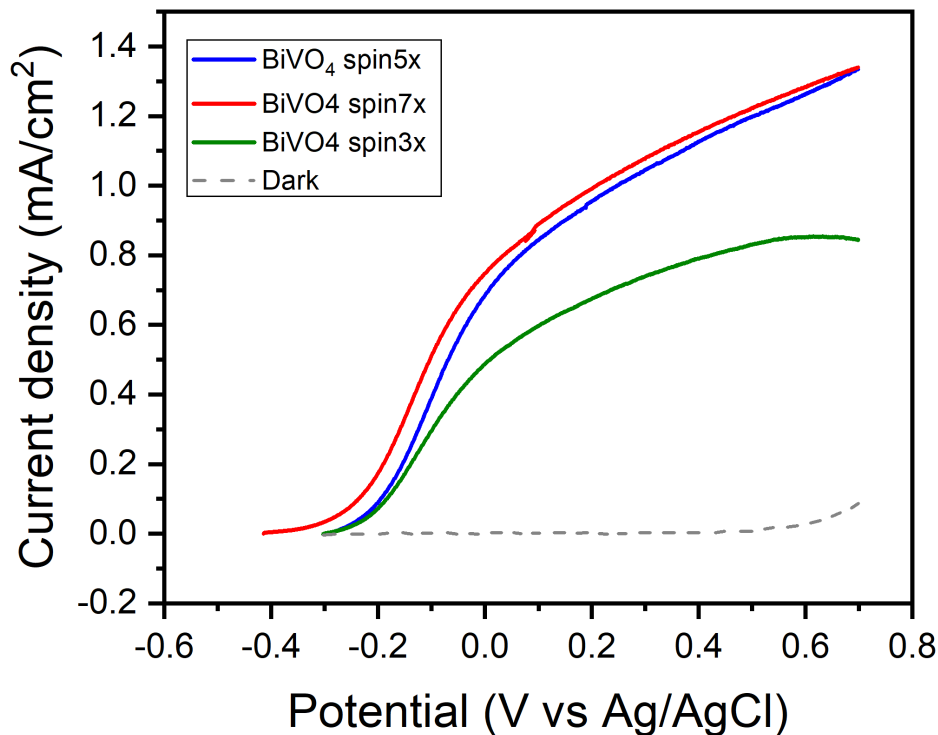
Figure 61. LSV curves obtained from spin coating deposition of BiVO₄ over bare FTO, with stacking of a different number of layers in each case.

A quick inspection immediately reveals how deposition of the lowest number of layers analyzed, so the 3 of the green curve, produces a relatively low value of current density at 0.6 V vs Ag/AgCl, which in this case measures roughly 0.85 mA/cm². The onset potential for this curve is located around -0.2 V vs Ag/AgCl, but after an interval of just roughly 0.2 V the slope rapidly decreases and reaches a saturation current a bit before the reference point at 0.6 V. In any case, the photoanodes produced by deposition of only 3 layers registered the lowest performances of all spin coating ones, since the green curve stays below the other two for the whole duration of the test. Nevertheless, deposition of 3 layers was still useful to discuss other parameters that will be addressed in the next section.

By looking instead at the other two curves, it can be seen how the one obtained by deposition of 7 layers (red) has a slightly better behavior than the one with 5 (blue), but the two are very close to each other, and the shapes are virtually equivalent. The difference between them actually decreases at higher values of applied potential, producing a current density value at 0.6 V vs Ag/AgCl of about 1.28 mA/cm² in both cases.

Evaluation of data from figure 61 was then useful for the subsequent production of photoanodes via spin coating. In general, a number of layers between 5 and 7 was expected to give better photoelectrochemical performances when tested by means of LSV. Deposition of a low number of layers gave instead much worse results, seemingly due to the fact that, below a certain thickness, the photoactive film isn't able to absorb enough of the radiation coming from the solar simulator, and cannot therefore produce a number of charged species comparable with the ones originated by thicker deposits.

As previously discussed, this kind of photoanodes presented a highly uniform appearance more or less over the whole FTO surface, exception made for small regions located at the four corners. Considering this fact, the polishing step left uncovered active areas that were considerably larger than the ones tested for drop casting specimens.

By analysis of the values registered from the LSV tests of the best performing spin coating and drop casting photoanodes, an appreciable difference in terms of

photocurrent output can be noticed. The comparison is summarized by the data collected in table 3.

Type of photoanode	Onset potential [V vs Ag/AgCl]	Current density at 0.6 V vs Ag/AgCl
Drop casting	-0.15	2.3 mA/cm^2
SILAR + drop casting	-0.08	3.3 mA/cm^2
Spin coating (best case)	-0.28	1.28 mA/cm^2

Table 2. Direct comparison of LSV characteristic values obtained from samples produced via drop casting vs spin coating methods.

The current density values at the reference point of the 3 types of samples differ of roughly 1 mA/cm^2 from each closest neighbor, proving clear discrepancies in the obtainable performances in a hypothetical use for a photoelectrochemical cell. Other than the improvement in regard to uniformity of the films, the spin coating method allowed to obtain slightly lower values of onset potential, which can be a great enhancement if the curve shows appreciable positive slope. After this initial improvement, the plot relative to spin coating is located below the other two for the rest of the test's duration. As anticipated when discussing the SEM and AFM analyses, these differences in performances can be reconducted to the much higher porosity that is observed for drop casting samples. Allowing the best possible charge transfer from the semiconductor to the electrolyte solution is in fact of crucial importance in order to cause oxidation and avoid charge recombination within the film itself.

Considering these factors, the following experimentation phase aimed at finding a way of improving the quality of spin coating photoanodes in terms of current density output, having already achieved good results from the point of view of homogeneity and reproducibility of the specimens.

4.3 Heterojunction with SnO$_2$ deposited via spin coating

Apart from the considerations made regarding the superficial extension of the semiconductor-electrolyte interface in the case of spin coating deposition, and the

obvious change in performances with respect to drop casting, other phenomena were investigated to try improving the performances of the photoanodes produced via spin coating. In particular, the deposition of a thin layer of undoped tin oxide in between the $BiVO_4$ photoactive film and the FTO substrate was employed in order to reduce charge recombination events, according to the principles explained in section 2.5.3. The contribution of tin oxide is felt as the new, modified band structure helps the extraction of electrons and the separation of charges, which ultimately means that more oxidation reactions can occur at the electrode-electrolyte interface.

For the part of the production concerning fabrication of the SnO_2 thin layer, the main references that were utilized were the studies by Byun et al. *(46)* and Luo et al. *(54)*, and the films were produced via spin coating. Initially, two precursor solutions with different concentrations of $SnCl_2$ $2H_2O$ dissolved in isopropyl alcohol were tested, a 0.1 M and a 0.2 M one (refer to section 3.1.2). After preliminary studies, it was decided to utilize only the solution at higher concentration, as in general the influence of the tin oxide layers produced with it was more pronounced, as observed by analysis of the LSV plots collected with the corresponding photoanodes.

Since it is reported in literature that the SnO_2 hole-blocking layer can influence the features also of the above deposited film, the study was initially devoted to optimizing the characteristics of the $BiVO_4$ film, analyzing it with the usual techniques exploited in the other cases and evaluating photoelectrochemical efficiency via LSV. Later on, the focus was shifted on the tin oxide layer's characteristics, and on how different configurations could influence the performances of the photoanodes.

4.3.1 SnO_2 characterization and variation of the $BiVO_4$ layer

For this section, the results collected from the spin coating of the photoactive film on bare FTO was taken as a starting point. By looking at the LSV results exemplified in figure 61 it was then decided to keep the SnO_2 layer in a steady condition and vary the characteristics of the above deposited $BiVO_4$ with application of 3, 5 or 7 layers with the same parameters utilized before (spin coating for 25 s at 1000 rpm). For what concerns instead the production of the hole-blocking layer, the parameters set for the

spin coater were fixed at a speed of 2000 rpm for 30 seconds. After the run was completed, the samples were placed onto a heating plate in open air for 1 hour at a temperature of 500 °C. As it is widely reported in literature, this passage produced a SnO_2 film in a cassiterite type rutile tetragonal structure, which was also confirmed by XRD measurements. *(66) (67)*

At first, careful analysis of the SnO_2 layer (mainly from a morphological standpoint) was performed in order to better understand the features of the $BiVO_4$ that would have been deposited on top of it. Images obtained via SEM are collected in figure 62.
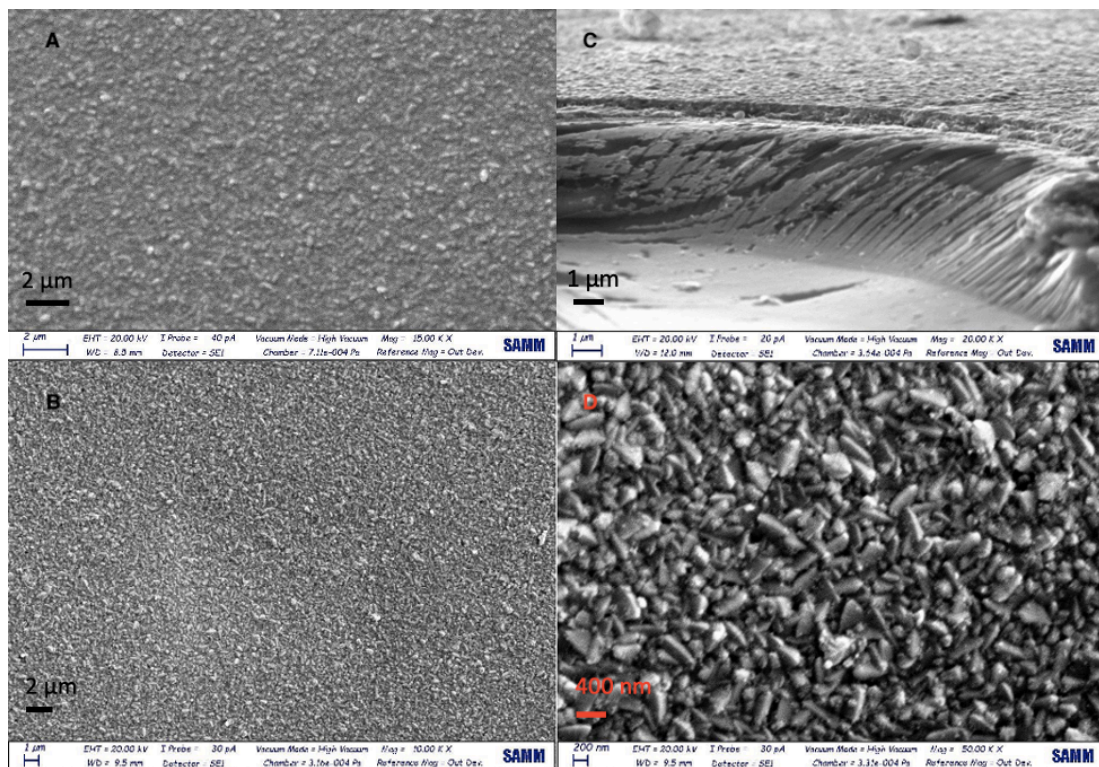
Figure 62. A: SEM image at 15Kx magnification of the SnO_2 layer deposited at 2000 rpm over FTO; C: side view of SnO_2 on top of FTO at 20Kx magnification; B, D: SEM images at 10Kx and 50Kx of FTO.

As it was expected from the utilization of a spin coating technique, the pictures collected (images A vs B in figure) show a more compact morphology for the SnO_2 layer with respect to the case of bare FTO. This is believed to be due to the fact that the voids in between the large FTO grains (observable in image C) are filled by the presence of the finer SnO_2 ones, resulting in a smoother surface. As in will be shown later, these differences in compactness and smoothness in the two cases produced some

modifications also upon the morphology of the spin coated $BiVO_4$, and therefore on the overall performances of photoanodes during LSV tests.

Three dimensional graphs produced via AFM measurements were coherent with what was observed in the pictures. The surface portion depicted in figure 63 looks in fact rather smooth, with a very reduced difference of 14.4 nm between the lowest and highest points detected by the microscope's probe. Average roughness of the surface was just slightly above 1 nm for this particular area.
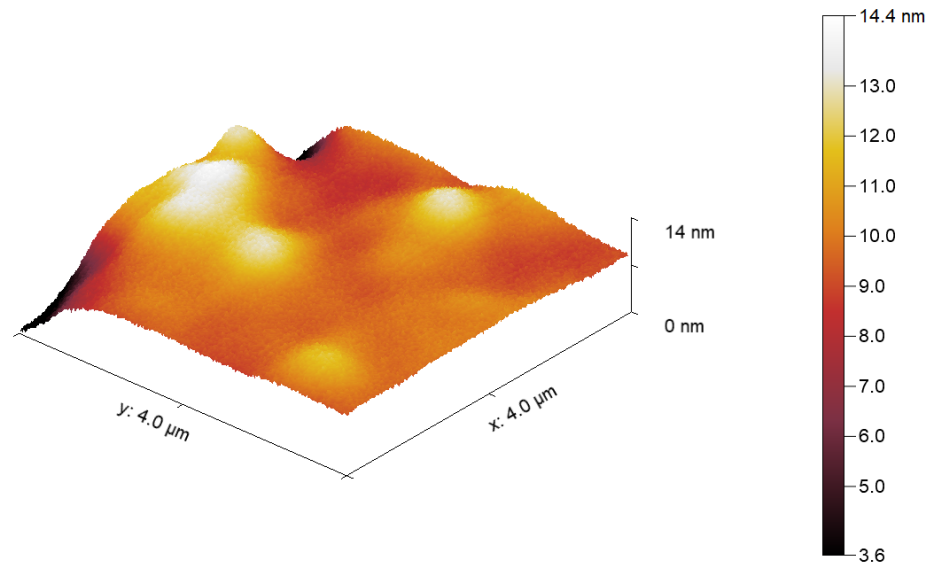
Figure 63. 3D graph resulting from AFM measurements of the SnO₂ hole-blocking layer deposited on top of FTO.

A base layer of this type was expected to influence the above laying $BiVO_4$ deposits by causing formation of a smoother surface than in the case depicted in figure 58, even at lower numbers of spin coating runs, so lower thicknesses.

For what concerns instead the structure of the tin oxide deposit produced after calcination on a hot plate, the XRD spectrum collected and depicted in figure 64 shows only the presence of peaks related to cassiterite, located in particular at angles measuring 26.6°, 33.9° and 51.8°, in decreasing order of intensity.
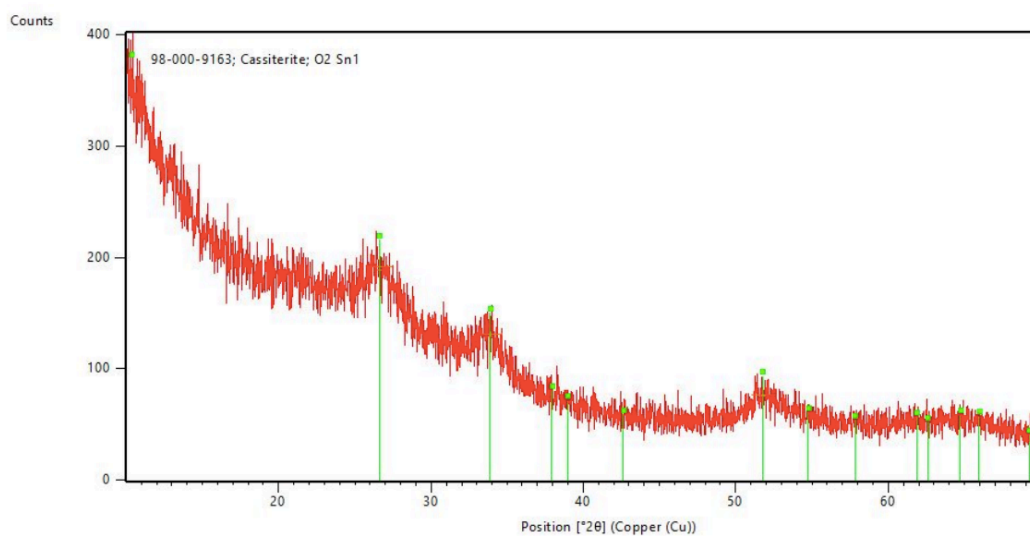
Figure 64. XRD spectrum obtained from analysis of the thin layer of the SnO_2 produced via spin coating.

Comparing the spectrum with those of the FTO detected under the $BiVO_4$ films discussed in previous sections, the obvious difference comes from the low relative intensity of cassiterite peaks with respect to the rest of the curve, and at the same time from their much larger width. These two information allow to conclude that the tin oxide layer was formed without long range translational order and was therefore presenting a prevalently amorphous structure rather than a crystalline one.
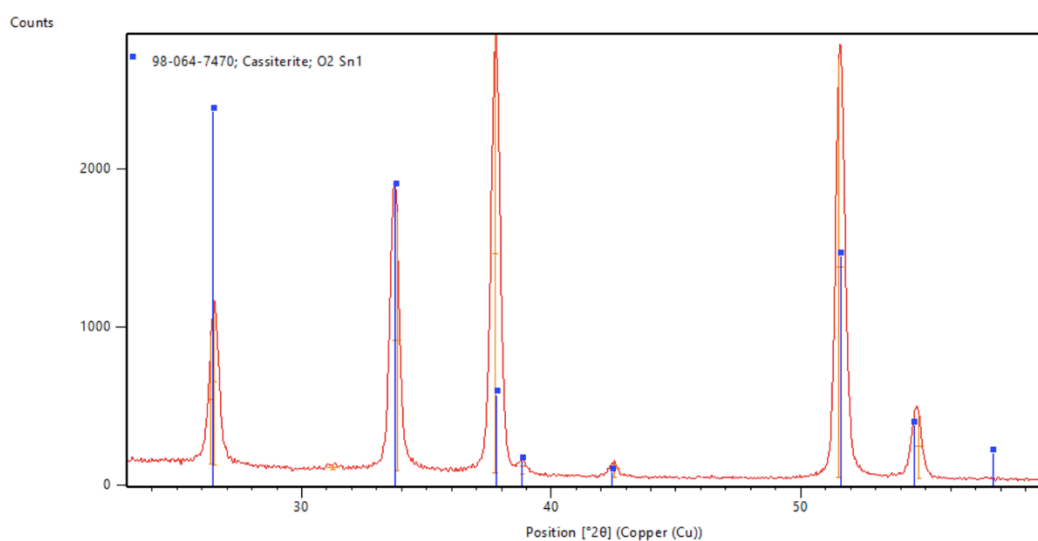
Figure 65. XRD spectrum obtained from an FTO sample.

A quick comparison with the spectrum in figure 65 obtained from an FTO sample, presenting a much more crystalline structure, can give further confirmation of these assumptions.

After assessing the characteristics of the tin oxide layer, $BiVO_4$ was deposited via spin coating in order to produce the final photoanodes as desired. As discussed before, results obtained from deposition on bare FTO were the starting point for this step, so the same three thicknesses obtained with 3, 5 and 7 spun layers were analyzed to appreciate the difference between the two configurations. Process parameters were kept as for spin coating on FTO, including the annealing stage in tubular furnace, in order to ensure that the photoactive part of the deposit exhibited the same characteristics of before, apart of course from those influenced by the SnO_2 over which it was fabricated.
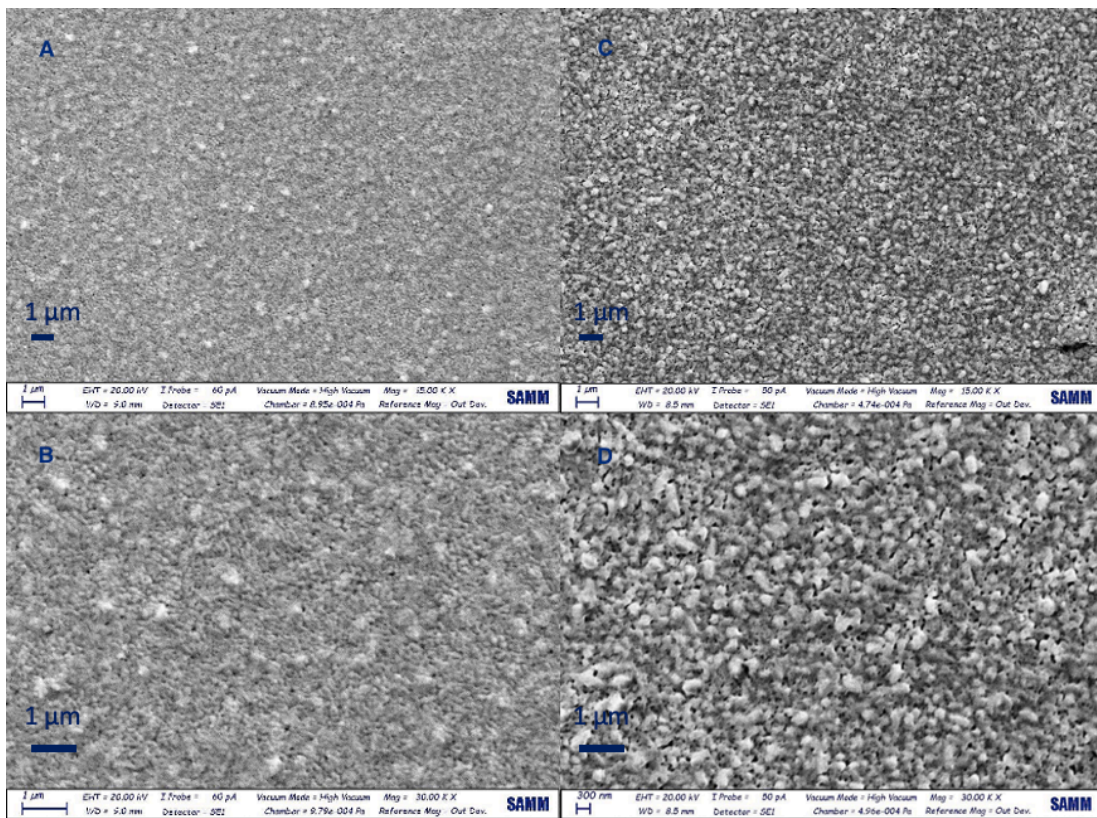
Figure 66. On the left, images obtained from a sample produced with BiVO₄ spin coated over a thin SnO₂ layer, at 15kX (A) and 30kX magnification (B). On the right, the images at the corresponding magnifications for BiVO₄ spin coated over bare FTO (C, D).

110

Images resulting from SEM analysis allowed to evaluate differences in the microscopical surface appearance of $BiVO_4$ when spun over SnO_2 instead of over bare FTO. By looking at the four pictures compared in figure 66, referred to a sample with the same number of photoactive film layers in the two cases, a more compact morphology can be observed when $BiVO_4$ is fabricated over the SnO_2 layer, allowing to evaluate the effect that the latter produced from the point of view of surface morphology on the photoactive film; it can be seen how a smoother layer of SnO_2 results in a more dense photoactive film, and vice versa in regard to the rougher FTO surface. This aspect was predictable by observing the AFM graph relative to the tin oxide surface in figure 63.

Surface morphology characteristics were evaluated also via analysis of AFM data. For spin coating $BiVO_4$ samples fabricated over SnO_2, the graph depicted in figure 67 can be taken as a reference.
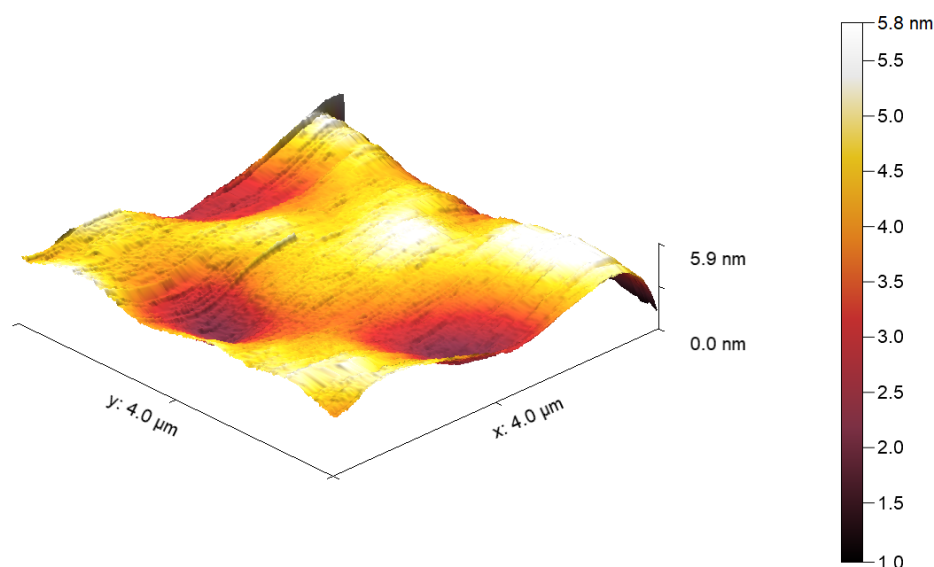
Figure 67. 3D graph resulting from AFM analysis of a photoanode produced via BiVO₄ spin coated over a SnO₂ thin layer.

Coherently with the images in figure 66 and with what was expected from previous analysis of the SnO_2 layer's morphology, also the surface of the photoactive film was rather smooth, with a maximum valley-peak difference of just 5.8 nm over the scanned area, and a mean roughness even below 1 nm.

To assess crystalline configuration of the $BiVO_4$ layer, XRD analysis was performed on the photoanodes, producing the graph in figure 68.
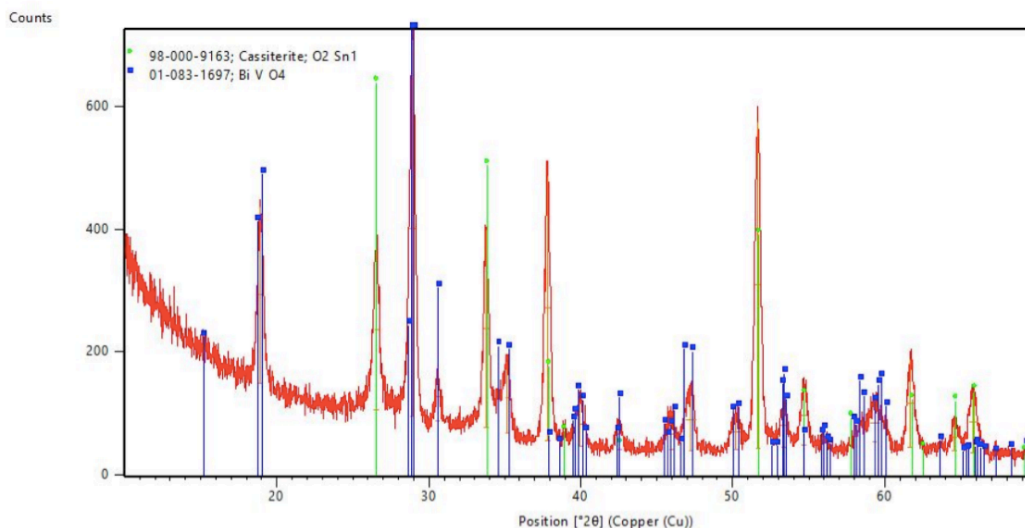
Figure 68. XRD spectrum of a photoanode fabricated by spinning the Mo:BiVO₄ solution (5 layers)
on top of SnO₂.

As for all the other methodologies of production employed for this work, also in this case the most important peaks corresponding to the monoclinic scheelite structure of bismuth vanadate (marked with blue squares in figure 68) can be easily spotted at 29°, 19° and 30.6°, while the absence of the peaks at 24.4° and 32.7° can be registered again as a sign of the absence of the tetragonal crystalline form after the annealing in tubular furnace. By comparing this last graph with the one for $BiVO_4$ spin coated on bare FTO represented in figure 60, it is possible to estimate a similar degree of the crystallinity in the two cases, because of the similar widths and relative intensities of the peaks related to the monoclinic scheelite structure.

The photoelectrochemical performances of photoanodes produced via spin coating of molybdenum doped bismuth vanadate on top of tin oxide were evaluated by means of LSV. In figure 69, the plots obtained from samples fabricated via deposition of 3, 5 and 7 layers of photoactive material are represented. As explained before, these values were chosen on the basis of the results obtained from deposition on bare FTO, and to correlate performances in the two cases. This made then possible to quantify the influence of the hole-blocking layer upon the overall efficiency of the electrodes.

As it was observed already from the spin coating on bare FTO, also in this case the photoanode with the thinnest of the three deposits (green curve, corresponding to 3 layers of $BiVO_4$ on SnO_2) behaved much worse than the thicker counterparts; its onset potential was in fact located at more positive values, and also the current density measured from the reference point at 0.6 V vs Ag/AgCl was of just 0.68 mA/cm², as a result of the inconsistent slope achieved after the onset potential.
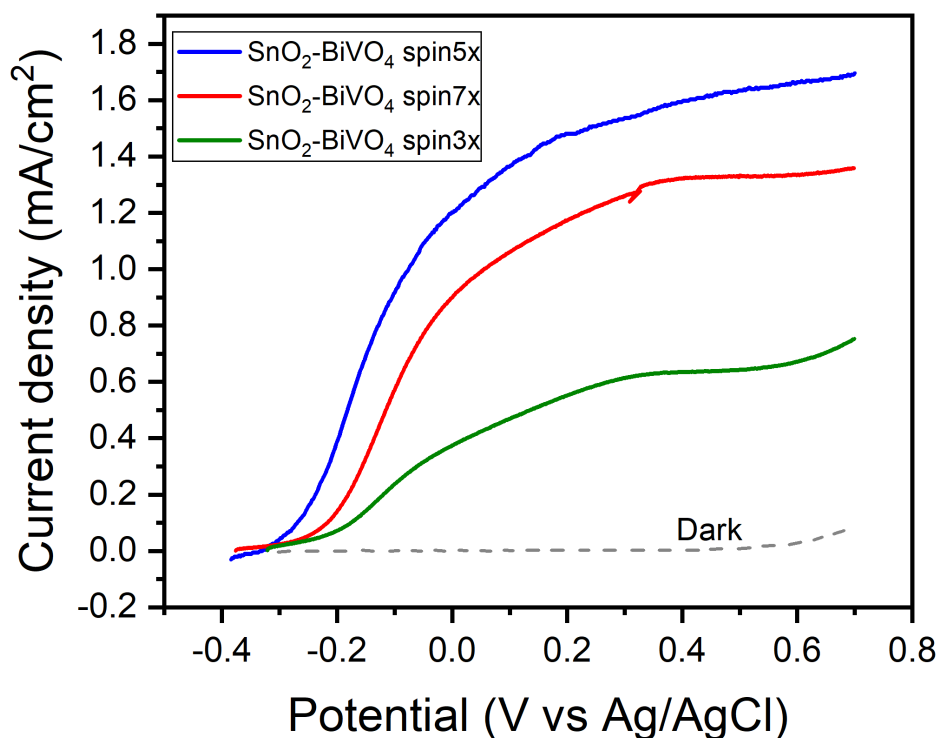
Figure 69. *LSV plots obtained by testing the photoanodes fabricated via spin coating of Mo:BiVO₄ in three different thicknesses above SnO₂.*

The situation is surely more interesting for the curves corresponding to 5 and 7 spun layers, which were almost identical for $BiVO_4$ on bare FTO. In this case, the difference is very noticeable from a quantitative point of view; the two curves share in fact a similar shape, but the one corresponding to 5 deposited layers shows better performances, registering an onset potential of -0.3 V vs Ag/AgCl and a current density at 0.6 V vs Ag/AgCl of 1.68 mA/cm², while the corresponding values in the case of the 7 layers curve are of -0.26 V vs Ag/AgCl and 1.35 mA/cm².

In order to allow easier interpretation of the effect of the SnO_2 hole-blocking layer on the final shape of the LSV curves, in figure 70 the two curves obtained with and without its presence were collected for each of the three tested thicknesses.
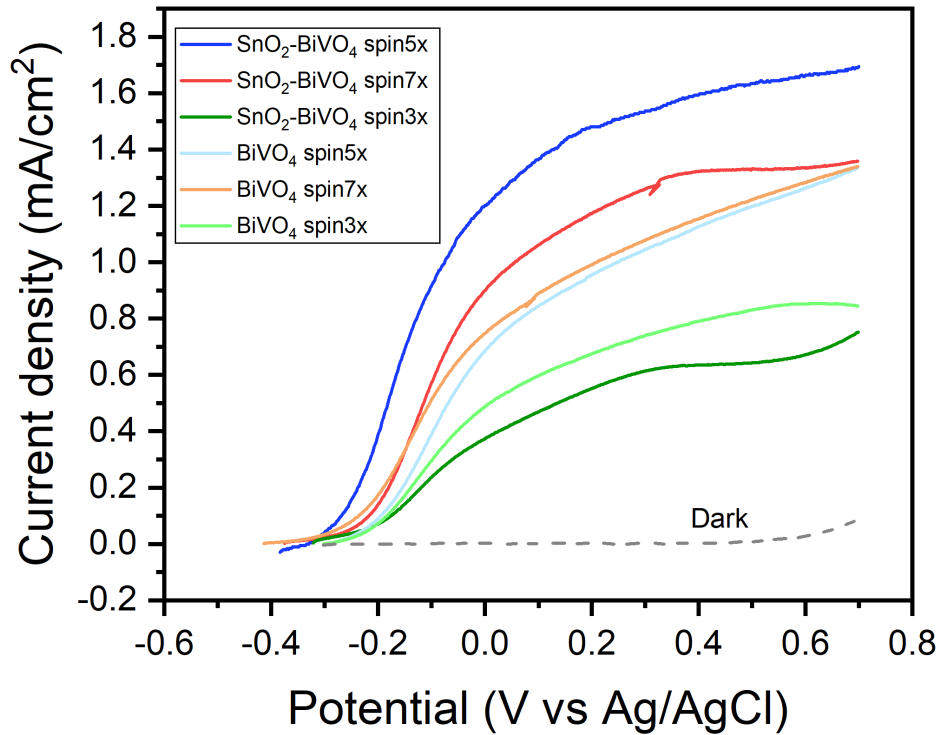
Figure 70. Recap of the LSV plots obtained with or without application of the hole-blocking layer for photoanodes produced via spin coating of 3, 5 and 7 photoactive layers.

For simplicity, the two curves associated to the same number of $BiVO_4$ layers are represented with the same color in its darker shade when it's deposited above SnO_2, and lighter when it's on bare FTO.

Analyzing the curves with 5 and 7 layers, the improvement in performances imparted by the SnO_2 is pretty obvious, especially for the 5 layers, which benefit from a more negative onset potential value and clearly separates from the second-best curve of the tested samples, that is the one obtained from 7 layers of $BiVO_4$ spun above FTO.

The situation is different for the curves obtained from the 3 layers configuration, in whose case the presence of the hole-blocking layer didn't generate appreciable differences on photoelectrochemical performances. Nevertheless, modifications

114

introduced in this particular case are not very consistent with respect to the improvements in the other two, and moreover the dark green curve of the graph shows a small drop in the current density value around 0.6 V vs Ag/AgCl, meaning that the distance between the two curves of the 3 layers configuration would be even smaller with a more standard behavior. This is believed to be due to the fact that deposition of only 3 spin coating layers did produce a not thick enough $BiVO_4$ deposit, whose characteristics were too dependent from experimental conditions, and so different in the case of the two samples analyzed here. Therefore, the influence of the SnO_2 layer cannot be reasonably evaluated by observing the two green curves. The low thickness of the 3 layers configuration was already observed for spin coating on bare FTO (refer to graph in figure 61).

In table 3, the effects introduced by the tin oxide layer upon onset potentials and current densities at 0.6 V vs Ag/AgCl are summarized to provide quicker interpretation of the already presented graphical data.

Number of $BiVO_4$ layers	Variation induced on the onset potential [V]	Variation induced on the current density at 0.6 V vs Ag/AgCl [mA/cm²]
3	~ 0	- 0.17
5	- 0.1	+ 0.4
7	+ 0.02	+ 0.1

Table 3. Difference in the values of onset potential and current density obtained for the 3, 5 and 7 $BiVO_4$ layers configuration with introduction of the SnO_2 layer.

It is immediate to notice the greater beneficial variations of the SnO_2 layer upon performances of the 5 layers configuration; for what concerns the current density value used as benchmark, the positive increment was an appreciable 31.25% with respect to the value of 1.28 mA/cm², obtained for the application over bare FTO. The two curves at 5 and 7 layers showed therefore a difference that was not present before application of the SnO_2 layer. This separation was attributed to the fact that, when the samples are illuminated in front, electrons in the 7 layers configuration have to cover a longer distance than those in the 5 layers one, resulting in higher probabilities of recombination events. As it will be discussed in the last part of this section,

photoanodes produced with $BiVO_4$ deposited on top of SnO_2 presented in fact better performances in front illumination conditions, differently from those fabricated on bare FTO.

The improved performances of photoanodes introduced by the presence of a hole-blocking layer are of course to be attributed to the modified electronic band configuration created (shown in figure 28, section 2.5.3), but the different morphology of the anode-electrolyte interface must be addressed as well. As observed from comparison of spin coating samples with drop casting ones, and coherently with many studies found in literature, an increase in the porosity of the outer surface of $BiVO_4$ based anodes surely helps the charge transfer to the electrolyte, boosting the kinetics of the oxidation reaction during tests. By observing the beneficial effect of a SnO_2 layer on spin coating samples, it can be deduced that the lightly reduced porosity resulting from the influence of tin oxide on morphology is less significant than its ability to reduce recombination at the $BiVO_4 - FTO$ interface. However, by comparing the photoanodes produced by spin coating on SnO_2 with those made via drop casting, it's also noticeable how a more significant reduction of the porosity, and so of the contact area with the electrolyte solution, can produce larger negative effects on the overall performances than the positive ones originated by SnO_2. Nonetheless, the spin coating method was introduced as a way to produce more uniform deposits over the whole extension of the FTO samples.

The last considerations regarding this section can be made by observing the characteristics of the curves in figure 71, which were collected in order to evaluate the difference in the photoelectrochemical performance for the electrodes produced by spin coating on tin oxide when in front or back illumination conditions. As discussed for drop casting on bare FTO (refer to section 4.1, figure 48) and in accordance with the study of Liang et al. *(45)*, $BiVO_4$ based photoanodes generally show a greater photocurrent when illuminated from the back of the electrode, because of the intrinsic crystalline structure that hinders the movement of negative charge carriers through the thickness of the material. LSV measurements highlighted instead an inversion of the behavior for the case of deposition of the photoactive layer on top of tin oxide. The curves in figure 71, all obtained from a specimen with 7 layers of $BiVO_4$ deposited, show an improvement in the current density at 0.6 V vs Ag/AgCl of roughly 0.1

mA/cm² when light hits from the side of the photoactive material, while also for the rest of the scan the front curve is located above the back one. Even if the difference is not large in absolute terms, what is important is the inverted situation with respect to the case discussed in section 4.1.
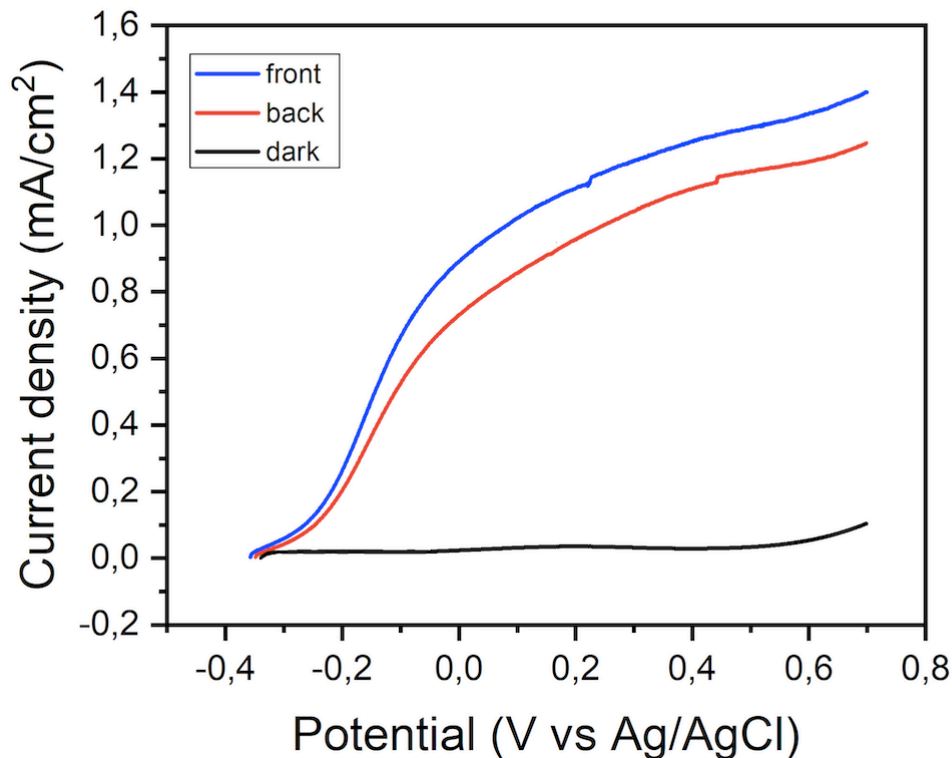
Figure 71. LSV curves showing a better photoelectrochemical performance in front illumination conditions for a sample produced by spin coating of BiVO₄ over a SnO₂ hole-blocking layer.

A possible reason for this kind of behavior may be due to the fact that, while producing a positive effect upon the overall performances of the electrodes thanks to the reduction of recombination events, the transfer of holes from the semiconducting materials to the electrolyte has worse kinetics because of the reduced surface of contact between the two. A lower efficiency in the transfer of positive charges could cause a negative effect in performances in the situation of back illumination, in which holes have to cover a longer path to reach their final destination; when light hits the front of the photoelectrode, positive charge carriers are instead in a more favorable situation, because of the shorter distance they have to travel across.

117

At the same time, the problems regarding limited charge transfer for the electrons that were described as a typical feature of $BiVO_4$ films in the drop casting on bare FTO section are partially reduced because of the denser $BiVO_4$ morphology produced by spin coating on SnO_2; so, the negative shift of the back curve is accompanied by a lightly positive one of the front one. As widely demonstrated in literature, denser deposits with well interconnected particles are in fact responsible for better electron transfer across the film's thickness. *(68) (69) (70)*

4.3.2 Variation of the SnO_2 hole-blocking layer

As anticipated, this part of the work consisted in tuning the properties of the SnO_2 layer in order to obtain the best possible photoelectrochemical efficiency of the photoanodes. To do so, different configurations of the hole-blocking layer were produced and tested after application of the $BiVO_4$ photoactive film via spin coating. In particular, the experiments aimed at finding the best possible situation in terms of thickness of the SnO_2 deposited on FTO and resulting photoelectrochemical performances, while for what concerns the $BiVO_4$ film, samples with deposition of 5 or 7 layers were examined, because of the conclusions deducted from previous analyses.

In order to fabricate tin oxide films presenting different thicknesses, two ways were investigated: at first, a spin coating deposition at varying values of rpm, which would of course give thicker deposits at lower rpm; as an alternative method, a multilayer configuration was investigated as well. In this last case, apart from the final annealing at 500 °C for 1 hour applied normally, a quick step of about 3 minutes onto a heating plate at 150 °C was exploited to ensure evaporation of the solvent in between consecutive spin coating runs.

Since the conclusions taken from the last section indicated a positive effect on performances originated by the relatively smooth morphology of SnO_2 when compared to FTO, the first choice was to try producing a thicker hole-blocking layer, to create a larger physical separation from the underlying FTO. Therefore, samples were produced by applying a spin coating speed of 1000 rpm for 30 seconds (halving the

value that was used previously) for the SnO$_2$ film, before application of the photoactive layers also via spin coating. As expected, produced films were thicker than before, but the speed at which samples were rotating was still enough to guarantee a smooth surface.

By directly looking at the SEM images of the SnO$_2$ surface, it is rather difficult to precisely address this kind of variation, since a precise individuation of the interface region between FTO and SnO$_2$ id very difficult. It was instead much easier to locate the line corresponding to the interface between FTO and the underlying glass. Analyses performed over the cross section of samples, illustrated in figure 72, were then useful to give an idea of the difference in thickness of the FTO + SnO$_2$ deposits in the two cases.
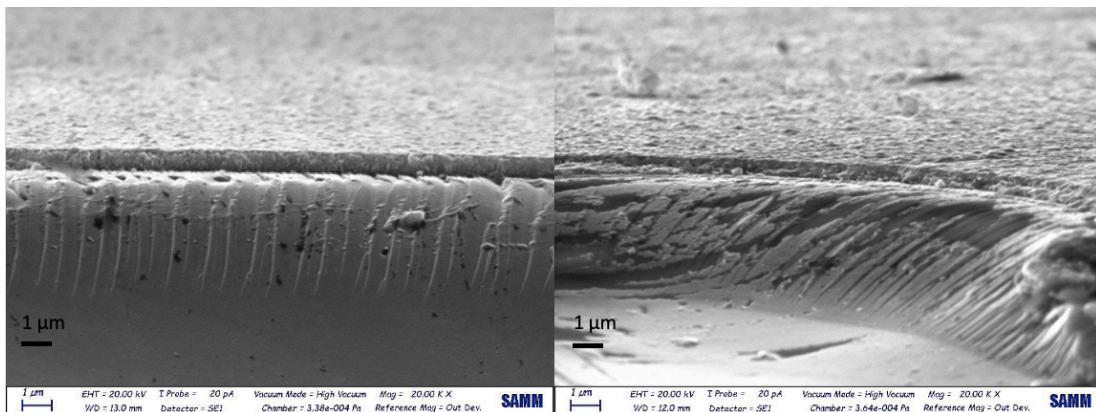
Figure 72. Direct comparison of the SnO$_2$ film's thickness in the case of deposition at 1000 rpm (left) or 2000 rpm (right). Both images were obtained at 20Kx magnification.

The vertical difference between the two images obtained via software analysis was in the order of tens of nanometers, and knowing the FTO's thickness was the same for both samples, it was attributed to the differences between the SnO$_2$ layers.

From what is reported in the work of Byun et al. *(46)*, a thicker tin oxide layer deposited above the FTO shows a more compact, smoother morphology. It was then reasonable to expect the same kind of influence already registered on the BiVO$_4$ film, but in a more pronounced way, helping the transfer of negative charges across the photoactive deposit as described for the samples discussed in the last section.

Photoelectrochemical assessment performed via LSV revealed better performances of the photoanodes produced via deposition on the thicker SnO_2. The curves produced for samples with 5 and 7 layers of photoactive film are depicted in figure 73.
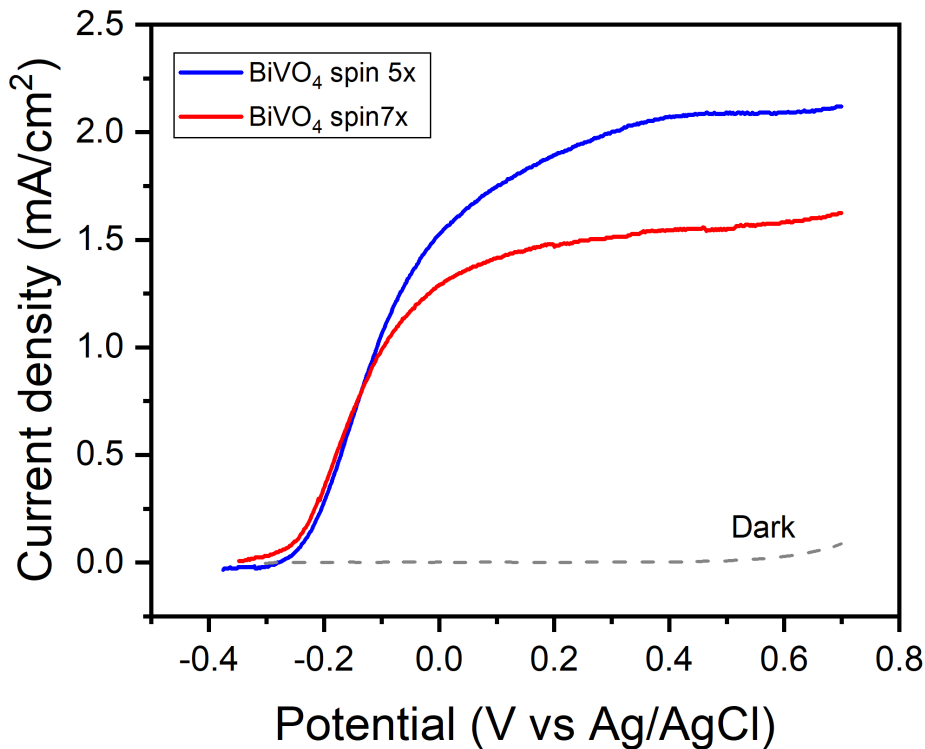
Figure 73. LSV curves obtained via spin coating of 5 and 7 layers of BiVO₄ above a SnO₂ hole-blocking layer fabricated via rotation at 1000 rpm.

The improvements with respect to the case of a thinner SnO_2 layer (refer to figure 69) are pretty clear: for the 7 layers sample, the onset potential is just very slightly shifted to the left, but the greater positive slope results in a higher curve that produces a current density value at 0.6 V vs Ag/AgCl equal to 1.6 mA/cm²; for what concerns the 5 layers one, the onset value is again pretty much the same, and the curve reveals better photoelectrochemical performances too, registering an output of 2.1 mA/cm² at 0.6 V vs Ag/AgCl. The current density gains at the reference value for benchmarks in the two cases are expressed in table 4, with the percentage over the total current density value obtained with the SnO_2 layer spun at 2000 rpm.

N° of BiVO$_4$ layers	Current density gain at 0.6 V vs Ag/AgCl [mA/cm²]	Gain % with respect to the original values
7	+ 0.25	+ 19 %
5	+ 0.42	+ 25 %

Table 4. Quantification in absolute value and in percetage of the variation in the reference values of photocurrent obtained by fabrication of a thicker SnO$_2$ layer.

From the percentage values over the previous current densities, an appreciable gain of performances can be observed for both configurations. Two factors were believed to be the main causes of the enhancement; first of all, as it was verified for the case of SnO$_2$ spun at 2000 rpm vs bare FTO, also in these conditions it is possible to hypothesize how the smoother morphology of the hole-blocking layer resulted in a denser BiVO$_4$ deposited film, in which electron transport was enhanced thanks to the improved interconnectivity between the particles (as explained in the very last part of previous section), but to a higher extent than in the previous situation. The smoother finishing of the SnO$_2$ layer obtained in this case was due to the higher thickness of the deposit itself, which created a physically larger distance from the much more irregular FTO morphology.

As for the second factor influencing photoelectrochemical performances, in the reference study proposed by Byun et al. *(46)* it is reported how a thin SnO$_2$ layer could possibly leave some very limited areas of FTO exposed, which would then come into contact with what is deposited above, so the photoactive film in this case. This would of course be the source of recombination of charges across the BiVO$_4$ – FTO interface according to the mechanism depicted in figure 28 (section 2.5.3), that could have been a limiting factor for the case of SnO$_2$ spin coated at 2000 rpm. This hypothesis is consistent with the feature sizes that can be estimated by looking at SEM images of the large FTO grains (figure 62, D) compared to the thickness of the SnO$_2$ layers fabricated on top of them (figure 72), since the typical dimensions of an FTO grain were around 300 nm or more, while the thickness difference measured for deposition of tin oxide at different spinning speeds was in the order of tens of nanometers.

Fabrication of a thinner SnO$_2$ layer on top of FTO was investigated as well, with spin coating deposition set at 3000 rpm for 30 seconds. The resulting LSV curve obtained

after $BiVO_4$ spin coating is represented in figure 74, together with the ones relative to SnO_2 deposition at 2000 and 1000 rpm, and the one from $BiVO_4$ fabricated above bare FTO.
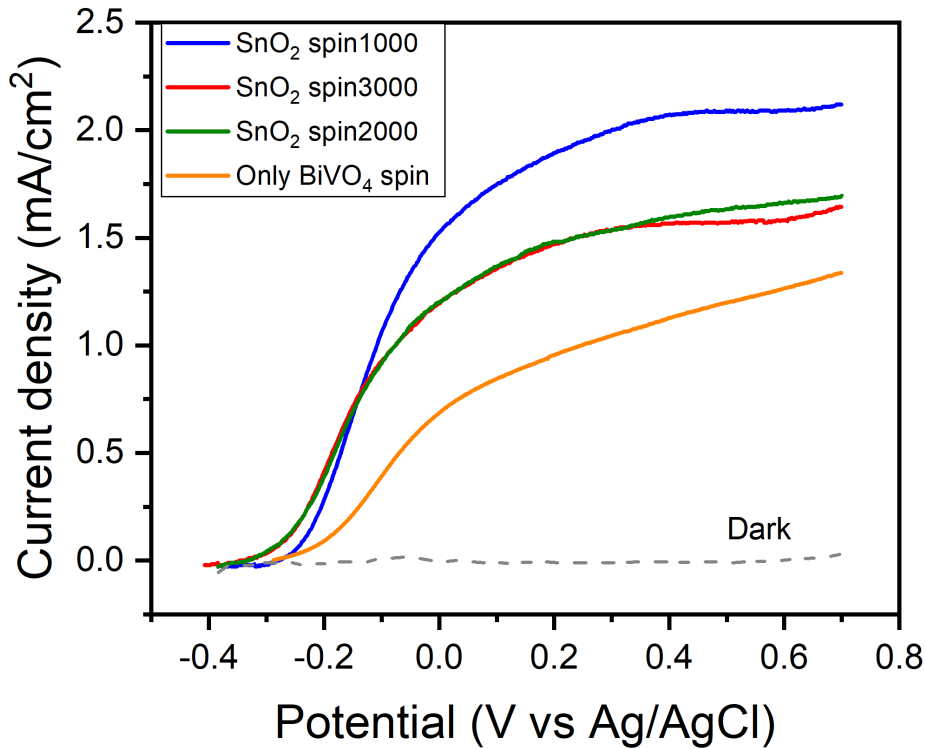
Figure 74. LSV curves obtained from deposition of $BiVO_4$ on three different types of SnO_2 layers, and on bare FTO.

All of the curves in the graph are referred to samples with 5 layers of $BiVO_4$ deposited via spin coating. For what concerns the one relative to 3000 rpm for the deposition of the hole-blocking layer, no significant difference in performance is observed with respect to the one at 2000 rpm. This could mean that the speed of the rotating plate cannot further decrease the thickness of the tin oxide deposit on FTO. Anyways, from previously gathered considerations, the effect of a thinner SnO_2 could only be detrimental, leaving larger areas of FTO exposed for the $BiVO_4$ deposit.

To determine the effect of an even thicker SnO_2 layer than the one produced with spin coating at 1000 rpm, deposition of the hole-blocking layer at a speed of 500 rpm was performed as well. By observing figure 75, the resulting curve after deposition of 5

BiVO$_4$ layers was completed can be compared with the one obtained from photoanodes with SnO$_2$ at 1000 rpm.
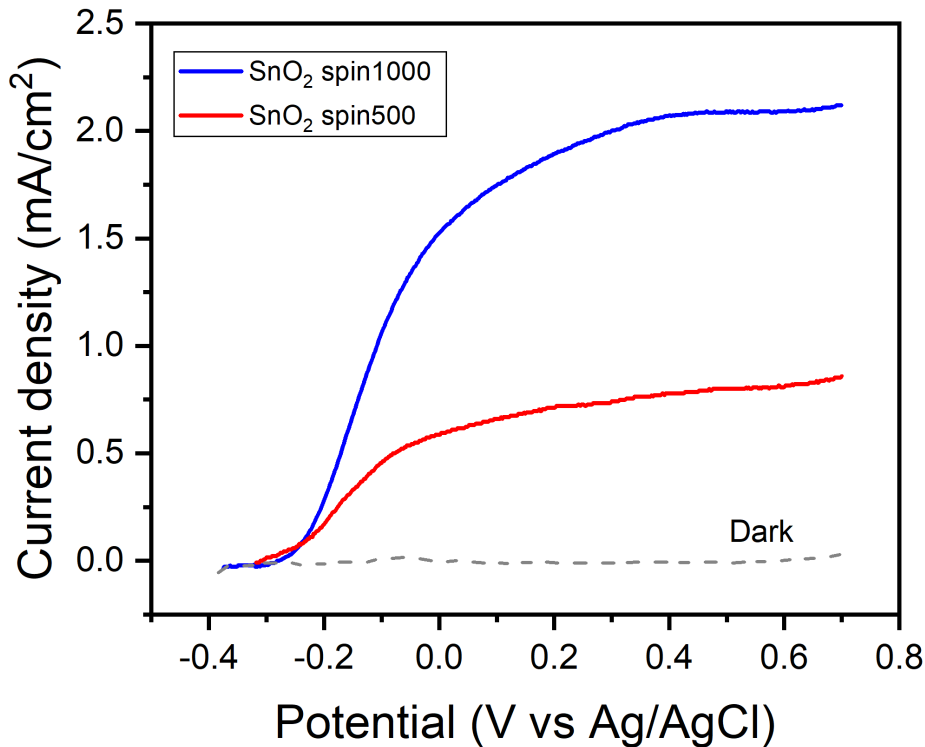
Figure 75. LSV curves obtained from photoanodes with SnO$_2$ spin coated at 1000 rpm (blue) vs 500 rpm (red).

As clearly visible from the huge difference in current density output, going above a certain thickness proved to be detrimental for photoelectrochemical performances of the samples. The reference value for the red curve was in fact of only 0.8 mA/cm^2, which is even lower than the 1.28 mA/cm^2 obtained for BiVO$_4$ on bare FTO. It must be then concluded that in this case the effect of the SnO$_2$ layer was detrimental for the functioning of electrodes. The reason was attributed to the fact that a too thick tin oxide layer can actually obstruct the flux of charged species in general; the electrical resistance of the whole stack of deposited material in its vertical direction (the one along which charges travel) was increased above a critical threshold because of the relatively resistive nature of SnO$_2$. *(71) (72)*

An additional problem as relevant as the latter can be traced to the fact that spin coating of the utilized solution below a certain rpm value caused a non-optimal distribution along the FTO surface, with inhomogeneous thickness that compromised the discussed beneficial effects of the hole-blocking layer on both the electronic band structure and the morphology of the photoactive layers.

From what emerged from the analyses of the fabricated samples, it can be then concluded that the thickness of the SnO_2 deposit must be kept within a certain range in order to exploit all of its favorable effect on photoelectrochemical performances. A too thin layer doesn't in fact produce the best modifications in terms of morphology of the $BiVO_4$ film, not granting the observed advantages in terms of transport ability of negative charges. On the other hand, if the SnO_2 layer gets too thick, as in the case of the one produced at 500 rpm, resistivity of the photoanode compromises the passage of charges, deteriorating performances of the electrodes.

To conclude the discussions related to thickness of the hole-blocking layer and its influence on the produced LSV graphs, an alternative method to modify the thickness with respect to the one obtained at 2000 rpm was evaluated.
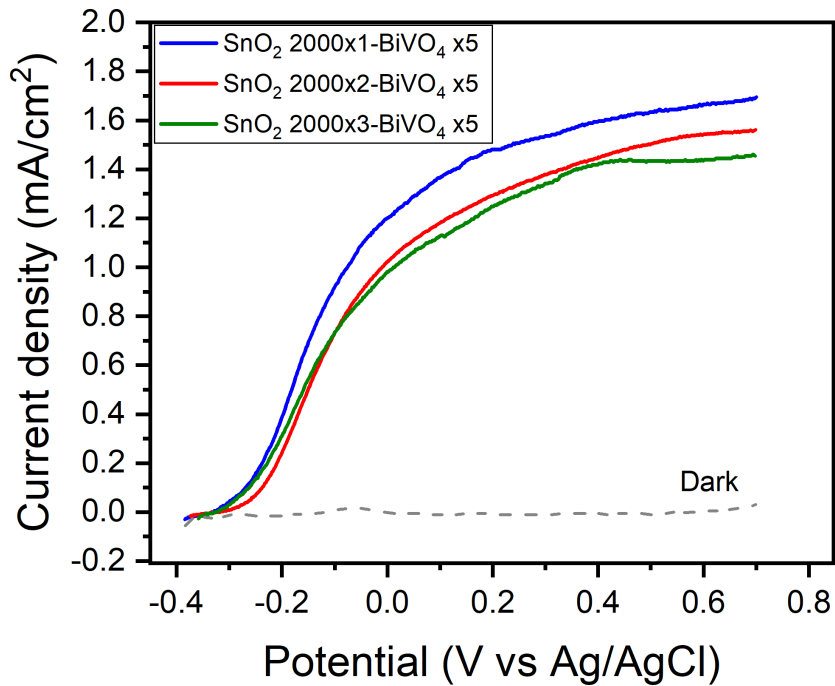
Figure 76. LSV curves obtained by photoanodes with 1, 2 and 3 layers of SnO₂ deposited in between FTO and BiVO₄.

Samples produced via deposition of 2 and 3 layers of SnO_2 spin coated above FTO at 2000 rpm for 30 seconds were prepared with deposition of 5 $BiVO_4$ layers as usual and tested via LSV. The resulting curves are represented in figure 76, together with the one obtained from the single layer configuration.

As it can be observed the increase of thickness given by the multilayer configurations didn't improve the photoelectrochemical performances as the one originated by spin coating at lower rpm values (1000 in particular), with the produced effects being in fact negative in terms of current density outputs. As for the causes of this behavior, an imperfect integration between successive SnO_2 layers was hypothesized, with interfacial regions hindering passage of charges and causing recombination phenomena. Moreover, the increased thickness was also believed to be responsible for a higher resistivity of the whole stack, as previously discussed for deposition at 500 rpm,

5 CONCLUSIONS AND FUTURE DEVELOPMENTS

The purpose of this work was to develop an easily reproducible technique able to produce $BiVO_4$ based photoanodes with the best possible performances for potential use in photoelectrochemical water splitting. Thin film photoanodes were produced via different deposition methods onto conductive FTO substrates and tested by means of linear scan voltammetry in order to assess photoelectrochemical performances. Characterization of the electrodes was carried out thanks to SEM, AFM and XRD techniques, allowing to investigate the critical factors determining the different performances in various cases and to intervene by modifying the procedures adopted for fabrication. At first, a simple drop casting technique was evaluated in order to fabricate the samples, but in spite of the appreciable current density outputs, measuring 2.3 mA/cm^2 at 0.6 V vs Ag/AgCl of applied potential, the produced films exhibited poor uniformity along the FTO surface, and rather scarce reproducibility. Introduction of a seed layer of $BiVO_4$ nanoparticles through a SILAR method raised the current density output up to 3.3 mA/cm^2 thanks to an improved microstructure, but the limitations regarding uniformity and reproducibility of the photoanodes were still observed. A spin coating technique was therefore adopted, producing samples presenting a great uniformity of the deposit along their whole surface, but with lower levels of current density output at 0.6 V vs Ag/AgCl, measuring 1.28 mA/cm^2. Implementation of a thin undoped SnO_2 layer in heterojunction with the spin coated $BiVO_4$ film proved to be very effective in raising the photocurrent density values to a much better 2.1 mA/cm^2, after the thickness of the tin oxide layer was optimized.

The improvements in photocurrent obtained with the heterojunction for spin coating samples allowed to reach values comparable to the ones obtained via simple drop casting, even though the morphology of the surface for spin coating photoanodes was judged as a limiting factor for the efficiency of charge transfer from the semiconducting material to the electrolyte solution. One of the future goals on which research should be focused could therefore be that of finding a way to produce a greater superficial porosity for this kind of samples, with particular attention in doing so without sacrificing the beneficial effect of the denser morphology introduced by the

smooth SnO_2 base layer, which created the conditions for more interconnected $BiVO_4$ particles to form, improving its electron transport ability.

Another key point could be identified in the characteristics of the SnO_2 layer itself, and its crystallinity in particular. Modifications regarding its annealing treatment, or implementation of substances to favor its crystallization in the precursor solutions could be good candidates to create better conductivity in the material, facilitating the passage of electrons to the back contact.

For what concerns instead aspects to improve in regard to the drop casting production, a more automated and standardized methodology of production would be beneficial for achieving better reproducibility of the samples, while also the study of phenomena influencing the solvent evaporation phase must be addressed in order to better comprehend its influence on uniformity along the substrate's surface. It must be said that in general implementing automatized processes is almost essential from the point of view of reproducibility at large scale, for both drop casting and spin coating syntheses.

REFERENCES

1. Chmielewski A. G. (2005). Environmental Effects Of Fossil Fuel Combustion

2. Solomon S., Qin D., Manning M. et al. (2007). Climate Change 2007: The Physical Science Basis. Working Group I Contribution to the Fourth   Assessment Report of the IPCC

3. Crimmins A., Kolian M., Rosseel K. (2012). Climate Change Indicators in the United States (second edition)

4. Chen K., Winter R., Bergman M. (1980). Carbon dioxide from fossil fuels: Adapting to uncertainty. Energy Policy 8:318-330. 10.1016/0301-4215(80)90108-1

5. Panwar N.L., Kaushik S.C., Kothari S. (2011). Role of renewable energy sources in environmental protection: A review. Renewable and Sustainable Energy Reviews 15(3):1513-1524. https://doi.org/10.1016/j.rser.2010.11.037

6. British Petroleum Company. (2018). BP Statistical review of world energy. London: British Petroleum Co

7. Zhang H., Bruns M.A., Logan B.E. (2006). Biological hydrogen production by Clostridium acetobutylicum in an unsaturated flow reactor. Water Res 40(4):728-734. https://doi.org/10.1016/j.watres.2005.11.041

8. Kuhn K.F., Koupelis T. (2004). In quest of the universe. Jones & Bartlett Learning

9. Nelson J. (2003). The Physics Of Solar cells. World Scientific Publishing Company

10. Bisquert J. (2017). The Physics of Solar Cells: Perovskites, Organics, and Photovoltaic Fundamentals

11. Kittel C. (1996). Introduction to Solid State Physics. New York: Wiley, 1976, 5th ed.

12. Slater J.C. (1956). The Electronic Structure of Solids. Handbuch der Physik 4:1-136. 10.1007/978-3-642-62039-3_1

13. Mahato N., Ansari M., Cho M.H. (2015). Production of Utilizable Energy from Renewable Resources: Mechanism, Machinery and Effect on Environment. In: Advanced Materials Research, vol 1116

14. Millman J. (2010). Integrated Electronics, 2nd edition edn. Tata McGraw-Hill education

15. Mahmoodi M., Sundararaj U., Park S. (2012). The electrical conductivity and electromagnetic interference shielding of injection molded multi-walled carbon nanotube/polystyrene composites. Carbon 50:1455–1464. 10.1016/j.carbon.2011.11.004

16. Shaheen A. (2010). Band Structure and Electrical Conductivity in Semiconductors

17. Ashcroft N.W. (1976). Solid state physics. Holt, Rinehart and Winston, New York

18. Beranek R. (2011). (Photo)electrochemical Methods for the Determination of the Band Edge Positions of TiO2-Based Nanomaterials. Advances in Physical Chemistry DOI: 10.1155/2011/786759. 10.1155/2011/786759

19. EG & G Services, (Firm). (2004). Fuel cell handbook [electronic resource] / EG&G Technical Services, Inc. U.S. Dept. of Energy, Office of Fossil Energy, National Energy Technology Laboratory, Morgantown, WV

20. Dicks A.L., Rand D.A.J. (2018). Introducing Fuel Cells; Hydrogen Storage. Fuel Cell Systems Explained; Fuel Cell Systems Explained:1; 323-26; 350. 10.1002/9781118706992.ch1; doi: 10.1002/9781118706992.ch11

21. Glazer M.N., Oprean I.M., Bățăuș M.V. (2013). Modeling and Analysis of a Fuel Cell Hybrid Vehicle. In: Anonymous Proceedings of the FISITA 201. Springer Berlin Heidelberg, Berlin, Heidelberg, p 847

22. Husain I. (2005). Electric and Hybrid Vehicles Design Fundamentals

23. Dincer I., Acar C. (2016). Review and evaluation of hydrogen production methods for better sustainability. Alternative Energy and Ecology (ISJAEE):14-36. 10.15518/isjaee.2016.11-12.014-036

24. Nikolaidis P., Poullikkas A. (2017). A comparative overview of hydrogen production processes. Renewable and Sustainable Energy Reviews 67:597-611. https://doi.org/10.1016/j.rser.2016.09.044

25. Bockris J.O., Reddy A.K. (2000). Modern electrochemistry 2B: Electrodics in chemistry, engineering, biology and environmental science. Springer Science & Business Media

26. Sharma S., Ghoshal S.K. (2015). Hydrogen the future transportation fuel: From production to applications. Renewable and Sustainable Energy Reviews 43:1151-1158. https://doi.org/10.1016/j.rser.2014.11.093

27. Yartys V.A., Lototsky M.V. (January 01, 2005). An Overview of Hydrogen Storage Methods. In: Veziroglu T.N., Yu. Zaginaichenko S., Schur D.V. et al. (eds) Hydrogen Materials Science and Chemistry of Carbon. Springer Netherlands, Dordrecht, p 75

28. Eberle U., Felderhoff M., Schüth F. (2009). Chemical and Physical Solutions for Hydrogen Storage. Angewandte Chemie (International ed in English) 48:6608-30. 10.1002/anie.200806293

29. Sheffield J., Martin K., Folkson R. (2014). Electricity and hydrogen as energy vectors for transportation vehicles. In: Alternative Fuels and Advanced Vehicle Technologies for Improved Environmental Performance, pp 117-137

30. Muir S.S., Yao X. (2011). Progress in sodium borohydride as a hydrogen storage material: Development of hydrolysis catalysts and reaction systems. Int J Hydrogen Energy 36(10):5983-5997. https://doi.org/10.1016/j.ijhydene.2011.02.032

31. Netskina O.V., Tayban E.S., Prosvirin I.P. et al. (2020). Hydrogen storage systems based on solid-state $NaBH_4$/Co composite: Effect of catalyst precursor on hydrogen generation rate. Renewable Energy 151:278-285. https://doi.org/10.1016/j.renene.2019.11.031

32. Fujishima A., Honda K. (1972). Electrochemical Photolysis of Water at a Semiconductor Electrode. Nature 238(5358):37-38. 10.1038/238037a0

33. Van de Krol R., Grätzel M. (2012). Principles of photoelectrochemical cells. Photoelectrochemical hydrogen production. Springer, Boston, MA

34. Chen S., Wang L.W. (2012). Thermodynamic Oxidation and Reduction Potentials of Photocatalytic Semiconductors in Aqueous Solution. Chem Mater 24(18):3659-3666. 10.1021/cm302533s

35. Bak T., Nowotny J., Rekas M. et al. (2002). Photo-electrochemical hydrogen generation from water using solar energy. Materials-related aspects. Int J Hydrogen Energy 27(10):991-1022. https://doi.org/10.1016/S0360-3199(02)00022-8

36. Park Y., McDonald K.J., Choi K.S. (2013). Progress in bismuth vanadate photoanodes for use in solar water oxidation. Chem Soc Rev 42:2321-2337

37. Li Z., Luo W., Zhang M. et al. (2013). Photoelectrochemical cells for solar hydrogen production: Current state of promising photoelectrodes, methods to improve their properties, and outlook. Energy Environ Sci 6:347-370. 10.1039/C2EE22618A

38. Hernández S., Thalluri S.M., Sacco A. et al. (2015). Photo-catalytic activity of $BiVO_4$ thin-film electrodes for solar-driven water splitting. Applied Catalysis A: General; Nanocatalysis Science: Preparation, Characterization and Reactivity,

dedicated to the scientific work of Jacques C.Vedrine. 504:266-271. https://doi.org/10.1016/j.apcata.2015.01.019

39. Ding C., Shi J., Wang D. et al. (2013). Visible light driven overall water splitting using cocatalyst/$BiVO_4$ photoanode with minimized bias. Physical chemistry chemical physics : PCCP 15:4589-95. 10.1039/c3cp50295c

40. Kim J.H., Jo Y., Kim J.H. et al. (2015). Wireless Solar Water Splitting Device with Robust Cobalt-Catalyzed, Dual-Doped $BiVO_4$ Photoanode and Perovskite Solar Cell in Tandem: A Dual Absorber Artificial Leaf. ACS Nano 9(12):11820-11829. 10.1021/acsnano.5b03859

41. Rohloff M., Anke B., Zhang S. et al. (2017). Mo-doped $BiVO_4$ thin films – high photoelectrochemical water splitting performance achieved by a tailored structure and morphology. Sustainable Energy Fuels 1. 10.1039/C7SE00301C

42. Victor M., Kassiba A., García-Sánchez M. (2014). Structural and Optical properties of Molybdenum doped Bismuth vanadate powders

43. Yao W., Iwai H., Ye J. (2008). Effects of molybdenum substitution on the photocatalytic behavior of $BiVO_4$. Dalton Trans (11):1426-1430. 10.1039/B713338C

44. Rajalingam V. (2014). Synthesis and Characterization of $BiVO_4$ nanostructured materials: application to photocatalysis

45. Liang Y., Tsubota T., Mooij L.P.A. et al. (2011). Highly Improved Quantum Efficiencies for Thin Film $BiVO_4$ Photoanodes. J Phys Chem C 115(35):17594-17598. 10.1021/jp203004v

46. Byun S., Kim B., Jeon S. et al. (2017). Effects of a SnO_2 hole blocking layer in a $BiVO_4$ - based photoanode on photoelectrocatalytic water oxidation. J Mater Chem A 5. 10.1039/C7TA00806F

47. Galembeck A., Alves O. (2000). $BiVO_4$ thin film preparation by metalorganic decomposition. Thin Solid Films 365:90-93. 10.1016/S0040-6090(99)01079-2

48. Luo H., Mueller A.H., McCleskey T.M. et al. (2008). Structural and Photoelectrochemical Properties of $BiVO_4$ Thin Films. J Phys Chem C 112(15):6099-6102. 10.1021/jp7113187

49. Nguyen N.T. (2012). Chapter 4 - Fabrication technologies. In: Nguyen N. (ed) Micromixers (Second Edition). William Andrew Publishing, Oxford, pp 113-161

50. Pan L., Kim J.H., Mayer M.T. et al. (2018). Boosting the performance of Cu_2O photocathodes for unassisted solar water splitting devices. Nature Catalysis 1(6):412-420. 10.1038/s41929-018-0077-6

51. Pathan H., Lokhande C. (2004). Deposition of metal chalcogenide thin films by successive ionic layer adsorption and reaction (SILAR) method. Bull Mater Sci 27:85-111. 10.1007/BF02708491

52. Odling G., Robertson N. (2016). $BiVO_4 - TiO_2$ Composite Photocatalysts for Dye Degradation Formed Using the SILAR Method. ChemPhysChem 17(18):2872-2880. 10.1002/cphc.201600443

53. Kim J.H., Jang J.W., Jo Y.H. et al. (2016). Hetero-type dual photoanodes for unbiased solar water splitting with extended light harvesting. Nature Communications 7(1):13380. 10.1038/ncomms13380

54. Luo W., Deng J., Fu Q. et al. (2014). Nanocrystalline SnO_2 film prepared by the aqueous sol–gel method and its application as sensing films of the resistance and SAW H2S sensor. Sensors Actuators B: Chem 217. 10.1016/j.snb.2014.10.078

55. Kounaves S.P. (1997). Voltammetric techniques. In: Settle FA (ed) Handbook of Instrumental Techniques for Analytical Chemistry, pp 709-726

56. Magagnin L. (2017). Applied Electrochemistry, lecture notes

57. Leng Y. (2013). Materials characterization: Introduction to microscopic and spectroscopic methods: Second edition

58. Bindell J.B. (1992). SEM: Scanning Electron Microscopy. In: Brundle C.R., Evans C.A., Wilson S. (eds) Encyclopedia of Materials Characterization. Butterworth-Heinemann, Boston, pp 70-84

59. García R. (2002). Dynamic Atomic Force Microscopy Methods. Surface Science Reports 47:197-301. 10.1016/S0167-5729(02)00077-8

60. Casari C.S. (2015). Microscopia a forza atomica AFM. Introduzione alle nanotecnologie A+B, lecture notes

61. Erinosho T., Collins D., Wilkinson A. et al. (2016). Assessment of X-ray diffraction and crystal plasticity lattice strain evolutions under biaxial loading. Int J Plast 83. 10.1016/j.ijplas.2016.03.011

62. Wang S., Chen P., Bai Y. et al. (2018). New $BiVO_4$ Dual Photoanodes with Enriched Oxygen Vacancies for Efficient Solar-Driven Water Splitting. Advanced materials (Weinheim) 30(20):1800486-n/a. 10.1002/adma.201800486

63. Anonymous. (1970). Joint Committee on Powder Diffraction Standards. Anal Chem 42(11):81A. 10.1021/ac60293a779

64. Haji Yassin S.N., Sim A.S.L., Jennings J.R. (2020). Photoelectrochemical evaluation of SILAR-deposited nanoporous $BiVO_4$ photoanodes for solar-driven water splitting. Nano Materials Science; Special issue on nanostructured materials for energy conversion and storage 2(3):227-234. https://doi.org/10.1016/j.nanoms.2019.10.003

65. Sayama K., Nomura A., Arai T. et al. (2006). Photoelectrochemical Decomposition of Water into H_2 and O_2 on Porous $BiVO_4$ Thin-Film Electrodes under Visible Light and Significant Effect of Ag Ion Treatment. J Phys Chem B 110(23):11352-11360. 10.1021/jp057539+

66. Rasheed R., Algawi S. (2016). Annealing Effect of SnO_2 Nanoparticles Prepared by the Sol–Gel Method. Journal of Advanced Physics 5:236-240. 10.1166/jap.2016.1262

67. Yuvakkumar R., Hong S.I. (2015). Incubation and aging effect on cassiterite type tetragonal rutile SnO_2 nanocrystals. J Mater Sci : Mater Electron 26(4):2305-2310. 10.1007/s10854-015-2684-1

68. Kim T.W., Choi K.S. (2014). Nanoporous $BiVO_4$ Photoanodes with Dual-Layer Oxygen Evolution Catalysts for Solar Water Splitting. Science 343(6174):990. 10.1126/science.1246913

69. Parmar K.P.S., Kang H.J., Bist A. et al. (2012) Photocatalytic and Photoelectrochemical Water Oxidation over Metal-Doped Monoclinic $BiVO_4$ Photoanodes. ChemSusChem 5(10):1926-1934. https://doi.org/10.1002/cssc.201200254

70. Tan H.L., Amal R., Ng Y.H. (2016). Exploring the Different Roles of Particle Size in Photoelectrochemical and Photocatalytic Water Oxidation on $BiVO_4$. ACS Appl Mater Interfaces 8(42):28607-28614. 10.1021/acsami.6b09076

71. Yakuphanoglu F. (2009). Electrical conductivity, Seebeck coefficient and optical properties of SnO_2 film deposited on ITO by dip coating. J Alloys Compounds 470(1):55-59. https://doi.org/10.1016/j.jallcom.2008.03.013

72. Serin T., Serin N., Karadeniz S. et al. (2006). Electrical, structural and optical properties of SnO_2 thin films prepared by spray pyrolysis. J Non Cryst Solids 352(3):209-215. https://doi.org/10.1016/j.jnoncrysol.2005.11.031